Activation and Coupling of Carbon Dioxide and Methane by Cationic Tantalum Clusters in the Gas Phase

Nikita LEVIN

Vollständiger Abdruck der von der Fakultät für Chemie der Technischen Universität München zur Erlangung des akademischen Grades eines

Doktors der Naturwissenschaften

genehmigten Dissertation.

Abstract

Efficient and selective activation and valorisation of small organic molecules, in particular of methane and carbon dioxide, under mild conditions is a "Holy Grail" of modern chemistry. Metal nano- and subnanoclusters serve as promising model systems for active sites of catalysts in these processes. Previous to this work, tantalum was demonstrated to be a prospective catalyst, as this element is able to promote the gas-phase reactions of methane oxidation, C-C coupling of CH_4 and CO_2, and potential ammonia synthesis.

In this work, the reactivity of size-selected cationic tantalum-based clusters towards methane, carbon dioxide, or mixtures thereof was studied in the ring electrode ion trap in the gas phase. In addition, the structure of the $[4Ta,C,2H]^+$ ion was analysed by means of infrared multiphoton dissociation spectroscopy at a free-electron laser facility.

When reacted with carbon dioxide, bare cationic tantalum clusters Ta_{1-16}^+ can enable either decarbonylation of CO_2 or its adsorption not followed by dissociation of a neutral fragment. The rates of these processes and the number of consecutive decarbonylation steps that a cluster can perform are size-dependent, which is reflected in two regimes of the reactivities of these clusters. Tantalum oxides in turn demonstrate enhanced rates of methane activation in comparison to bare clusters. Thus, mass selected $Ta_8O_2^+$ brings about non-oxidative coupling of two methane molecules in a catalytic cycle.

Kinetic analysis supported by theoretical calculations revealed that the cationic tantalum atom Ta^+ and its tetramer Ta_4^+ enable C-C and C-O coupling reactions respectively, when exposed to a mixture of CO_2 and CH_4. More specifically, in parallel to decarbonylation of CO_2, both cations dehydrogenate methane; the product of methane dehydrogenation then undergoes coupling with carbon dioxide followed by dissociation of a neutral compound.

The scientific works discussed in this thesis exemplify the importance of gas-phase investigations of size-selected metal clusters as fine models for the "real-world" catalytic systems. Coupled with theoretical explorations of studied systems, they provide insights into mechanisms of catalytic reactions, which is a crucial step towards the conscious design of catalysts in the future.

Zusammenfassung

Die effiziente und selektive Aktivierung und Aufwertung kleiner organischer Moleküle, vor allem von Methan und Kohlendioxid, unter milden Bedingungen ist ein "heilige Gral" der modernen Chemie. Metallnano- und -subnanopartikel dienen als aussichtsreiche Modellsysteme für aktive Zentren von Kalysatoren in diesen Prozessen. Vorangehend zu dieser Arbeit wurde gezeigt, dass Tantal ein vielversprechender Katalysator ist, da dieses Element in der Lage ist, in Gasphasenreaktionen die Oxidation von Methan, die C-C Kupplung von CH_4 und CO_2 und die mögliche Synthese von Ammoniak zu bewerkstelligen.

In dieser Arbeit wurde die Reaktivität massenselektierter kationischer Cluster auf Tantalbasis gegenüber Methan, Kohlendioxid und Mischungen davon in einer Ringelektrodenionenfalle in der Gasphase untersucht. Zudem wurde die Struktur des $[4Ta,C,2H]^+$ Ions mittels Multiphotonendissoziationsspektroskopie an einer Freie-Elektronenlasereinrichtung analysiert.

Nackte Tantalcluster, Ta_{1-16}^+, können, wenn sie mit Kohlendioxid reagieren, entweder die Decarbonlyierung von CO_2 oder dessen Adsorption ohne nachfolgender Fragmentieren ermöglichen . Die Rate dieser Prozesse und die Anzahl an konsekutiven Decarbonylierschritten, die ein Cluster durchführen kann, ist größenabhängig, was in zwei Reaktivitätsregimen dieser Cluster widerspiegelt. Tantaloxide wiederum weisen im Vergleich zu reinen Clustern erhöhte Methanaktivierungsraten auf. So bewirkt massenselektiertes $Ta_8O_2^+$ die nichtoxidative Kopplung zweier Methanmoleküle in einem katalytischen Zyklus.

Die durch theoretische Berechnungen gestützte kinetische Analyse zeigte, dass das kationische Tantalatom Ta^+ und sein Tetramer Ta_4^+ C-C- bzw. C-O-Kopplungsreaktionen ermöglichen, wenn sie einer Mischung aus CO_2 und CH_4 ausgesetzt werden. Genauer gesagt, dehydrieren beide Kationen Methan parallel zur Decarbonylierung von CO_2. Das Produkt der Methandehydrierung geht dann eine Kopplung mit Kohlendioxid ein, gefolgt von der Dissoziation einer neutralen Verbindung.

Die in dieser Arbeit dargelegten wissenschaftlichen Arbeiten verdeutlichen die Bedeutung von Gasphasenuntersuchungen größenselektierter Metallcluster als gute Modelle für "reale" katalytische Systeme. Gepaart mit theoretischen Untersuchungen der untersuchten Systeme liefern sie Einblicke in die Mechanismen katalytischer Reaktionen, was einen entscheidenden Schritt in Richtung eines bewussten Designs von Katalysatoren in der Zukunft darstellt.

Contents

List of Abbreviations

BR	branching ratio
CID	collision-induced dissociation
DC	direct current
DFT	density functional theory
FEL	free-electron laser
FELICE	The Free Electron Laser for Intra-Cavity Experiments
FT-ICR	Fourier-transform ion cyclotron resonance
GIB	guided ion beam
HAT	hydrogen atom transfer
HOMO-LUMO	highest occupied and lowest unoccupied molecular orbitals
IR	infrared
IRMPD	infrared multiphoton dissociation
KIE	kinetic isotope effect
MS	mass spectrometry
NOCM	non-oxidative coupling of methane
OAT	oxygen atom transfer
OCM	oxidative coupling of methane
POM	partial oxidation of methane
QMF	quadrupole mass filter
REIT	ring electrode ion trap
RF	radio frequency
SIFT	single-ions flow tube
ToF	time-of-flight (mass spectrometry)

1   Introduction

Conversion of energy and matter is the basis of the majority of chemical processes that occur in nature. To make rates of such processes reasonably fast, usually a special compound, which is called a catalyst, is required. By definition, a catalyst is a substance that enhances a rate of a reaction without being consumed over its course[1]. Typically, quite complex molecules with outstanding selectivity and turnover numbers, such as proteins or protein complexes, play a role of catalysts in biological systems. Thus, methane-to-methanol catalysis is mediated with 100% selectivity by methane monooxygenases[2], and nitrogenases help reduce nitrogen to ammonia in some bacteria[3, 4]. Researchers have put a lot of effort in the last two centuries into taking control over these and similar reactions and reproduce them firmly on the practical scale. These endeavours are driven by the demand to find a robust, efficient, and relatively cheap way to convert rather simple substances, such as nitrogen, methane, carbon dioxide, or water, into more useful compounds, which in turn serve as precursors to produce fuels, fertilizers, plastics *etc*. However, the extremely high structural complexity of above-mentioned natural catalysts and their sensitivity to reaction conditions make impossible their direct application in industrial processes. Therefore, the main directions of research in this field today are either investigation of bacterial systems to find a way to employ them as biorefineries of biomass[5], or search for reasonably simple analogues of natural catalysts. The latter approach allows for controlled fabrication of catalysts, selective for reactions of interest. In this regard, small metal clusters are promising candidates to serve as active sites of as-developed catalytic frameworks[6]. Chemistry of metal-clusters has gained greater attention since the discovery by Haruta *et al.* of remarkable size-dependent catalytic activity of subnanometer particles of gold, known for its "nobleness" in terms of chemical reactivity[7, 8]. However, despite a substantial progress in this field in the recent decades, there still exists no recipe for the conscious design of metal-cluster-based catalysts, and most of conventional catalysts currently used in industrial plants were implemented as the results of trial-and-error approach. It is therefore crucial to expand our knowledge on essential physical properties of small metal particles and how to match them to their chemical activity. The goal of this introductory chapter is to give a reader an idea about the nature of metal clusters, briefly overview the chemistry of methane and carbon dioxide and the challenges of their activation. Moreover, examples of modern hetero- and homogeneous catalytic systems dealing with this problem are given as well.

1.1   Studies on Metal Clusters

A metal cluster is a compound consisting of few metal atoms, bound together by chemical bonds. The number of atoms in a cluster may vary from two to few dozens and even hundreds. The particular interest for such nano- and subnanometer metal particles is premised on their exceptional physical and chemical properties, compared to bulk matter. Unlike bulk, clusters represent the non-scalable regime of matter, which means that addition of one single atom to a cluster may drastically change its physical properties, such as electron affinity, ionisation energy, HOMO-LUMO gap, spin multiplicity, magnetic moment and many more. This in turn greatly affects the cluster's reactivity in certain reactions. First attempts to investigate the behaviour of clusters in aerosols and colloids happened already in the 19th century, but it was only in the mid 1980s when technological advances allowed for the systematic study of properties and reactivities of metal clusters in the gas phase and in heterogeneous systems (*i.e.* in the systems where catalysts exist not in the same phase as reactants[1]). Significant advances in the recent decades in spectroscopic techniques and computational chemistry enabled precise measurements of various quantum properties of metal clusters, and attempts were made to match these parameters to reaction mechanisms. However, despite this noticeable progress, there exists no adequate answer to the question raised by Richard Feynman during his famous talk given at the annual meeting of the APSociety at the California Institute of Technology in 1959[9]:

> "What would the properties of materials be if we could really arrange the atoms the way we want them? They would be very interesting to investigate theoretically. I can't see exactly what would happen, but I can hardly doubt that when we have some control of the arrangement of things on a small scale we will get an enormously greater range of possible properties that substances can have, and of different things that we can do."

Even though today one can hardly call into question the veracity of the second part of this short excerpt, our understanding of metal-cluster reactivity and underlying mechanisms is far from being ideal.

1.2 Chemical Conversion of Methane and Carbon Dioxide

Values of heats of formation for the ideal gas state at 298.15 K are taken from Ref. [10].

1.2.1 Methane

Methane is a stable (heat of formation -74.9 kJ/mol) odourless colourless gas under standard conditions, with chemical formula CH_4. It is the simplest alkane, which makes it an attractive building block for generation of multiple carbon-based chemical precursors and fuels[11], especially when contrasted with prospective depletion of conventional sources of carbon such as oil. In addition, extraction of methane can be economically relevant due to its abundance and accessibility on earth. Methane is profusely generated in livestock agriculture networks and during anaerobic decomposition of biomass in natural wetlands and paddy rice fields[12, 13]. Importantly, it comprises up to ~90% of natural gas[14], which usually comes as a byproduct of oil extraction, and its substantial amounts are hidden in the form of methane clathrates under the seabed and in the permafrost zone[15]. Up to date, methane finds its use in chemical industry almost exclusively as the feedstock for the indirect conversion *via* synthesis gas (mixture of CO and H_2). This process, known as steam reforming, accounts for ~96% of total methane consumption for the production of chemicals[14]. Synthesis gas in turn is the main reagent to produce methanol, higher hydrocarbons *via* the Fischer-Tropsch process, and NH_3 *via* the Haber–Bosch process. However, the industrial processes of methanol and hydrocarbons production lack selectivity, the Haber-Bosch one is energetically very demanding, and both require harsh and ill-defined reaction conditions. Therefore, an efficient and selective way for direct conversion or liquefaction of methane is extensively sought for. Several such reactions, which were found to be of great importance, are listed below:

- Oxidative coupling of methane (OCM)

  In this reaction, two or more molecules of methane form hydrocarbon species in the presence of an oxidising agent. Particularly relevant are the reaction of ethane and ethylene formation (Eq. 1.1 and 1.2):

$$2\,CH_{4(g)} + \frac{1}{2}O_{2(g)} \longrightarrow C_2H_{6(g)} + H_2O_{(l)}, \quad \Delta H^o = -220.7 \text{ kJ/mol} \qquad (1.1)$$

$$2\,CH_{4(g)} + O_{2(g)} \longrightarrow C_2H_{4(g)} + 2\,H_2O_{(l)}, \quad \Delta H^o = -396.6 \text{ kJ/mol} \qquad (1.2)$$
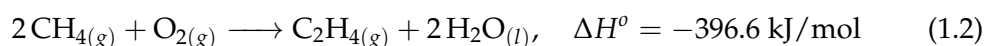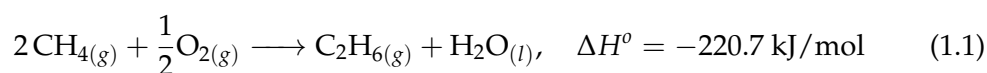
These reactions are extremely favourable from the perspective of thermochemistry, however, in real systems, the non-selective formation of CO and CO_2 becomes problematic, which makes this type of methane conversion so far economically unappealing. To circumvent the problem of overoxidation, mild oxidising agents were proposed, as for example, sulfur[16, 17] and carbon dioxide[18].

- Partial oxidation of methane (POM)

Another route of methane conversion is to use oxidants to generate oxygenates directly from methane[19]. Among others, methanol and formaldehyde are especially desired products due to their high relevance for industrial and technical applications.

$$CH_{4(g)} + \frac{1}{2}O_{2(g)} \longrightarrow CH_3OH_{(l)}, \quad \Delta H^o = -163.8 \, \text{kJ/mol} \tag{1.3}$$

$$CH_{4(g)} + \frac{1}{2}O_{2(g)} \longrightarrow CH_2O_{(g)} + H_{2(g)}, \quad \Delta H^o = -42.3 \, \text{kJ/mol} \tag{1.4}$$
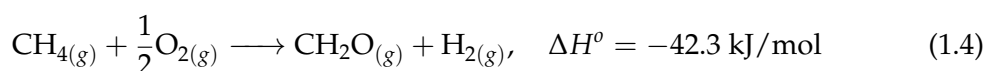
Products of the reactions shown in Eq. 1.3 and 1.4 are thermodynamically more stable than reactants, but usage of conventional catalysts still require high pressures and/or temperatures[20, 21], and, similar to the case of OCM, the reactions can further proceed to the unwanted overoxidation to CO and CO_2, which is a great impediment on the way to the practical application of POM and OCM reactions.

- Non-oxidative coupling of methane (NOCM)

Unlike OCM, reactions of non-ocidative coupling of methane do not involve any oxidant to form products. Such approach helps circumvent the problem of overoxidation, however it renders the reactions considerably endothermic.

$$2\,CH_{4(g)} \longrightarrow C_2H_{6(g)} + H_{2(g)}, \quad \Delta H^o = 65.1 \, \text{kJ/mol} \tag{1.5}$$

$$2\,CH_{4(g)} \longrightarrow C_2H_{4(g)} + 2\,H_{2(g)}, \quad \Delta H^o = 202.1 \, \text{kJ/mol} \tag{1.6}$$
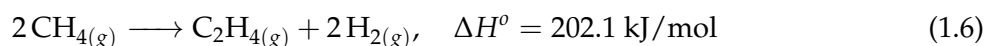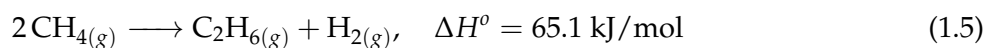
A remarkable feature of NOCM is the elimination of molecular hydrogen as a by-product of the hydrocarbon formation. This gas is believed to play a crucial role in the global energy system in the future[22], and new efficient and environmentally-friendly technological processes to reduce hydrogen are intensively searched for. Therefore, reactions of NOCM can be found promising candidates to develop sustainable green economy of the future.

Despite numerous prospective ways to utilize methane, the efficiency and selectivity of modern catalysts is insufficient to incorporate the corresponding reactions into high-throughput industrial processes. This is hardly surprising, as activation of methane's C-H bond represents a great challenge. The reason of such complication lies in the closed-shell electronic structure of this molecule, with ten electrons filling all bonding molecular orbital and anti-bonding ones left unoccupied. On top of that, very low polarizability exhibited by methane and strong delocalization of bonding molecular orbitals provide an additional challenge for an activating agent. As mentioned above, controlled methane oxidation to specific products suffers not only kinetic, but also thermodynamic constraints, as this reaction may favourably proceed to fully oxidised carbon product (CO_2). With all that said, it is no wonder that direct conversion of methane into such valuable products like methanol, ethane or ethylene was called a "Holy Grail" of modern catalysis[23].

1.2.2 Carbon Dioxide

Carbon dioxide represents a very stable compound (heat of formation -393.5 kJ/mol under normal conditions) with chemical formula CO_2. This molecule plays an important role in the life cycles of animals and plants and in the carbon cycle on earth[24]. In addition, it is also a greenhouse gas, the concentration of which in the atmosphere has significantly increased since the beginning of the industrial era[25]. Starting from around 1950, the emission of carbon dioxide has become the dominant source of anthropogenic emissions to the atmosphere, and this share continues to grow[25]. Even though there are multiple routes for CO_2 to get to the atmosphere, including such natural processes like respiration of living organisms or eruption of volcanoes and geysers, the main source of CO_2 emissions is combustion of fossil fuels, namely coal, petroleum, and natural gas[25]. The two main strategies to restrain further increase of carbon dioxide emissions are CO_2 capture and storage and CO_2 capture and utilization to useful chemicals and fuels[26, 27]. The conversion of carbon dioxide into other compounds poses a challenging task: not only this molecule is very stable thermodynamically, it is also inert in terms of kinetics, as its electronic configuration features a closed-shell structure, very much like that of methane. To date, CO_2 is used in production of multiple diverse chemicals, and the major share of CO_2-consumption in industry falls on generation of urea and methanol[28, 29]. These processes involve multiple cycles of synthesis under harsh conditions[27], which makes them energetically demanding and poorly controllable. Production of methanol and urea is extremely important for chemical industry and agriculture, which makes direct hydrogenation of carbon dioxide to methanol (Eq. 1.7) and CO_2-NH_3 coupling (Eq. 1.8) hot topics in the modern catalysis[27].

$$CO_{2(g)} + 3\,H_{2(g)} \longrightarrow CH_3OH_{(l)} + H_2O_{(l)}, \quad \Delta H^o = -131.0 \text{ kJ/mol} \tag{1.7}$$

$$CO_{2(g)} + 2\,NH_{3(g)} \longrightarrow CO(NH_2)_{2(s)} + H_2O_{(l)}, \quad \Delta H^o = -133.6\ kJ/mol \qquad (1.8)$$
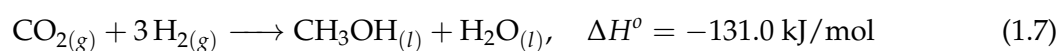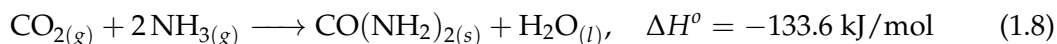
1.2.3   Coupling of Methane and Carbon Dioxide

Another type of reactions worth mentioning in regards to activation of methane and CO_2 are C-C coupling reactions, where carbon atoms from both these two molecules are involved in the bond formation, and C-O coupling reactions, where one of the oxygen atoms of CO_2 forms a bond with the carbon atom of methane. For example, acetic acid can be produced in the following reaction (Eq. 1.9):

$$CH_{4(g)} + CO_{2(g)} \longrightarrow CH_3COOH_{(l)}, \quad \Delta H^o = -16.1\ kJ/mol \qquad (1.9)$$

Syngas is generated in the catalytic process which is called dry reforming of methane (DRM, Eq. 1.10):

$$\frac{1}{2}CH_{4(g)} + \frac{1}{2}CO_{2(g)} \longrightarrow CO_g + H_{2(g)}, \quad \Delta H^o = 123.7\ kJ/mol \qquad (1.10)$$
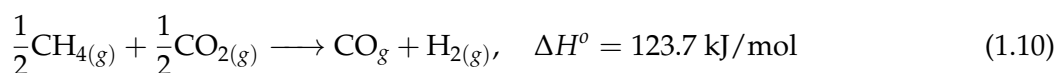
The latter reaction is of great economical importance, as it provides the feedstock for methanol production; however, catalytic DRM to syngas involves multiple adsorption, activation, bond-cleavage, coupling and desorption steps, which significantly narrows the choice of proper catalysts for this reaction.

1.3   Examples of Heterogeneous Catalytic Systems

In order to put the topic of gas-phase investigations of metal clusters and their reactivity into a broader context, a brief review of principles of heterogeneous catalysis is given in this section on the example of methane conversion, along with selected results of recent research efforts.

As the name already suggests, two or more phases are involved in a heterogeneous catalytic process. Normally, a catalyst is present in a reactor in form of a solid surface, whereas reactants and products usually exist either in gas- or liquid phase. Dispersed metal clusters, surface structural features, and surface point defects may act as active sites of a catalyst. A reaction therefore occurs in a thin layer between gaseous or liquid phase and a surface. Such assembly can be scaled for practical applications[30], and its different types make up catalytic zones in chemical reactors on most chemical plants. Plural heterogeneous catalytic frameworks were proposed to convert CH_4 and CO_2 into valuable products and fuels. An exhaustive overview of methane and carbon dioxide activation challenges and recent advances can be found in the Ref. [23, 31–34]. For illustrative purposes, few noteworthy examples of methane conversion over heterogeneous catalysts are considered in this section.

Among these, metal-exchanged zeolites (metal = Co, Ni, Co, Fe) enabled direct conversion of methane to methanol with selectivity to methanol more than 75%[35–

37]. Another example of zeolite-based methane activation is methane dehydroarom-atization on Mo-doped zeolites[38]. In these systems, the yield of products can reach its thermodynamic limit with the selectivity up to 98% under temperatures ranging between 150-800°C[35–38]. Despite their high tunability, zeolites still have not found application in industry, because the corresponding chemical processes feature multiple separate stages with varying operating temperatures to run the reaction.

A possible solution to overcome thermodynamic and kinetic limits is to pump energy into catalytic system to enhance its performance. Thus, photocatalysts are employed to selectively convert methane to valuable products, *e.g.* syngas[39], liquid oxygenates[40] or benzene[41]. In such systems an external source of light is used to surmount thermodynamic and kinetic barriers. These barriers are associated predominantly with band gap transitions in metal oxides at active sites of a catalyst, methane C-H bond activation, and desorption of reaction products from a surface. This helps avoid the use of high temperatures and an associated formation of carbon and coke, and allows to greatly surpass a thermodynamic limit of a reaction. For more details on photocatalytic systems, the reader if referred to the works of Song *et al.*[42] and Li *et al.*[43].

Electrochemical cells provide another source of external, non-thermal energy for a reaction. In a typical electrolytic cell, an electrical potential is used to run redox reactions on electrodes and generate active species for the oxidation of methane. In the overall process of methane to methanol oxidation, the following two reactions occur on an anode (Eq. 1.11) and cathode (Eq. 1.12):

$$CH_4 + H_2O \longrightarrow CH_3OH + 2\,(H^+ + e^-) \qquad (1.11)$$

$$\frac{1}{2}O_2 + 2\,(H^+ + e^-) \longrightarrow H_2O \qquad (1.12)$$
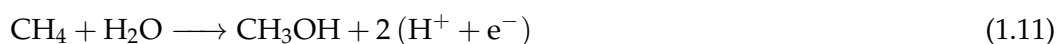
The selectivity to the methanol formation in such systems can reach 88% with conversion efficiencies up to 61%[44]. There are several limitations to be considered to avoid methane overoxidation and oxygen evolution. For example, a catalysts must provide enough $^*O$ radicals, but their coverage should be kept low to increase the selectivity towards methanol formation[45]. Moreover, it was suggested that an immediate removal of methanol from a reactor can inhibit its further oxidation[45]. This, however, complicates the design of a reactor and leads to additional operational costs. In addition, it should be noted that due to the exergonicity of the methane-to-methanol oxidation reaction, such electrochemical technology can in principle act as a fuel cell and additionally generate electrical energy.

1.4   Gas-phase Studies of Metal Clusters

1.4.1   Concept of Gas-Phase Studies

The analysis of heterogeneous catalytic systems in general provide invaluable information on how to improve "real-world" industrial processes by increasing selectivities of reactions and conversion of reactants. These improvements lead to reduction of wastes and energy consumption. This analysis focuses primarily on surface-reactant interactions, effects of surface geometries on reaction pathways, density and stability of active sites on a surface, and the impact of temperature and pressure on reaction rates and turnover frequencies. A vast amount of mass-spectrometric and spectroscopic techniques helps obtain these data, and in particular the information about the role of specific active sites in reactions. However, the capability of the surface techniques to investigate the intrinsic physical properties of active sites is very limited, and the very nature of their reactivity remains in most cases unclear. In contrast, the studies of particles, and among others, metal clusters in the gas phase aim at uncovering their quantum properties and matching them to the kinetics of these particles in gas-phase reactions[46, 47]. Such an approach allows to reveal underlying mechanisms of these reactions and generalize this knowledge for more conscious design of catalysts in the future. The characterization of gas-phase systems is usually relatively simple and executed by conventional mass-spectrometric and spectroscopic techniques[47]. This simplicity originates from the absence of solvation effects or cluster-surface interactions, that can significantly alter properties of an investigated particle or even hamper its analysis. In addition, isolated small metal clusters can be reasonably accurately modelled with *ab-initio* and dynamic quantum-chemical calculations employing the density functional theory (DFT). These calculations provide information on the cluster's geometry, electronic structure, spin states, ionization potentials *etc.*, which gives deeper insights into fundamentals of processes that occur in chemical reactions between a metal cluster and reactants in the gas phase. These advantages allow free metal clusters to become experimentally tractable models for surfaces and heterogeneous catalysts[48]. However, the mass-spectrometric methods, used to explore kinetics and energetics of clusters, are applicable exclusively to charged species. Along with other limitations of gas-phase studies, namely, the absence of cluster-surface and/or cluster-solvents interactions and the necessity of vacuum conditions in experimental chambers, this precludes extrapolation of properties of investigated charged metal clusters directly to "real-world" industrial catalytic systems. Despite this constrains, the gas-phase experiments provide a conceptual framework and a useful tool to explore electronic and geometrical structures of nanoparticles and match them to the mechanistic patterns of corresponding reactions[49].

In the following subsections, a brief overview of common experimental techniques for gas-phase cluster reactivity and selected results of gas-phase activation of methane and CO_2 is given. The goal of this overview is not to compare or assess

different techniques or approaches, but rather to introduce the reader to the field of gas-phase studies of cluster reactivity.

1.4.2 Cluster Sources and Reactor Types

Systematic investigations of gas-phase metal-cluster systems began in mid 1970s with the appearance of ion sources capable to generate molecular jets of charged metal clusters[50]. Early prototypes were represented by **thermal heated oven** sources (also known as Knudsen ovens)[51, 52]. In such assemblies, a metal vapour is seeded into a gas stream which then undergoes supersonic expansion through a nozzle. This allows to receive highly intensive hot cluster beams with a narrow velocity distribution[51]. Such ion beams were used to measure cross sections for electronic excitation[51], determine shell structures of clusters[53, 54] and deposit size-selected metal clusters[55]. Almost a dozen years later, the **electrospray ionisation** (ESI) technique was developed by Yamashita and Fenn[56]. An electrospray is generated when a solvent is pushed through a thin capillary set under high voltage potential towards an orifice of an analyser. A nebulizer gas is used to shape an aerosol plume at the capillary tip, and the charge-residue and ion-evaporation processes drive the subdivision of as-formed droplets to produce multiply-charged ions[57]. ESI has become widely used in mass-spectrometric investigations of biological samples due to the mildness of this ionization method; however, it also found use in the studies of hydration energies of gaseous metal clusters[58–61] and ion evaporation processes[57]. At the same period of time, the **laser-vaporisation** (LaVa) technique emerged, which remains until now one of the most widely employed method to generate beams of thermalised charged metal clusters and nanoparticles. The original setup was designed Smalley and co-workers[62]. It is based on the ablation of a metal disk or a rod by a pulsed laser beam of high power. The as-produced metal plasma is thermalised by collisions with a buffer gas and condensed *via* supersonic expansion through a nozzle into vacuum. This setup enables cluster formation of metals with high boiling points and metal alloys, which greatly extended the research field of gas-phase cluster chemistry.

The development of cluster-generation methods was followed by the advancement of cluster-reactivity-measurement techniques. One of the first experimental approaches to study gas phase reactions were **flow tube** reactors[63]. In a typical flow-tube setup, clusters generated in an ion source are transported into a reactor tube filled with a mixture of buffer and reactant gases. The excess of the buffer gas guarantees a quick thermalisation of the clusters and a laminar flow in the tube. The reaction occurs in the gas phase, and products and intermediates are transported through ion optics to a mass analyser (*e.g.* a quadrupole mass spectrometer). The reaction temperature is controlled by heating/cooling jackets coating the tube, and variation of reactant-gas pressure enables the monitoring of reaction kinetics. When clusters of particular sizes are preselected before entering a flow-tube reactor, the setup is known specifically as single-ions flow tube (SIFT)[64]. A similar setup is

characteristic for **collision cells**. In such an apparatus, much lower pressures are employed, and charged particles undergo not more than one collision with a reactant gas, which allows to avoid some of the limitations of fast-flow tubes[65]. However, lack of thermalisation may lead to fragmentation of species with low heat capacities, which has a critical effect on the analytical capabilities of this experimental method. In contrast to flow tubes, the method of **guided ion beam** (GIB) mass spectrometry allows for the analysis of charged particles only. It employs a symmetric assembly of RF ion optics to confine ion movement in radial directions. Typically, quadrupoles or multipoles filled with a mixture of buffer and reactant gases are used as reactive chambers. Such setups are mainly applied to study thermodynamics and kinetics of reactions between reactant gases and either neutral or charged clusters by measuring cross-section of these processes. More specifically, information on reaction endothermicity, metal-metal and metal-adsorbate bond energies, reaction and dissociation pathways, and electronic structure (with assistance of quantum-chemical calculations) can be obtained[66]. In addition to the radial confinement, the motion of ions in a guided-ion-beam setup can also be restrained in the axial direction by applying DC voltages at the ends of the ion guides. This allows for the **trapping** of ions in space and opens perspectives for precise kinetic and spectroscopic studies[67–69]. Yet another trapping technique widely used in the modern gas-phase research laboratories is **Fourier transform ion cyclotron resonance** mass spectrometry (FT-ICR)[70]. The use of homogeneous magnetic filed of high intensity forces ions to move in circular orbits with specific Larmor frequencies thus trapping them radially, and DC potentials confine them axially. The high-/ultra-high vacuum needed for the operation of an FT-ICR apparatus limits the application of this technique to single-collision experiments. The exceptional trapping capability of the FT-ICR technique enables precise kinetic measurements[71]; however, reaction intermediates and products are not thermilized, and dissociation pathways cannot be neglected.

1.4.3   Gas-phase Activation of Methane by Cationic Metal Clusters

In this and the following section, a general overview of kinetic processes occurring during gas-phase activation of methane and carbon dioxide by cationic metal clusters is given. In order to gain more detailed insights, a reader may access the works mentioned in these two sections and references therein. Examples of scientific works dealing with types of reactions specific to the subject of the thesis are given in the corresponding results chapters.

By "activation of a molecule" researches usually understand any interaction causing a weakening of the molecule's bonds, and more specifically — bond bending, stretching and scission, which may lead to an enhancement of the molecule's reactivity. Several scenarios are available for a molecule when it encounters a metal cluster in the gas phase: elastic scattering not followed by any sort of further interaction, association reaction characterized by the formation of Van-der-Waals bonds

between two reacting particles, or chemisorption of the molecule on the cluster followed by electronic and structural rearrangements. The latter scenario has gained an increased interest from the researchers who study activation of methane, because the species formed in the corresponding processes may represent key intermediates for further methane valorisation. A process, featuring such a methane bond restructuring, is a hydrogen atom transfer (HAT) from a carbon atom to a cluster. The direct HAT with the release of a methyl radical occurs in the reaction of open-shell metal oxide with methane when a high spin density is concentrated at the oxygen atom[72–74]:

$$CH_4 + MO^{+\cdot} \longrightarrow CH_3^\cdot + MOH^+ \tag{1.13}$$

This reaction is of particular importance for the field of catalysis, because methyl radicals produced in the course of the hydrogen atom abstraction are considered to be key intermediates of oxidative dimerization of methane:

$$CH_3^\cdot + CH_3^\cdot \longrightarrow C_2H_6 \tag{1.14}$$

The presence of oxygen-centered radicals was discovered to enhance the oxidation reactivity of metal-based catalysts towards the cleavage of the C-H bond of methane[75]. When there are no oxyl radicals present, the reaction is inhibited due to large barriers associated with decoupling of the M=O bond and the development of a high spin density at the accepting oxygen atom[76].

In the case of an indirect HAT on cations of metal oxides, a transition complex $[CH_4 \cdots M–O^\cdot]^+$ as well as an intermediate $[CH_3–M–OH]^+$ are generated. This metal-mediated pathway is typical of small diatomic metal oxides with vacant sites enabling the coordination of methane to the metal core. In this reaction, a methane molecule is first coordinated to the metal center, and the C-H scission takes place at the reactive oxo-center[73, 77]. Due to specific spin states of both the metal oxide and the insertion intermediates $M(CH_3)(OH)^+$, the potential energy surface of a thermal reaction usually involves a spin–orbit mediated crossover from the high-spin to the low-spin surface and back to the high-spin one in order to ensure the reaction to proceed through the channel of the lowest energy[78]. At the end of the HAT process, the methyl radical can either be released, or coupled with an -OH group to form a cluster-methanol species. These two reactions were observed, for example, in the gas-phase reactions between methane and FeO^+[79] and MnO^+[80].

The coordination of a methane molecule on a cluster may lead to the formation of a covalent metal-carbon bond. This process is usually accompanied by the scission of two C-H bonds of methane and the elimination of a hydrogen molecule. Under thermal conditions such reaction only occurs efficiently when the formed M=C bond is stronger than the C-H bond of methane. The reactivity of atomic cations of different metals with methane was thoroughly investigated in a SIFT experiment by Shayesteh *et al*[81]. Among studied species, only Ta^+, As^+, Nb^+, W^+, Os^+, Ir^+, and

Pt^+ dehydrogenate methane, with Ta^+, W^+, and Ir^+ being capable to perform several dehydrogenation steps. These results match with the values of metal-methylene bond strengths received in a GIB studies of the metal–ligand thermochemistry (see references in [81]). The driving force for the high reactivity of 5d transition-metal cations are lanthanide contraction and relativistic effects, which lead to changes in orbital sizes resulting in an increased overlap and the stabilization of the $M=CH_2$ bond[82, 83]. The $[M,C,2H]^1$ complex can act as intermediate species for the formation of valuable products. For example, catalytic oxidation of methane by molecular oxygen was performed by Pt^+[84], Ta^+ brought about the coupling of methane and carbon dioxide to $OCCH_2$[85], and reactions of $Ta_{1,4}CH_2^+$ with oxygen in the gas phase lead to the release of diverse neutral products[86]. In addition, Au_2^+ was found to catalyse methane conversion into formaldehyde and ethylene[87, 88]; however, the catalytic formation of ethylene on Au_2^+ was later put into question[89].

Further reaction pathways of an $[M,C,2H]^+$ complex are governed among other aspects by its structure. This species can in principle exist in three different isomeric forms: metal-carbene $M-CH_2$, metal-hydridocarbyne $H-M-CH$, and metal-dihydridocarbide H_2-M-C. The conventional kinetic studies that use solely mass-spectrometry are not able to provide information on precise structures of analysed species; therefore, an additional analytical tool is needed to tackle this problem. Infrared multiphoton dissociation (IRMPD) spectroscopy, in particular employing free electron laser (FEL), has proved its usefulness for the structural analysis of diverse molecules, including gas-phase metal-organic complexes[90]. More specifically, a vast amount of studies was recently dedicated to the investigation of intermediates of methane association to metal clusters[91]. In an IRMPD experiment, resonant absorption of electromagnetic waves in the IR range by a molecule results in the excitation of its vibrational modes and eventually in its fragmentation, and structural information is gained by the comparison between experimental fragmentation profiles and those calculated by means of DFT.

1.4.4   Gas-phase Activation of Carbon Dioxide by Cationic Metal Clusters

Carbon dioxide can associate with neutral particles in both monodentate (η^1-C and η^1-O) and bidentate (η^2-C,O and η^2-O,O) modes[92–94]; however, the linear η^1-O coordination is usually the most favorable for the reaction with cations due to the electrostatic nature of bonding[95]. This "end-on" coordination enables a transfer of an oxygen atom from a CO_2 molecule to a metal center M^+ when a M^+-O affinity is higher than that of CO-O[96, 97]. Analogously to a HAT in reactions of metal clusters with methane, this process is called OAT (oxygen-atom transfer):

$$M^+ + CO_2 \longrightarrow MO^+ + CO \qquad (1.15)$$

[1]this notation reflects the stoichiometry of a compound when its structure is unknown

The process of the OAT is believed to proceed *via* the dissociative chemisorption of a CO_2 molecule and the formation of an insertion complex [O-M$^+$-CO][98–101]. This is followed by the release of a CO moiety with the formation of a cluster oxide, which is preferred over the elimination of an O-atom with the formation of a cluster-CO complex. The latter process has an endothermic threshold of around 4-5 eV in the gas-phase reactions between CO_2 and V$^+$[102], Fe$_{1,2}^+$[101], or NbO$_{0,1}^+$[103].

The kinetic constraints of the CO_2 activation are limited to electronic, spin, and geometric considerations. Thus, activation of a CO_2-molecule by cations of transition metals is promoted by donation of electrons from d-orbitals into a π*-antibonding molecular orbital of CO_2, thereby bending and loosening the C=O bond. Therefore, the probability of an OAT from a CO_2 molecule to a metal cation depends on the availability of valence electrons on the metal center. At the same time, spin conversion necessary for the diabatic dissociation of a molecule of carbon dioxide represent a kinetic barrier of 1.97 eV[101], which greatly reduces the efficiency of the CO_2-decarbonylation process for larger clusters.

Another challenging yet important task is to determine the exact structures of studied clusters and reaction intermediates. Structural investigations allow, for example, to differentiate between molecular adsorption and dissociative chemisorption of carbon dioxide. One approach is to measure energies of collision-induced dissociation (CID) of a studied species, a methodology systematically employed *e.g.* in the group of Armentrout[101–104]. CID experiments yield only bond energies and provide no structural information. A more useful technique in this regard is IRMPD coupled with DFT calculations. The comparison of DFT predictions with experimental vibrational bands provides information on structural configuration and binding modes of investigated species. Some examples of such works can be found in the Ref. [94].

1.4.5 Gas-Phase Coupling of Methane and Carbon Dioxide

Among atomic cations of all transition elements, only Nb$^+$, Ta$^+$, and W$^+$ are capable to perform both methane dehydrogenation and CO_2 decarbonylation reactions in the gas phase[81, 96]. Among these three, only the reactivity of Ta$^+$ towards a consecutive activation of methane and CO_2 in the gas phase was investigated[85] to this date. The product of the first methane-dehydrogenation reaction TaCH$_2^+$ was isolated and exposed to carbon dioxide, and the kinetic analysis unambiguously indicated a C-C coupling reaction and the release of a neutral species[85]. The overall reaction is given with the following equation:

$$TaCH_2^+ + 2\,CO_2 \longrightarrow TaO_2^+ + CO + C_2H_2O \tag{1.16}$$
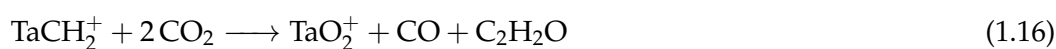
Later, this work was complemented by a comprehensive theoretical study of this reaction[105].

The gas-phase coupling reactions between these two molecules have not receive any further attention until recently, when the group of He published two more studies concerning this topic[106, 107]: in one of those, a bimetallic CuB^+ cation forms $CuBCH_3^+$ in the reaction with methane, and then this intermediate reacts with CO_2 to bring about (non-selectively) the C-C coupling followed by the release of C_2H_2O[106]; in the other one, a $RhVO_3^-$ anionic oxide activated one molecule of CH_4 and one of CO_2 to form a $RhVO_3(CH_4)(CO_2)^-$-complex, which under elevated temperature dissociates *via* four parallel reaction channels with the release of different neutral products[107].

As mentioned in the previous sections, the efficient utilisation of methane and carbon dioxide is of increased relevance from both economical and environmental perspectives. Their simultaneous conversion is therefore particularly profitable; however, the coactivation of both CH_4 and CO_2 is associated with multiple thermodynamic and kinetic limitations, what renders the search of a proper catalyst a challenging task.

1.5 Thesis Outline

This thesis comprises the results of the research efforts focused on the kinetic investigation of the reactivity of small cationic tantalum clusters towards the activation of methane and carbon dioxide in the gas phase under thermal conditions, complemented by a spectroscopic structural analysis of the $[4Ta,C,2H]^+$ species. The specific interest to the chemistry of bare and ligated tantalum clusters is motivated by recent discoveries of their increased reactivity towards methane activation[108–112]. Yet, the literature on gas-phase interactions of tantalum clusters with carbon dioxide is scarce, even though Ta^+ was found to be one of the few elements, whose atomic cations can bring about decarbonylation of a CO_2 molecule to form MO^+[96, 97]. Up to date, the reactivity of Ta clusters of different sizes with CO_2 has not been investigated, and the work presented in this thesis purports to remove this white space. In addition, the previously demonstrated ability of Ta^+ to couple two molecules of methane and carbon dioxide with the release of a neutral species[85] incentivised further investigation of this reaction in this work, but mediated by multiatomic Ta cluster cations.

The thesis is divided into several chapters and adheres to the following structure: first, Chapter 2 describes the experimental techniques employed during the course of the studies. Chapter 3 presents the results of the kinetic experiments on the activation of CH_4 by $Ta_8O_2^+$. This system was found to mediate catalytic conversion of two methane molecules into ethane and molecular hydrogen. The findings were supplemented by the experiments with CD_4 (fully deuterated methane). In Chapter 4, the structures of $[4Ta,C,2H]^+$ and its isotopologues are revealed by means of FEL-IRMPD spectroscopic technique and DFT-based calculations. This species features

the dihydrido-carbide structure, which was not reported previously for the products of methane dehydrogenation mediated by metal clusters, and which might be responsible for the reactivity of this compound with molecular oxygen[86]. Furthermore, the reactivity of Ta_n^+ clusters of different sizes (n=1-16) towards CO_2 is investigated in the kinetic gas-phase experiment and complemented by some DFT findings (Chapter 5). Finally, C-C and C-H coupling promoted by $Ta_{1,4}^+$ is discussed in Chapter 6. When either of these ions is exposed to a mixture of CH_4 and CO_2 in the gas phase, the release of a neutral species is observed; however, compositions of these neutrals and mechanical pathways of their abstraction are different for both Ta-compounds.

2 Experimental

Two substantially different experimental techniques were employed in the works that will be discussed in this thesis. All the gas-phase kinetic experiments were carried out in the laboratory of "Gasphase Cluster Kinetics" at the Chair of Physical Chemistry at the Technical University of Munich, whereas the spectroscopic investigation of $[4Ta,C,2H]^+$ was performed in the molecular beam instrument coupled to the intracavity free-electron laser (FELICE) at the facility located at the Radboud University, Nijmegen. The detailed description of both techniques is given in the subsequent sections.

2.1 Apparatus for Gas-Phase Kinetic Studies

The experimental setup for gas-phase kinetic studies consists of four primary parts: a laser-evaporation cluster source, a quadrupole mass filter (QMF), a ring-electrode ion trap (REIT), and a time-of-flight (ToF) mass analyser. Schematically, the setup is shown in Fig 2.1. The goal of the apparatus is to measure the evolution of intensities of charged particles produced in the cluster source and products of their interaction with reactant gases, based on the time that they spend in the ion trap filled with a mixture of a buffer gas and reactant gases. The design of the experiment can be briefly described in the following way:

A laser pulse ablates a tantalum metal disk and generates hot plasma of tantalum ions. The latter are subsequently cooled by a helium buffer gas, pulsed in the cluster source *via* a piezo valve. The mixture of buffer gas molecules and metal species undergoes supersonic expansion through a nozzle into vacuum to facilitate the agglomeration of ions and neutrals into clusters. Upon expansion, clusters may pick up molecules of adsorbates pulsed into a reaction volume by a general valve to form ligated clusters. The cluster beam is focused by several stacks of Einzel lenses into a quadrupole ion bender, which deflects ions of a particular charge into a quadrupole mass filter (QMF). The QMF acts as an ion guide in the broadband mode and transmits ions within a narrow band of mass-to-charge ratios (m/z) in the mass-selection mode. The filtered ions fly into the ring-electrode ion trap filled with a mixture of buffer and reactant gases, where they are stored for a determined amount of time. Large excess of the buffer gas ensures multi-particle collision dynamics and quick thermalisation of all particles inside the trap. During the storage time, the ions collide with molecules of buffer and reactant gases. After the storage time ends, the

ions are pushed out of the trap by electrostatic potentials applied to the ring elec-
trodes. This way the ions get into the acceleration region of a ToF analyser, from
where they are pulsed into the ToF tube to be mass-separated. The detection of the
particles is realized by a chevron-type microchannel plate detector. All the triggered
components of the setup are synchronised together, and the timings and lengths of
triggers are controlled by a home-written LabVIEW program. The trigger pulses are
generated by Digital Delay Generators (model DG645).
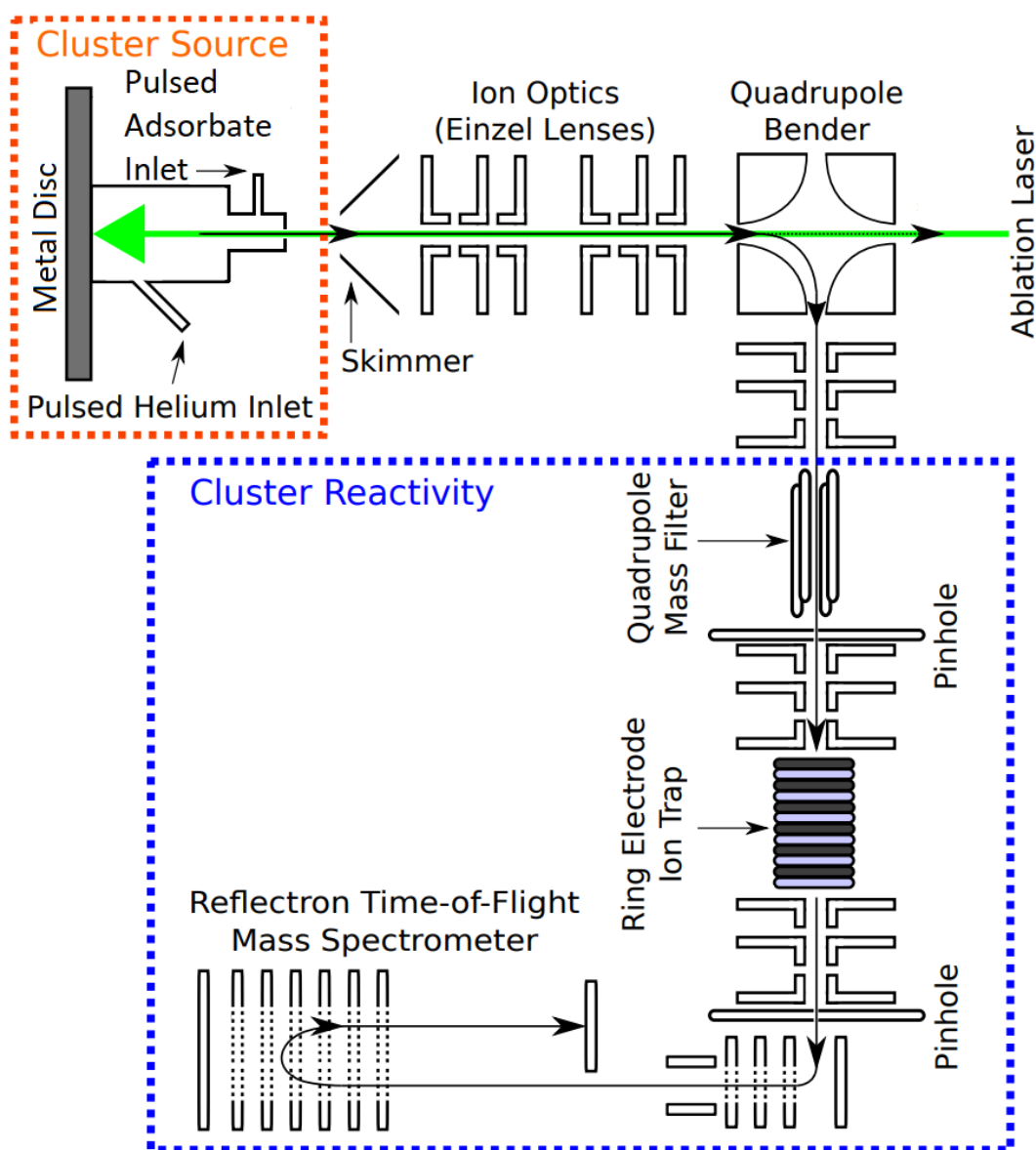
FIGURE 2.1: A schematic representation of the experimental setup. Adopted from [113].

2.1.1   Cluster source

Charged clusters are generated in a modified Smalley-type laser-vaporisation cluster
source[114]. A second-harmonic pulse of a Nb:YAG laser (532 nm, 60 mJ/pulse, 10
ns pulse width, 100 Hz repetition rate) irradiates a rotating tantalum disk. A motor

puts the disk in motion in a hypocycloid gear, which allows for the maximum exposure of the disk's surface to the ablating laser pulses. The irradiation by the focused laser beam evaporates metal atoms from a small spot in the near-surface layers, thus creating a gaseous mixture of hot ions and neutrals in the region inside the cluster source. The helium buffer gas (Westfalen AG, 5.0) is introduced into this region *via* a pulsed piezo valve, which operates under stagnation pressure of 7 bar with a typical pulse width of 400 µs. Collisions with helium atoms efficiently thermalise hot metal particles and quench their rotational and vibrational excited states. Driven by the pressure gradient, the buffer gas carries metal atoms through the nozzle into the chamber evacuated by rotary vane pumps (Ruvac WS 1001 backed by Busch R5 RA 0205), thus causing their supersonic expansion into the region of low vacuum. The cooling provided during expansion and collisions with the buffer gas molecules facilitates agglomeration of separate metal atoms and ions into clusters of various sizes and charge states. The size distribution of as-formed clusters is controlled by the piezo-pulse width, timing, and amplitude.

An inlet for adsorbate gas is built into the nozzle[115]. The injection of the gas is implemented by a general valve operating in the pulse mode (stagnation pressure 2 bar, ~100 µs pulse width). Such assembly enables picking up of adsorbate molecules by metal particles flying through the nozzle followed by the reactions between gas molecules and clusters. The products of these reactions are efficiently thermalised over their expansion into vacuum; however, too wide pulses of the general valve may cause leaking of the adsorbate gas into the region of the laser ablation and the subsequent formation of unwanted high-temperature products.

The evacuated chamber is separated from the rest of the apparatus by a skimmer, which ensures significantly lower pressure behind it and shapes the ion beam. The ions coming through the cluster source and passing the evacuated chamber and the skimmer are subsequently focused by several stacks of Einzel lenses into a quadrupole mass bender. The latter consists of four parallel rods with negative DC voltage applied to one pair of opposing rods and ground to the other pair. Therefore, negative ion and neutrals are filtered out, and only positive ions are steered into the QMF. The bender can be operated in both continuous and triggered modes, but during the experiment it functions in the triggered mode only, which allows ions to pass the QMF only during a limited amount of time (typically, for 3 ms) in each operation cycle. This prevents the continuous arrival of ions into the ion trap, what would lead to misinterpretation of kinetic data. A Pfeiffer TPU 2200 split system installed under the ion bender provides efficient pumping to separate the cluster-source compartment (high pressure region) from the rest of the apparatus which operates under high vacuum.

2.1.2 Quadrupole Mass Filter

A quadrupole mass spectrometer, sometimes referred to as quadrupole mass filter (QMF), is a type of mass analysers, able to conduct and separate ions in gas phase based on their mass-to-charge ratios[116]. It consists of four parallel rods; the opposing rods are interconnected electrically, and radio-frequency (RF) potentials (hundreds of Hz) are applied to each of them. Such assembly allows the transmission of all ions, whose masses[1] are higher than a threshold determined by the amplitude of RF voltages, in the space between the rods. Therefore, in the "RF-only" mode, the QMF acts as an ion guide, and a broad band of masses can pass through it. When a DC offset potential is applied between each pair of diagonal rods, only ions within a narrow band of m/z ratios are transmitted through the QMF, and all other ions have unstable trajectories and collide with the rods or the QMF housing. The width of this band depends on a combination of RF and DC potentials and is given by solutions of Mathieu's differential equation[117]. In the experimental setup described in this chapter, the commercially available quadrupole mass spectrometer Extrel Model 5221 is used. The ion transmittance achieved with this QMF can reach 15%, and ions with masses up to 16000 m.u.[2] can be mass-selected. The QMF is evacuated by Pfeiffer TMU 260 turbomolecular pump.

2.1.3 Ring-Electrode Ion Trap

The ions passed through the QMF are focused by two stacks of Einzel lenses into a home-built ring-electrode ion trap (REIT)[118]. In this trap, reactions between charged particles created in the cluster source and molecules of reactant gases take place. The structural arrangement of the trap is based on the design developed by Gerlich[119] and modified in the group of Asmis[68]. The schematic drawing of the REIT is shown in Fig 2.2a. It consists of twenty four coaxial molybdenum annular electrodes (1.4 mm thick, 32 mm OD, 11 mm ID) electronically insulated from each other by sapphire disks of the same shape.

Two larger electrodes close the trap at both ends. Such an arrangement is able to sustain a relatively wide range of gas pressures and facilitates the quick thermalisation of ions (see below). Square-wave RF potentials (typically, 350-700 kHz, 80-120 V) are applied to this assembly to enable the radial confinement of ions inside the trap. Therefore, the voltage at any electrode periodically switches with a radio frequency from a positive +V potential to a negative -V potential, and the voltages on electrodes in each adjacent pair have different signs (Fig 2.2b). The application of square-wave potentials is substantiated by the limitation associated with the use of conventional sinusoidal potentials — namely, by the operation of storing capacities for ions with different masses by varying exclusively the amplitudes of RF voltages,

---

[1]since the abundance of multiply charged ions is negligibly low, the *m/z*-ratio will from now on be referred to in this thesis simply as *m* or 'mass'

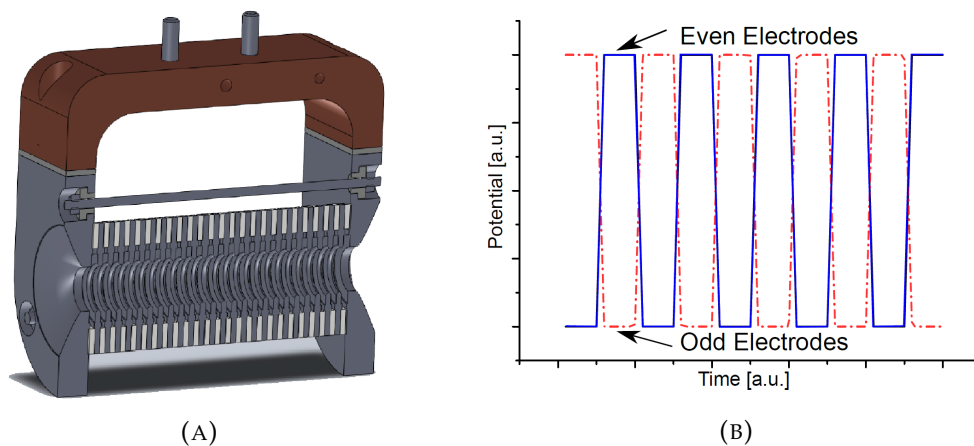[2]atomic mass unit ($\frac{1}{12}$ of the mass of an ^{12}C atom)

FIGURE 2.2: A) A schematic in-section drawing of the ring-electrode ion trap, B) square-wave RF potentials applied to the electrodes. Adopted with permission from [118].

which would inevitably lead to the necessity to apply voltages up to several kV to store ions with high masses.

During an experiment, the trap is continuously filled with a mixture of helium buffer gas (Westfalen AG, 6.0) and reactant gases. The chamber of the trap is pumped by a Pfeiffer HiPace 700M turbomolecular pump. The gas mixture is created in a separate mixing-chamber equipped by a capacitance gauge (Baratron 722B, MKS) to control pressures inside the chamber, which is evacuated by a Pfeiffer TMU 260 turbo-molecular pump backed by a Leybold TRIVAC D 65 B forepump. Typically, the reactant gas is diluted in several steps in the buffer gas until a required concentration[3] is reached. The mixture is streamed into the REIT by a gas-flow control unit (179C Mass Flow Meter, MKS) at the rate of 170 sccm. The pressure inside the trap is probed by a Baratron manometer (Baratron 722B, MKS). The differential gas injection and pumping cause an inhomogeneous distribution of the pressure inside the trap, thus limiting the control over absolute values of pressure to roughly 50% accuracy. In all the gas-phase kinetic experiments discussed in this thesis, the pressure at the manometer inside the trap was established to be 0.82 Pa, which enables a multi-collisional mode of ion-molecule reactions and the quick collisional thermalisation of ions within 1 ms[120].

The trap is mounted on a cold head of a cryo pump (PRK-800, Leybold) (see Fig 2.2a) attached to a closed-circuit helium compressor (RW2, Leybold), and the assembly of electrodes is embedded into a copper-box housing to avoid the heating *via* black-body radiation. The heating of the trap is operated by a temperature-control unit (Model 335 Cryogenic Temperature Controller, Lake Shore Cryotronics) through a resistive-heating cartridge attached to a copper block of the cold head. The same unit monitors the temperature of the entire REIT *via* a cryogenic temperature sensor (Cernox, Lake Shore Cryotronics) attached to one of the end ring electrodes.

---

[3]In this thesis, "concentration" is seen as the number of particles in a unit of volume $[X] = \frac{N_X}{V} = n_X$

The balancing of a heating and a cooling outputs allows setting up constant temperatures of the REIT in the range between 20 K and 320 K. The trap operates in three regimes. When only RF potentials are applied to the electrodes, ions pass through, and the REIT acts as an ion guide. Two other modes of operation must be discussed in more details. To store ions inside the trap, low DC voltages are applied to both end electrodes (Fig. 2.3a, red), thus confining the movement of ions in axial directions, in addition to the radial confinement provided by RF potentials. Fast ions flying from the outside surmount the low DC voltage at the entrance electrode (2-3 V) and undergo multiple collisions with the buffer gas, which along with the potential at the exit electrode (typically, 12-18 V) prevents their further movement in this direction. In such regime, ions can be stored within the trap for the time periods up to several seconds [118]. Due to collisions with gas molecules and Coulomb repulsion, the amount of stored ions declines exponentially in time. In the extraction regime, the storage DC voltages at the end electrodes are substituted by a potential gradient over all ring electrodes (Fig. 2.3a, black), superimposed over the RF potentials (Fig. 2.3b). This creates a driving force pushing ions out of the trap. Due to tight stacking of ring electrodes, ions leave the trap almost simultaneously, which makes REIT advantageous over other guided ion beam techniques. Specifically, such a setup allows for a coupling with a time-of-flight (ToF) analyser, that is normally characterized with higher resolution than quadrupole mass spectrometers. In addition, ToFs work in a pulse mode, which significantly increases ion transmission in comparison to the techniques that operate in a scanning mode and therefore lose ions during each scan.
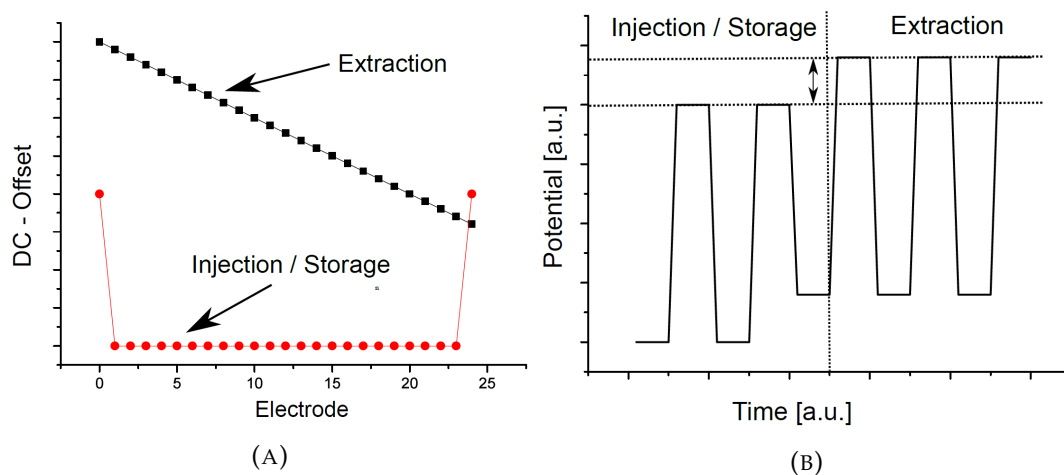
FIGURE 2.3: A) DC potentials applied to different electrodes during storage (red) and extraction (black) of ions, B) time evolution of the combination of RF and DC-offset potentials applied to a single electrode. Adopted with permission from [118].

2.1.4   Time-of-Flight Mass Analyser

Ejected from the REIT, ions are focused by two stacks of Einzel lenses into the acceleration region of the time-of-flight (ToF) mass analyser (Fig. 2.4). Here, the trajectory

of the ion cloud is deflected through 90° by a short (30 μs) HV pulse applied to the repeller electrode (U_1), and the ions are drawn into the field-free region of the ToF through an acceleration stage. The latter is constructed in the form of a stack of ring electrodes, where to the first, "extractor", electrode a short pulse of HV potential is applied (U_2), and the last one is grounded. The triggers of the deflection and acceleration of ions are synchronised with ejection of ions from the trap. Since ions with different masses are temporally separated during their transition to the ToF's acceleration region, the timing of the HV pulses on the repeller and the extractor are controlled by the LabVIEW master program in order to focus on a particular mass region. Therefore, only a relatively narrow band of masses (few hundred m.u.) is pulsed inside the ToF analyser, and all other masses are suppressed.
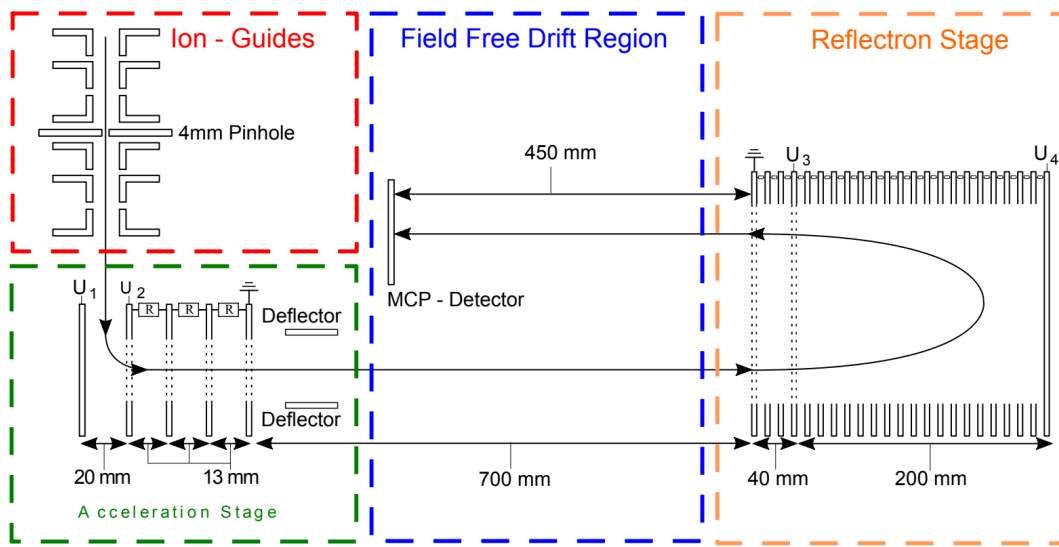
FIGURE 2.4: A schematic representation of the time-of-flight compartment. Adopted from [113].

In an idealized form, the principle of operation of a ToF mass analyser can be represented as follows: ions, leaving an acceleration region with velocity v, drift through a field-free region with the length l until they reach a detector. This velocity can be extracted from the equation

$$qU = \frac{1}{2}mv^2, \tag{2.1}$$

where q is the ion's charge, and U is the acceleration potential. Therefore, the time of flight t of a particle is given by

$$t = \frac{l}{v} = l\sqrt{\frac{m}{2qU}}, \tag{2.2}$$

which allows to obtain values of masses of ions based on the times of their arrival to a detector. In real measurements, however, results are heavily affected by the spreading of initial velocities and starting positions of ions, which greatly impairs

the resolving power of a mass spectrometer. To compensate for these two draw-backs, additional modifications were brought to the principle scheme of ToF and were implemented in the described apparatus. Namely, double-stage acceleration region (U_1 and U_2) allows to significantly extend the space focus[4] of ions[121], and a reflectron (U_3 and U_4) compensates initial distributions of velocities[122]. Such modifications limit the resolution-reduction effects to collisions with molecules of residual gases. To reduce the penetration of the buffer gas from the trap, a 4-mm pinhole is placed between the trap and the acceleration region of the ToF. The ToF is evacuated by two turbo-pumps (TPU-510 at the acceleration stage, Pfeiffer TMU 260 at the reflectron) that keep the pressure in the field-free region below 10^{-7} mbar. Through variation of U_{1-4}, the mass-resolution can be tuned, and its typical value amounts to 2000, which enables the discrimination between, for example, $Ta_8O_2CH_2^+$ and $Ta_8O_2CH_4^+$.

2.2   Analysis of kinetic data

In a typical kinetic experiment, ions produced by a single laser shot in the cluster source are collected in the REIT filled with a mixture of buffer and reactant gases and stored inside it for a specific amount of time. Charged reaction products are subsequently ejected to the mass analyser. The oscilloscope (LeCroy 9300 OM REVA) displays an averaged signal (usually 100-500 averaged spectra) coming from the detector for a single preset storage time, and values of intensities against times of flight are extracted and stored digitally as .txt files. When this cycle is repeated for different storage times, the evolution of the intensities of different ions can be traced and these data can be used to build kinetic models. The raw data are processed in home-written programs (python 3). First, the data are transformed from the time- into the mass domain, baseline corrected, and the absolute values of intensities of peaks are normalized to their integral. Thereafter, the output is transferred into a program which performs kinetic fitting of normalized intensities to the input kinetic models (see below). The results are model-specific, and the output yields reaction constants and kinetic traces.

2.2.1   Mechanisms of Gas-Phase Reactions

A generalized bimolecular association reaction between a charged metal cluster (or a ligated metal cluster) M and a molecule of reactant gas A can be represented as follows:
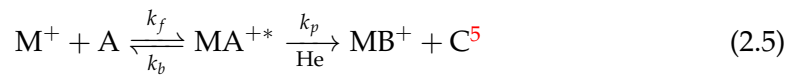
$$M^+ + A \underset{k_b}{\overset{k_f}{\rightleftharpoons}} MA^{+*} \tag{2.3}$$

In the equation above, MA^{+*} denotes an association product bearing the excess of heat released during the reaction course. In equilibrium, the association process is

---

[4]a point in space, where ions with the same mass arrive simultaneously regardless of their starting position

balanced by a dissociation of the formed product back to the reactants, and the overall reaction is characterized by the equilibrium constant $K = \frac{k_f}{k_b}$, where k_f and k_b are the rates constants of forward and backward reactions respectively. The dissociation is not the only reaction pathway accessible to the excited complex MA^{+*}. When a gas-phase reaction occurs in excess of a buffer gas, collisions with its molecules may lead either to the formation of stable MA^+ complex (Eq. 2.4) or to atomic rearrangements and product formation (Eq. 2.5). These two processes compete with each other, and the branching ratios are dependent on the kinetics of both pathways.

$$M^+ + A \underset{k_b}{\overset{k_f}{\rightleftharpoons}} MA^{+*} \xrightarrow[\text{He}]{k_s} MA^+ \tag{2.4}$$

$$M^+ + A \underset{k_b}{\overset{k_f}{\rightleftharpoons}} MA^{+*} \xrightarrow[\text{He}]{k_p} MB^+ + C^5 \tag{2.5}$$

When the partial pressure of the buffer gas is insufficient, collisional stabilization competes with the relaxation of the excited complex through fragmentation:

$$M^+ + A \underset{k_b}{\overset{k_f}{\rightleftharpoons}} MA^{+*} \xrightarrow{k_{fr}} F_1^+ + F_2 + ...^5, \tag{2.6}$$
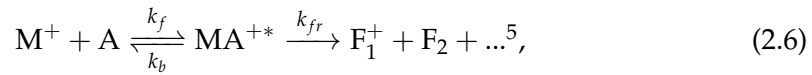
where F_i stands for molecular fragments. The latter case is characteristic of very exothermic reactions occurring under single-collision conditions, but such reactivity can also be observed in systems under multi-collisional conditions[123, 124].

Since the kinetic experiments considered in this thesis feature relatively high pressures in the REIT, and quick thermalisation within 1 ms is enabled for the reacting species, the reactions given in equations 2.4 and 2.5 are more relevant for further discussion and will be scrutinized here in more details. The rate responsible for the change in the concentration of $[MA^{+*}]$ in each reaction pathway can be expressed in the following form:

$$\frac{d[MA^{+*}]}{dt} = k_f[M^+][A] - k_b[MA^{+*}] - k[MA^{+*}][He], \tag{2.7}$$

where k denotes the rate constant of either intermediate stabilization k_s or product formation k_p. In a simplistic model, the concentration of $[MA^{+*}]$ is assumed constant; the steady-state approximation is therefore applicable, and $\frac{d[MA^{+*}]}{dt} = 0$, which results in

$$[MA^{+*}] = \frac{k_f[M^+][A]}{k_b + k[He]}, \tag{2.8}$$

and

$$\frac{d[MX^+]}{dt} = k[MA^{+*}][He] = \frac{kk_f[M^+][A][He]}{k_b + k[He]}, \tag{2.9}$$

---

[5] since the abundance of products is negligibly low in comparison to that of reactant and buffer gases, the back reactions can be omitted

where X is either A or B. The reactions of collisional stabilization of an intermediate or formation of products can therefore be described with a termolecular rate constant $k^{(3)}$:

$$k^{(3)} = \frac{kk_f}{k_b + k[\text{He}]} \tag{2.10}$$

In the kinetic low-pressure regime when $k_b \gg k[\text{He}]$, this can be further reduced to

$$k^{(3)} = \frac{kk_f}{k_b} \tag{2.11}$$

Since the concentrations of reactant and buffer gases are many orders of magnitude higher than those of ions stored in the trap and are continuously replenished, they can be considered to remain constant, and the overall reaction rate becomes pseudo-first-order.

$$\frac{d[\text{MX}^+]}{dt} = -\frac{d[\text{M}^+]}{dt} = k^{(1)}[\text{M}^+], \tag{2.12}$$

$$k^{(1)} = k^{(2)}[\text{A}] = k^{(3)}[\text{A}][\text{He}] \tag{2.13}$$

The analytical solution of the differential equation 2.12 is given by

$$[\text{M}^+](t) = [\text{M}^+]_0 e^{-k^{(1)}t}, \tag{2.14}$$

which describes the temporal evolution of the concentration of reactant ions as a function of initial concentration and pseudo-first-order reaction rate. Chemical systems with complex reaction pathways are described by sets of differential equations in multiple variables, which makes finding their analytical solutions a time-consuming or even impossible task.

2.2.2   Numeric Fitting of Experimental Data

A home-written python 3 program provides a platform to fit experimental data points with kinetic curves and extract corresponding pseudo-first-order reaction rates. A matrix containing normalized intensities of different ions against storage time is transferred to the program by a user, who also sets up reaction pathways between different species. The program translates the given model into a set of differential equations which is then solved by the algorithm based on the LSODA method[125]. Values of rate constants in the equations are automatically adjusted by the Levenberg-Marquardt algorithm[126, 127] to minimize least-square errors between experimental data points and fitted curves until a certain criterion of fit quality is met. The program outputs a list of pseudo-first-order reaction rates for each reaction of the input reaction model and draws kinetic curves which fit temporal distributions of experimental values of intensities for each ion. A user can propose several reaction models and choose the best one basing on the quality of fit reflected in the values of least-square errors and the simplicity of the models.

Apparent pseudo-first-order kinetic rate constants can be turned into second-order rate constants with the help of Eq. 2.13. The concentration of reactant gas is calculated under assumption of the validity of the ideal gas approximation:

$$p_{total} = n_{total} k_B T, \tag{2.15}$$

$$[A] = n_A = a \cdot n_{total}, \tag{2.16}$$

where p_{total} and n_{total} are total pressure and concentration of the gas inside the trap, n_A is the concentration of the gas A, a is the proportion of the gas A in gas mixture, k_B is the Boltzmann constant, and T is temperature of the reaction. Therefore,

$$[A] = n_A = \frac{a \cdot p_{total}}{k_B T}, \tag{2.17}$$

and

$$k^{(2)} = k^{(1)} \frac{k_B T}{a \cdot p_{total}} \tag{2.18}$$

2.3 IRMPD Spectroscopy

Infrared multiphoton dissociation spectroscopy (IRMPD) is an experimental technique used in most cases for structural analysis of ions and molecules in gas phase. The method is based on resonant absorption of multiple infrared photons by vibrational modes of a molecule, which leads to the dissociation of molecular bonds and the fragmentation of the molecule. Theoretical principles of IRMPD and the description of the technical equipment employed in the experiments are given in the sections below.

2.3.1 Vibrational Spectroscopy

In a general case of polyatomic nonlinear molecule, the number of vibrational modes is equal to 3N-6, where N stands for the number of atoms in this molecule, and the vibrational potential lies therefore in a (3N-6)-dimensional space. For the sake of simplicity, only the case of a diatomic molecule, featuring only oscillatory stretching along its axis, will be considered in this subsection in order to outline important concepts; however, a similar reasoning can be carried through for a more general case. In the zero-order approximation, the vibrational potential of a diatomic molecule has the form of a harmonic oscillator:

$$\hat{V} = \frac{1}{2} k \hat{x}^2 = \frac{1}{2} \mu \omega^2 \hat{x}^2, \tag{2.19}$$

where $\hat{V}$ is the potential energy operator, $\omega = \sqrt{\dfrac{k}{\mu}}$ is the angular frequency of the oscillator, k is the zero-order force constant of the oscillator, μ is the reduced mass of

the molecule, and $\hat{x}$ is the coordinate operator, which stands here for the momentary internuclear separation. The solution of the corresponding eigenvalue problem is

$$E_n = (n + \frac{1}{2})\hbar\omega, \tag{2.20}$$

where $\hbar$ is the reduced Planck constant and n = 0,1,2... is the index number of the equidistant energy levels (Fig. 2.5a). A more accurate model is described by the Morse potential:

$$\hat{V} = D_e(1 - e^{-a\hat{x}})^2, \quad a = \sqrt{\frac{\mu\omega^2}{2D_e}} \tag{2.21}$$

where D_e is the depth of the potential well. This representation accounts for anharmonicity of bond's oscillation, and the corresponding energy levels are then equal to

$$E_n = (n + \frac{1}{2})\hbar\omega - (n + \frac{1}{2})^2\hbar\omega\chi, \tag{2.22}$$

Here χ is an anharmonicity constant. Note, that the distance between adjacent energy level reduces with increasing number n, converging to a continuum at the dissociation limit (Fig. 2.5b). When the energy of the bond stretching reaches this limit, the bond breaks.
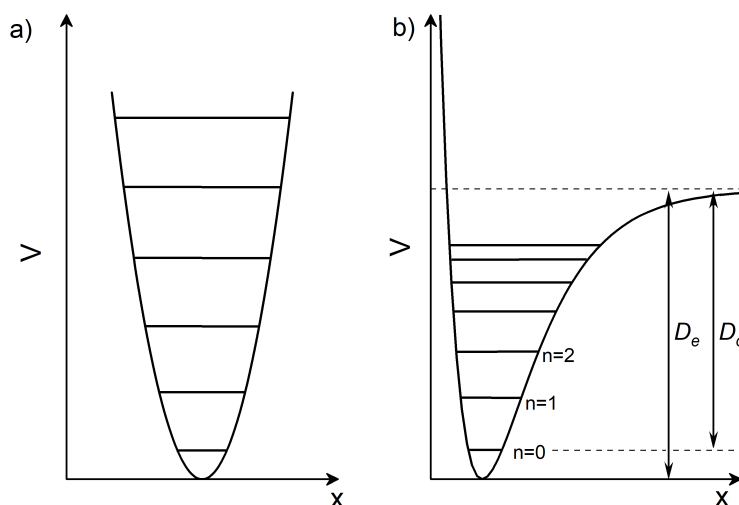
FIGURE 2.5: Quantum harmonic oscillator (a) and Morse potential (b) and corresponding stationary states. D_e is the depth of the potential well and D_0 is the dissociation energy, that is equal to the difference between a dissociation threshold and an energy of the zero vibrational level.

When a molecule interacts with a monochromatic electromagnetic wave, a resonant transition (n = k) —> (n = k+1), k≥0 may occur, if the energy gap between these states matches the energy of the wave. Further transitions (n = k+1) —> (n = k+2) are out of resonance due to anharmonicity of the potential and are therefore not possible. There are two relaxation channels available for an isolated excited

molecule: emission of a photon and intramolecular vibrational energy redistribution (IVR)[128]. The probability of elastic scattering is insignificant in the IR range, because of its dependence on the wavelength of the incident light. In contrast, the IVR describes an efficient process in which the energy pumped into the system is redistributed among other vibrational degrees of freedom. Its efficiency is proportional to the number of vibrational modes with which the excited state is coupled and therefore is usually higher for larger molecules. The adsorption of a quantum of energy followed by IVR leads to the increase of the density of states, what makes available further adsorption of electromagnetic radiation at the same resonant frequency. In such a manner, multiple adsorption events may happen, and the total inner energy of the system increases.

In the model of the harmonic oscillator (Eq. 2.19), transitions between non-adjacent energy levels (n = k) —> (n = k+2, k+3, k+...), k$\geq$0 are forbidden due to selection rules; however, for the anharmonic oscillator these restrictions are lifted and corresponding low-intensity transitions can be observed. In addition to that, in thermal systems, the distribution of molecules in the space of vibrational levels (k = 0, 1, 2,...) is describes by the Boltzmann distribution. Therefore, even relatively small molecules can be characterised by rather complex vibrational spectra.

When the amount of heat accumulated by a molecule through adsorption of multiple photons reaches its lowest dissociation limit, the molecule can undergo relaxation through several distinct processes. Emission of IR photons is typically of very low intensity and can be therefore neglected. Two other processes — namely, emission of an electron and fragmentation of the molecule, compete with each other, and their intensities depend on the molecular properties. Thus, electron loss is in particular characteristic of anionic particles M^-, for which the electron affinity of a neutral M is typically lower than a bond strength of the anion. Therefore, if internal energy of an anion M^- exceeds this electron affinity, M^- may emit an electron rather than undergo dissociation, what results in the decrease of the MS-signal corresponding to this anion[129]. For cations M^+, dissociation of a molecular bond prevails in the vast majority of cases, resulting in a depletion of the M^+-signal and a raise of a signal corresponding to charged fragments. This phenomenon underlies the principle of IRMPD and is utilized to probe structures of molecules where vibrational modes lie in the IR range. A big advantage of the IRMPD technique lies in its applicability to studies of low-pressure gas-phase systems, where conventional adsorption spectroscopy is no longer applicable due to insufficient densities of particles, and feasibility of construction of tunable high-fluence IR lasers (*i.e.,* free-electron lasers).

2.3.2 Free-Electron Laser

In the early days of IRMPD, the only light source capable to bring on multiple-photon molecular fragmentation in gas phase was the CO_2 laser[130]. More specifically, the emission of a CO_2 laser contains only rotational-vibrational lines in a narrow band between 9.2 and 10.8 μm. This substantially limited the applicability of

the technique to the identification of the loss of few characteristic moieties in organic molecules. The breakthrough in the field of the multiple-photon dissociation spectroscopy happened with the construction of free-electron lasers (FEL). In particular, to attain to the region of lower frequencies, the use of FELs has been proven highly beneficial for IRMPD[131]. The operation of a FEL is based on the coherent motion of free relativistic electrons in a spatially periodic magnetic field, which induces dipole radiation with an energy and a frequency depending on the parameters of an apparatus (Fig. 2.6). More specifically, a bunch of electrons produced in an electron gun pass through a magnetic field with a spatial periodicity along the axis of the electrons' propagation. The assembly of multiple magnets which generate this field is called undulator or wiggler. The undulator is positioned between two mirrors that form a resonator of the laser. Affected by the Lorenz force, the electrons move along a periodic curved trajectory inside the undulator, which induces dipole radiation with wavelength λ_s expressed in the following form:

$$\lambda_s = \frac{\lambda_u(1 + K^2)}{2\gamma^2} \tag{2.23}$$

Here, λ_u is the spatial period between the magnets, γ is the Lorentz factor accounting for relativistic energies of moving electrons, and K reflects the strength of the magnetic field. In more detail,

$$\gamma = \frac{c}{\sqrt{c^2 - v_z^2}} \tag{2.24}$$

and

$$K = \frac{eB\lambda_u}{2\pi m_e c}, \tag{2.25}$$

where c is the speed of light in vacuum, v_z is the velocity of electrons along the axis of the undulator, e is the charge of an electron, m_e is its mass, and B is the amplitude of the magnetic flux density varying sinusoidally along the undulator axis. The square of the Lorentz factor accounts, first, for the contraction of the undulator experienced by relativistic electrons, and second, the relativistic Doppler effect resulting from the transition between the electron frame of reference to the laboratory one. For the period of the undulator in the order of tens of mm, these relativistic effects bring about the output radiation in the IR range.

During the propagation of the electrons along the axis of the undulator, the transverse motion of an electron couples with the transverse component of the electric field of the radiation, which causes a phase-dependent modulation of the electron's transverse velocity. Since the electrons are equally distributed over the phases, this phenomenon induces a modulation of the electron density along the axis of propagation and the formation of micro-bunches of electrons, the number of which is equal to the number of periods of the undulator. Therefore, a macropulse of a FEL represents a few-µm-long series of ultrashort (few pm) equidistant pulses. A more
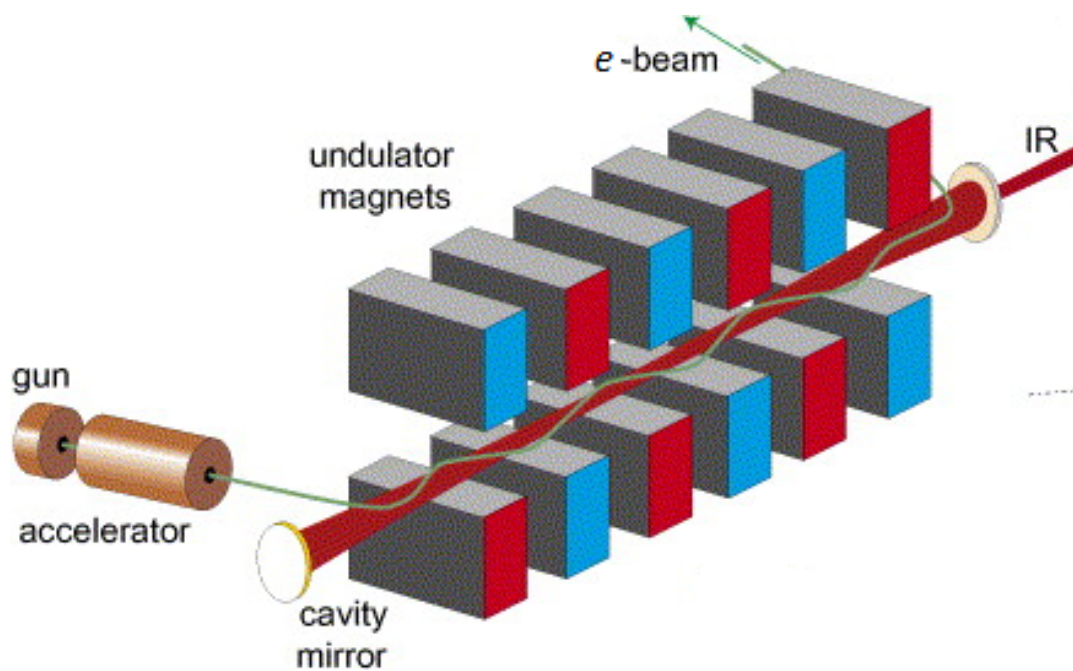
FIGURE 2.6: A schematic representation of the free-electron laser experimental setup. Adopted with permission from [132].

elaborate description and derivation of the FEL principles can be found in the ref. [133].

3 Catalytic Non-Oxidative Coupling of Methane

Activation of methane by atomic cations in gas phase was thoroughly investigated both in kinetic experiments[81, 82, 134, 135] and spectroscopically[91], and Ta^+ was found to be one of the few investigated atoms, able to activate CH_4. Due to these discoveries, Ta received increased attention from the researchers in this field, and several studies covered the reactivity of Ta^+, Ta_n^+ clusters, and oxides thereof with methane[108–112, 136]. In particular, is was discovered that the rates of methane dehydrogenation by Ta_4O^+ and Ta_5O^+ are much higher than those by Ta_4^+[111], whereas bare clusters comprising five or more Ta atoms cannot dehydrogenate methane at all[112]. This striking discoveries incited further exploration of reactions between $Ta_nO_m^+$ and methane. Among all investigated clusters of this kind, $Ta_8O_2^+$ demonstrated an unexpected kinetic behaviour, which can be explained in terms of a catalytic cycle. Previously, various metal, mainly noble-metal, clusters were reported to perform catalytic oxidation of CO to CO_2 in gas phase[137–146]. Examples of catalytic methane conversion are, in contrast, scarce and are represented only by Au_2^+- and Pd_2^+-based systems[87, 88, 147, 148].

This chapter describes in details the gas-phase reactivity of $Ta_8O_2^+$ towards activation of methane. It shows conclusively, that this ion can bring about the dehydrogenation of one methane molecule with the formation of a $[Ta_8O_2CH_2]^+$ intermediate, followed by the coupling with another molecule of methane and the consecutive elimination of C_2H_6 with the regeneration of initial $Ta_8O_2^+$. The text of the chapter is based on the publication "Catalytic Non-Oxidative Coupling of Methane on $Ta_8O_2^+$" written by N. Levin, J. Lengyel, J. F. Eckhard, M. Tschurl, and U. Heiz (Technical University of Munich, Chair of Physical Chemistry)[149].

3.1 Results

Tantalum-oxide clusters are produced in the laser vaporization cluster source (section 2.1.1). Oxygen (Air Liquide, 5.5) was injected into the nozzle to enable the formation of oxides. The ion trap was filled with mixtures of helium with either CH_4 (Rießner-Gase, 5.5) or CD_4 (Cambridge Isotope Laboratories, 99%). The content of methane in the mixture amounted to 20 ppm (0.02 %). Figure 3.1(a-c) displays the mass spectra reflecting the products of reactions between $Ta_8O_2^+$ and CD_4 in the REIT for specific storage times and temperatures. The mass difference between H and D makes the mass spectra for the reaction with CD_4 to be better resolved and more

demonstrative; however, the discussion and conclusions given below are applicable to the reaction with CH_4 too (Fig. 3.6). As can be seen in the Fig. 3.1a, the only detectable product in the reaction between $Ta_8O_2^+$ and CD_4 at room temperature is a carbene $[Ta_8O_2CD_2]^+$. It originates from the dehydrogenation of methane, a reaction which was previously observed for various Ta-based clusters[109–112]. Normally, the reaction of dehydrogenation proceeds in gas phase with full conversion of an initial cluster to a carbene species. This is not the case, however, for the reaction of $Ta_8O_2^+$: as can be seen in Fig. 3.1d, the reaction proceeds until the intensities of the initial cluster and its carbene reach a steady state.

At lower temperatures, additional peaks appear on the mass spectra. The new peaks at 169 K can be assigned to $[Ta_8O_2(CD_4)]^+$ and $[Ta_8O_2CD_2(CD_4)]^+$. They result from the association between methane and $Ta_8O_2^+$ and $[Ta_8O_2CD_2]^+$ respectively. At even lower temperatures, for example at 147 K, two more peaks appear with stoichiometries $[Ta_8O_2(CD_4)_2]^+$ and $[Ta_8O_2CD_2(CD_4)_2]^+$, which can be assigned to the products of further association with methane. Regardless of the temperature, the main reaction channel — namely, dehydrogenation of methane on $Ta_8O_2^+$ — exhibit the same behaviour: after the reaction starts, the intensity of the cluster-carbene species grows on the expense of the initial cluster $Ta_8O_2^+$ until a steady state is reached. At lower temperatures, in parallel with this process, the intensities of these two ions continue to slowly decrease because of the reactions of methane physisorption, until the only observable ions are the products of these association reactions (Fig. 3.1e,f).

3.1.1 Comparison of Kinetic Models

Thorough analysis of the reaction kinetics can help unravel mechanisms of the formation of observed products. At 300 K, when the abundance of the products of methane physisorption is negligibly small and cannot be detected, the two observed compounds, namely $Ta_8O_2^+$ and $[Ta_8O_2CD_2]^+$, coexist in a steady state, and the corresponding reactivity can be formally described in terms of a chemical equilibrium:

$$r_1 = k_1^{(1)}[Ta_8O_2^+] = r_{-1} = k_{-1}^{(1)}[Ta_8O_2CD_2^+], \qquad (3.1)$$

where r_1 and r_{-1} are reaction rates and $k_1^{(1)}$ and $k_{-1}^{(1)}$ are corresponding pseudo-first-order rate constants.

The comparison of different kinetic models for the reactions at lower temperatures reveals the role of the products of methane physisorption in the overall reaction mechanism (Figures 3.2). The results show, that the ions $Ta_8O_2CD_4^+$ and $Ta_8O_2CD_2CD_4^+$ represent the products of the reversible side reactions of intact CH_4 adsorption (Fig. 3.2b). These ions can therefore be interpreted as products of weak intact adsorption of methane on the corresponding cluster with an unfavourable adsorption geometry, what hampers the further reaction of methane dehydrogenation. This reasoning can be extended to the reaction model for even lower temperatures.
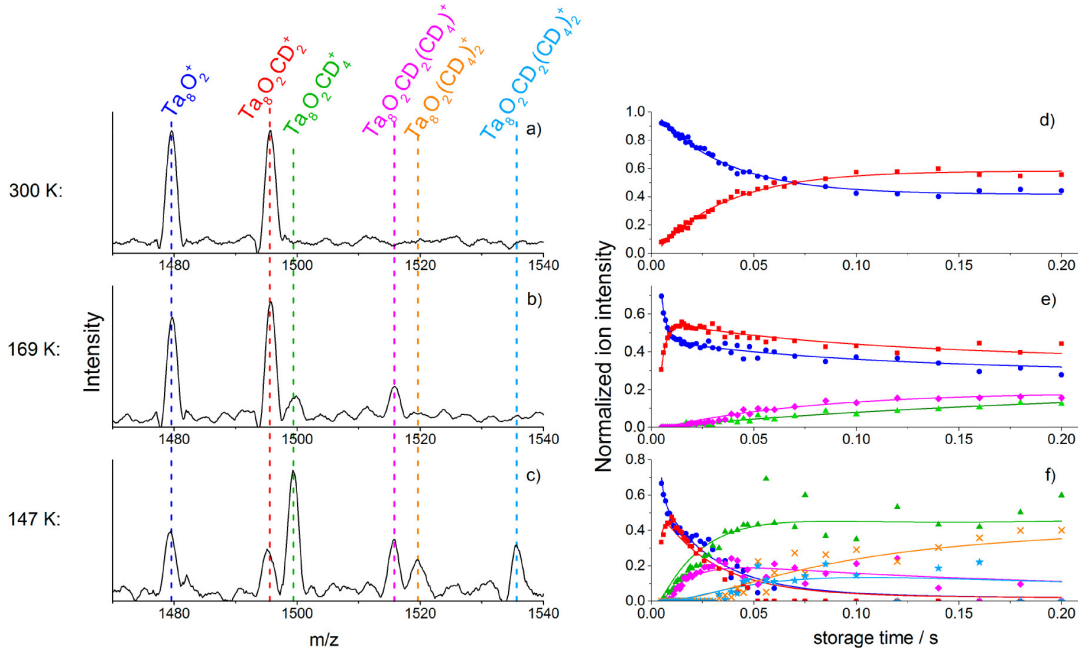
FIGURE 3.1: Left: mass spectra of the $Ta_8O_2^+$/CD_4-system measured at the storage time of 0.06 s. Right: pseudo-first-order kinetic fits of the reaction between $Ta_8O_2^+$ and CD_4. The experimental data points correspond to the normalized intensities of the reactants, intermediates, and products marked as follows: ■ $Ta_8O_2^+$, ● $Ta_8O_2CD_2^+$, ▲ $Ta_8O_2CD_4^+$, ◆ $Ta_8O_2CD_2CD_4^+$, × $Ta_8O_2(CD_4)_2^+$, ★ $Ta_8O_2CD_2(CD_4)_2^+$. Mass spectra and kinetic fits correspond to the various temperatures of the reaction system: 300 K (a, d), 169 K (b, e), and 147 K (c, f). Reprinted with permission from [149].

Similarly, the ions $Ta_8O_2(CD_4)_2^+$ and $Ta_8O_2CD_2(CD_4)_2^+$ are the products of the side-reaction physisorption of an additional methane molecule. The solid lines in the Fig. 3.1 denote the kinetic traces corresponding to this model.

The discovery of a correct kinetic model that best fits the experimental data does not provide insight into the real mechanisms underlying the observed reactivity. For example, the apparent steady state between $Ta_8O_2^+$ and $[Ta_8O_2CD_2]^+$ can be explained in terms of three different scenarios within the same kinetic fit: a genuine chemical equilibrium between these two compounds (Eq. 3.2), existence of at least two isomers of $Ta_8O_2^+$ with significantly differing reactivities (Eq. 3.3), and a full catalytic cycle, in which coupling of two methane molecules is mediated by a $Ta_8O_2^+$ cluster with its subsequent regeneration(Eq. 3.4). Therefore, additional experiments on the reaction kinetics must be carried out in order to distinguish these three scenarios.

$$Ta_8O_2^+ + CH_4 \rightleftharpoons Ta_8O_2CH_2^+ + H_2 \tag{3.2}$$

$$(Ta_8O_2^+)_{isom.\ 1} + CH_4 \longrightarrow Ta_8O_2CH_2^+ + H_2 \tag{3.3a}$$

$$(\text{Ta}_8\text{O}_2{}^+)_{isom.\ 2} + \text{CH}_4 \not\longrightarrow \tag{3.3b}$$

$$\text{Ta}_8\text{O}_2{}^+ + \text{CH}_4 \longrightarrow \text{Ta}_8\text{O}_2\text{CH}_2{}^+ + \text{H}_2 \tag{3.4a}$$

$$\text{Ta}_8\text{O}_2\text{CH}_2{}^+ + \text{CH}_4 \longrightarrow \text{Ta}_8\text{O}_2{}^+ + \text{C}_2\text{H}_6 \tag{3.4b}$$
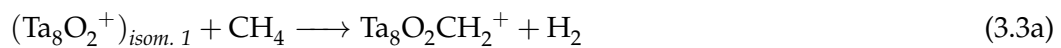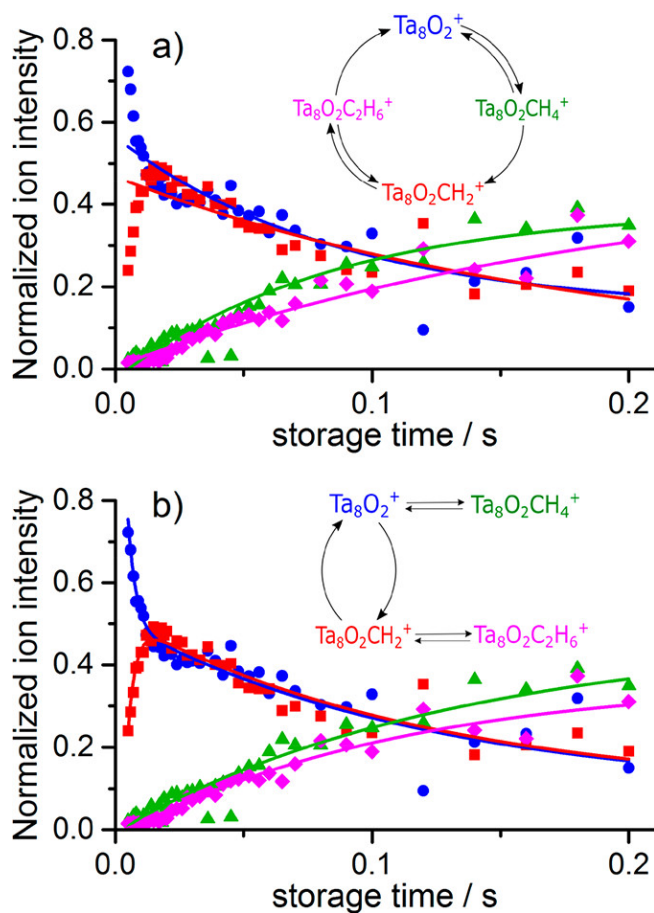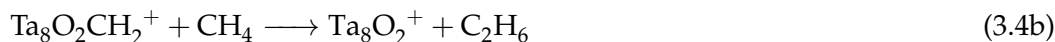
FIGURE 3.2: Kinetic fits corresponding to two different models of the reaction between Ta_8O_2^+ and CH_4 at 163 K. Panel (a): the product of the methane adsorption on Ta_8O_2^+ observed in the mass spectrum reacts further to form $\text{Ta}_8\text{O}_2\text{CH}_2^+$. The latter adsorbs another molecule of methane to form a cluster-ethane complex which further dissociates to release C_2H_6. Panel (b): Ta_8O_2^+ and $\text{Ta}_8\text{O}_2\text{CH}_2^+$ coexist in a steady-state equilibrium, whereas the side reactions of methane physisorption occur in parallel. The kinetic fits by additional models are shown in Fig. 3.9. Reprinted with permission from [149].

3.1.2   Variation of Methane Partial Pressure

The hypothesis of a chemical equilibrium (Eq. 3.2) between Ta_8O_2^+ and $[\text{Ta}_8\text{O}_2\text{CH}_2]^+$ is not tenable due to the following reasoning: first, the concentration of H_2 in the ion trap during the experiment is insignificant in comparison to that of methane, and

the rate of the reverse reaction is therefore too low to account for the regeneration of the initial $Ta_8O_2^+$ cluster. Moreover, as shown in the Fig. 3.3, the apparent rate coefficients yielded from the fits of the Eq. 3.1 scale linearly with the concentration of methane not only for the "forward" reaction of the methane dehydrogenation, but also for the reaction back to $Ta_8O_2^+$. With the involvement of the Eq. 2.13, this implies that the values of the bimolecular rates for both forward and reverse reactions scale linearly with the concentration of methane, which contradicts with the formulation of the equilibrium given in Eq. 3.2. It can thus be concluded, that the observed steady state cannot be assigned to a chemical equilibrium.
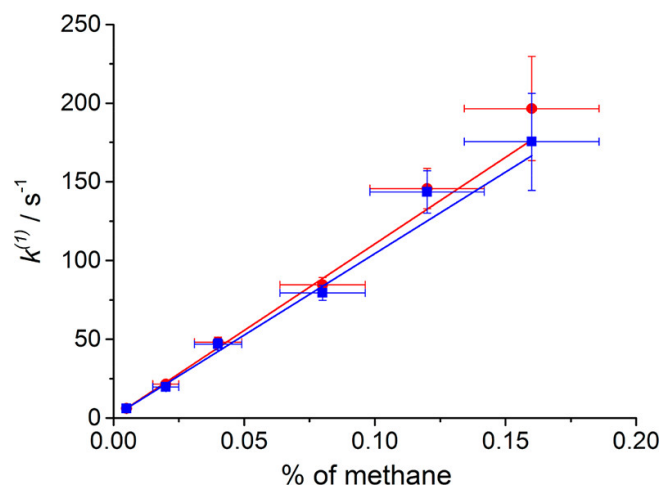
FIGURE 3.3: Values of apparent pseudo-first-order rate coefficients $k_1^{(1)}$ (red circles) and $k_{-1}^{(1)}$ (blue squares) corresponding to the reaction 3.1 plotted against the proportion of methane in the helium mixture at total pressure of 0.88 Pa. Reprinted with permission from [149].

3.1.3 Kinetic Isotopic Effects

For the further investigation of the reactivity of $Ta_8O_2^+$ towards methane, it is necessary to appeal to the notion of kinetic isotope effect (KIE). KIE is reflected in a change of a reaction rate, when one or several nuclei in reactant molecules are substituted by their isotopologues. For the reactions of methane activation, which involve either CH_4 or CD_4, this effect is quantitatively expressed as

$$KIE = 0.9 \cdot \frac{k_{C-H}}{k_{C-D}},$$ (3.5)

where k_{C-H} and k_{C-D} are rate coefficients of reactions with CH_4 and CD_4 respectively, and the factor 0.9 accounts for the difference between collisional cross-sections of CH_4 and CD_4[111, 112]. The phenomenon of intramolecular KIE originates from the change of zero-point vibrational energy of a bond (E_0 in Eq. 2.20). In a simple model of a harmonic oscillator (Eq. 2.19), a chemical bond is approximated as a spring with an oscillation angular frequency $\omega = \sqrt{\dfrac{k}{\mu}}$, where k is the zero-order

force constant of the oscillator and μ is the reduced mass of the molecule. There-
fore, for a bond formed between two nuclei with masses M and m (M $\gg$ m), the
angular frequency can be rewritten as $\omega \approx \sqrt{\dfrac{k}{m}}$. In a C-H bond, the substitution
of the H-atom by a D-atom leads to the reduction of the oscillation frequency by the
factor of $\sqrt{2}$. In order to dissociate, a chemical bond in the ground vibrational state
needs to absorb the amount of energy that equals to a dissociation energy D_0 (Fig.
2.5). Therefore, for a reaction of dissociation, $-k_B T \ln(k) = D_0 = D_e - E_0$, where k is
a reaction rate coefficient and D_0 is the depth of the potential well of the oscillator.
Therefore, the theoretical value of KIE for the reaction of C-H bond dissociation is
given by

$$\frac{k_{\text{C-H}}}{k_{\text{C-D}}} = \exp\left(\frac{\hbar \omega_H (1 - \sqrt{\frac{1}{2}})}{2k_B T}\right), \tag{3.6}$$

where $k_{\text{C-H}}$ and $k_{\text{C-H}}$ are rates of C-H and C-D dissociation, and ω_H is a C-H oscil-
lation frequency. This simple model is applicable to very exothermic reactions that
proceed as simple H-atom abstraction, and relatively low values of KIE (1.3—1.5)
are expected for such systems[150]. Rates of more complex reactions with multiple
transition states may have more intricate dependence on the isotopic composition
of involved molecules. Therefore, values of KIE can specify the nature of a rate-
limiting step and thus clarify the mechanism of a reaction [150]. For example, KIEs
below ~1.3 bring evidence that a rate-limiting step is not related to the bond scission,
but rather to the release of a product[151, 152] or to the cross-over between two spin
surfaces[153, 154], whereas high KIEs can be indicative of σ-bond metathesis[155],
multiple C-H bond scissions[111], or the formation of an insertion intermediate H-
M-CH$_3$[156].

In this work, reactions with methane isotopologues were used to probe the na-
ture of the steady state between the initial cluster $Ta_8O_2^+$ and $[Ta_8O_2CH(D)_2]^+$. Rate
coefficients for the reactions with CH_4, CD_4 and the corresponding KIE values are
listed in Table 3.2, Table 3.3, and Table 3.4 respectively. The values of the KIE are
below two, what makes the reaction of methane dehydrogenation by $Ta_8O_2^+$ similar
to that by the atomic tantalum cation[82]. Moreover, these two ions carry out this re-
action in the gas phase at similar rates ($k^{(2)} = 1.15 \cdot 10^{-9}$ cm^3 s^{-1} for Ta$^+$ at 300 K, and
$k^{(2)} = 7.00 \cdot 10^{-10}$ cm^3 s^{-1} for $Ta_8O_2^+$ at 300 K). Therefore, the theoretical treatment of
the reactivity of Ta$^+$ towards methane might be applied to the reactivity of $Ta_8O_2^+$.
For example, as noted by Parke *et al.*, the Ta$^+$/CH$_4$ system must undergo spin re-
arrangements at the reaction entrance channel in order to match the experimental
observation of the barrierlessness of the dehydrogenation reaction[136], what can
explain the comparatively low KIE values and reaction rates. Alternatively, the for-
mation of a hydrogen molecule may have rather high barriers and therefore can be
the rate-determining step, as was previously exemplified in the study of Ta$^+$[136].
The relatively low KIE values of the regeneration of $Ta_8O_2^+$ can be associated with
a high-barrier of the coupling reaction between two carbon atoms, as this process is

not affected by the isotopic substitution of the hydrogen atoms.

Furthermore, the comparison of the kinetics of $Ta_8O_2^+$ towards activation of different methane isotopologues proves the invalidity of the concept, that suggests the explanation of the steady state by the presence of isomers with significantly different reactivities. Several considerations must be noted for this interpretation. First, if there were multiple isomers that reacted with methane with different rates, then the initial cluster $Ta_8O_2^+$ would eventually completely turn into the product $[Ta_8O_2CH_2]^+$, and the corresponding kinetic traces in Fig 3.1b would not exhibit the steady-state behaviour. Second, the same result would be received even if one or several isomers were unreactive, but interconversion between all the isomers was feasible (*i.e.* they could transform into each other[157]). In this case the equilibrium between isomers would be shifted toward the reactive ones due to their continuous removal from the reaction. As a result, the conversion of all $Ta_8O_2^+$-clusters would eventually be achieved. Lastly, in the case of kinetically trapped unreactive isomers, the ratio of the intensity of the bare cluster to that after the dehydrogenation reaction is not expected to be affected by the isotopic composition of methane. Indeed, assuming that the distribution of isomers generated in the cluster source remains the same all the time, the share of unreactive ones would stay identical in all the experiments, and the reaction would proceed until the steady state with the same ratio $\dfrac{[Ta_8O_2CH(D)_2^+]_{eq}}{[Ta_8O_2^+]_{eq}}$ is reached. Figure 3.4a shows that this, however, is not the case, what already makes the explanation by unreactive isomers doubtful. Such behaviour (Fig. 3.4a) does not contradict though the hypothesis of a catalytic cycle, as reaction rates of dehydrogenation and liberation of the product may depend differently on the isotopic composition of methane.
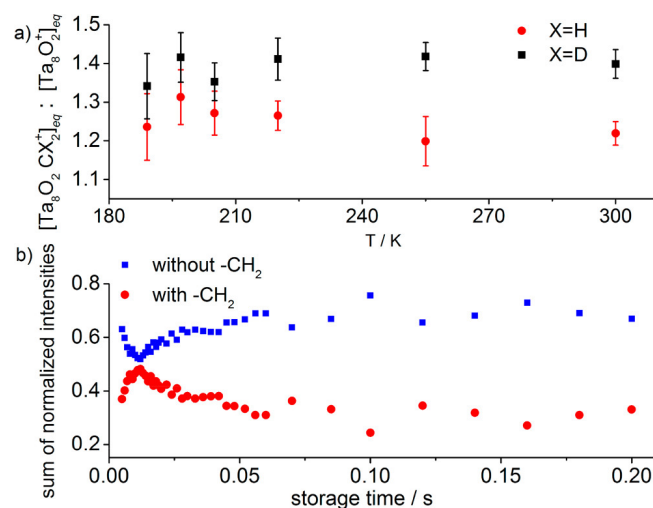
FIGURE 3.4: (a) Ratios $\dfrac{[Ta_8O_2CH_2]_{eq}^+}{Ta_8O_2^+}$ (red circles) and $\dfrac{[Ta_8O_2CD_2]_{eq}^+}{Ta_8O_2^+}$ (black squares) reflecting the steady state of the reaction at different temperatures. (b) Evolution of the total normalized intensities of ions, containing (red circles) and not containing (blue squares) a carbene moiety for the reaction of $Ta_8O_2^+$ with CH_4 at 147 K. Reprinted with permission from [149].

An even stronger evidence against the "isomers"-theory is demonstrated in Fig. 3.4b. In this figure, the sums of the normalized intensities of ions containing and not containing a -CH$_2$ moiety are plotted against the storage time (see figure caption for details). The occurrence of the maximum (or the minimum, respectively) cannot be explained by the presence of unreactive isomers, because in this case the "flat" behaviour would be expected. A reaction cycle in turn provides an adequate model of this observation. Indeed, the rates of dehydrogenation and product formation in the cycle are significantly higher than the rates of the side-reactions of methane physisorption. This quickly leads to the establishment of the steady state over the initial period of time limited by the extremum around 15 ms in Fig. 3.4b. After some time, the intensities of the products of methane physisorption become significant. Since the physisorption occurs faster on the bare Ta$_8$O$_2^+$ than on the [Ta$_8$O$_2$CX$_2$]$^+$-clusters, the summed intensities of all ions containing the -CH$_2$ motif slowly decreases in time, until the only species present in the system are the products of physisorption. All the considerations are summarized in Figure 3.5. It gives a clear evidence that the reaction occurs *via* the catalytic cycle shown in Scheme 3.1.

3.2 Discussion

FIGURE 3.5: Summary of possible scenarios to explain the reaction behaviour. The catalytic cycle (first column) is the only model that provides an adequate treatment of the experimental observations. The interpretation based on the presence of unreactive isomers (columns two and three) cannot explain the formation of the steady state or the observed kinetic isotope effects. The suggestion of the chemical equilibrium between Ta$_8$O$_2^+$ and [Ta$_8$O$_2$CH$_2$]$^+$ does not agree with the linear dependence of the reaction rates on the methane partial pressure. Reprinted with permission from [149].

The kinetic experiments on small metal clusters are usually reinforced by DFT calculations of potential energy surface (PES), along which the reaction system evolves. The Ta$_8$O$_2^+$ cluster however represents a too complex system, and accurate calculations of the corresponding PES would be very demanding. Even the structure of this ion could not be confidently established in the experiment, as the assignment of its IR vibrational spectrum was not unequivocally possible[158]. Nevertheless, even
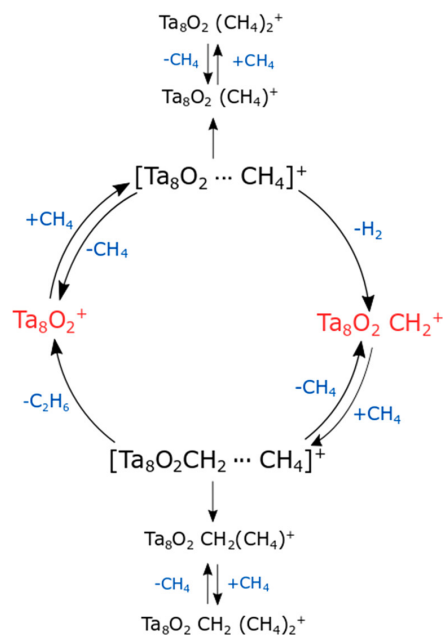
SCHEME 3.1: Proposed catalytic cycle for the reaction of $Ta_8O_2^+$ with methane. Reprinted with permission from [149].

though the detection of neutral reaction products is hampered by their extremely low concentrations, some conclusions about the products of the cycle can be made based on the thermochemical considerations and comparison to the literature. First, among all possible products of C-C coupling reactions (see Table 3.1), ethane is the most stable from the perspective of thermochemistry, even though the reaction of its formation from two molecules of methane is already endorgonic. This does not contradict with the observation of the reaction in the REIT experiment, because in a system starting without any reaction products, their formation is thermodynamically favored, as long as the overall Gibbs free energy of the system ($\Delta_r G°$) is negative, and the equilibrium concentrations are not reached. The temperature dependence of the reactions in the cycle is, at first sight, at odds with their endergonicity. This behavior, however, has already been described previously for a different system and can be explained by a combination of an adsorption pre-equilibrium and an apparent activation energy lower than the endothermic potential of the reaction[159]. Second, the formation of ethane and molecular hydrogen was observed for tantalum-hydride-doped silica catalysts[160]. The comparison of this work to the study of $Ta_8O_2^+$ reveals numerous similarities in the reaction mechanisms in both systems (Scheme 3.2), even though the differences in their reaction environments and compositions of catalysts are significant. Analogously to the mechanism proposed for the activation of methane by $Ta_8O_2^+$, Soulivong $et\ al.$ also discovered that the catalytic cycle initiates through the formation of carbene species in the reaction of methane dehydrogenation[160]. This carbene further undergoes a C-C coupling with another molecule of methane, and the cycle closes with the elimination of an ethane molecule. The details of the coupling mechanisms proposed for the gas-phase $Ta_8O_2^+/CH_4$ system and supported tantalum hydride are, however, different. For the latter, the crucial step

TABLE 3.1: Thermochemistry for the possible reactions at standard temperature and pressure. For all individual reactions, standard molar enthalpies $\Delta_r H^\circ$/Gibbs energies of formation $\Delta_r G^\circ$ are taken from Ref. [161]. Furthermore, the equilibrium constant (K) is calculated from the equation K = exp($-\Delta_r G^\circ$/RT). (R denotes the gas constant with a value of 8.314 J/(K·mol).)

Reaction	$\Delta_r H^\circ (298K)$ / kJ mol^{-1}	$\Delta_r G^\circ (298K)$ / kJ mol^{-1}	K (298 K)
$2\,CH_4 \longrightarrow C_2H_6 + H_2$	65.2	69.0	$8.0 \cdot 10^{-13}$
$2\,CH_4 \longrightarrow C_2H_4 + 2\,H_2$	201.6	169.4	$2.0 \cdot 10^{-30}$
$2\,CH_4 \longrightarrow C_2H_2 + 3\,H_2$	376.6	310.9	$3.2 \cdot 10^{-55}$
$2\,CH_4 \longrightarrow 2\,CH_3^\cdot + H_2$	440.6	396.8	$2.8 \cdot 10^{-70}$

of methane activation is the HAT enabled by a carbene-hydride, which results in the formation of methyl and elimination of an H_2. This methyl couples with the carbene group which in turn brings about a HAT from another methane molecule. Finally, a C_2H_6 is desorbed, and the remaining methyl reacts to form a carbene and hydride (Scheme 3.2). In contrast, potential methyl species formed in the course of the gas-phase reaction between $Ta_8O_2^+$ and CH_4 were not detected on our experiment, and the kinetic analysis suggests that the coupling occurs directly *via* activation of the second methane molecule by the carbene intermediate. Another difference to the observations made by Soulivong *et al.* is that no side-reactions like further dehydrogenation or the migration of methyl groups[160] were observed in the gas-phase experiment.
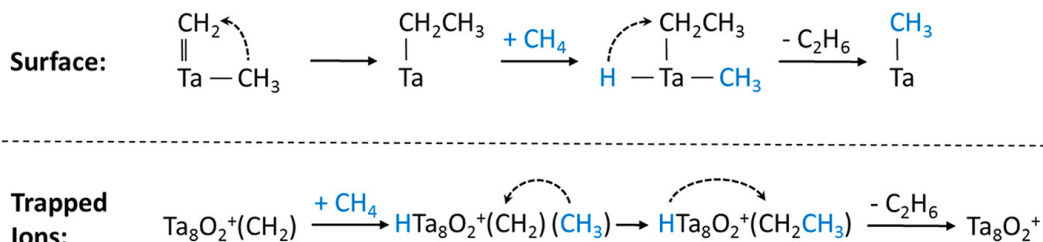
SCHEME 3.2: Comparison of the proposed reaction mechanism for the catalytic non-oxidative coupling of methane to ethane by supported silica-hidrides (top) and gas-phase $Ta_8O_2^+$ (bottom). Reprinted with permission from [149].

The reaction of catalytic non-oxidative coupling of methane (NOCM) to ethane in gas-phase was also observed on Pd_2O^+ [147]. The reaction conditions in this work are similar to the ones described in the Thesis with the multi-collisional thermalisation of clusters enabled in the reactor. The exact mechanism of methane coupling in this reaction system however differs significantly from the one proposed for $Ta_8O_2^+$ and is much less unambiguous. It was suggested by the authors, that the reaction of methane dehydrogenation, which similar to the reaction on $Ta_8O_2^+$ leads to the formation of carbene, occurs only after cooperative coadsorption of three methane molecules on Pd_2O^+ (Scheme 3.3). Since collisional stabilization of physisorbed

species is more efficient at lower temperatures (because only the reaction of desorption, denoted by the reaction coefficient k_b in the Eq. 2.4, depends on the temperature), the reaction was only observed at the temperatures around 260 K. After the reaction of methane dehydrogenation, which leads to the formation of $Pd_2OC_3D_{10}^+$, a molecule of ethane is released thus reforming a $Pd_2OCD_4^+$ (Scheme 3.3). Therefore, not the Pd_2O^+ cluster itself takes part in the catalytic cycle, but rather its methanated form.
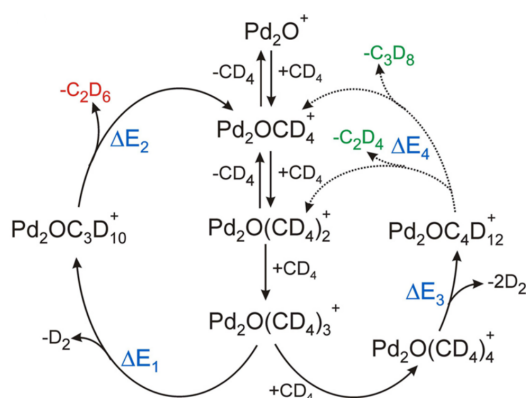
SCHEME 3.3: Proposed reaction mechanism for the reaction of Pd_2O^+ with methane. Adopted from [147].

3.3 Summary

Conversion of methane mediated by $Ta_8O_2^+$ in the gas phase proceeds through a catalytic cycle, in which two molecules of CH_4 couple to form ethane and molecular hydrogen. Thorough kinetic analysis involving pressure- and temperature-dependant experiments as well as isotopic substitution of CH_4 with CD_4 allows to discard interpretations suggesting the presence of unreactive isomers or a backward reaction. At room temperature, the formation of the products of methane intact adsorption is not observed; however, at lower temperatures these side reactions poison the catalytic conversion. This reaction of NOCM was compared to its previous examples — namely, by supported silica-hidrides and by gas-phase Pd_2O^+. The reaction mechanisms proposed for all three reaction systems demonstrate significant differences; however, the process of C-C coupling itself most likely proceeds through the same steps.

3.4 Supplementary Information

Listed below (Eq. 3.7) are the reactions occurring in the catalytic cycle, described in detail in the previous sections. The rate coefficients are denoted as k_i, and their values are listed in Table 3.2 for the reactions with CH_4 and in Table 3.3 for the reactions with CD_4. Note, that in Eq. 3.7a k_1 corresponds to the reaction of methane dehydrogenation, whereas k_{-1} stands for the $Ta_8O_2^+$ regeneration reaction.

$$Ta_8O_2^+ \underset{k_{-1}}{\overset{k_1}{\rightleftharpoons}} Ta_8O_2CH_2^+ \tag{3.7a}$$

$$Ta_8O_2^+ \underset{k_{-2}}{\overset{k_2}{\rightleftharpoons}} Ta_8O_2(CH_4)^+ \tag{3.7b}$$

$$Ta_8O_2CH_2^+ \underset{k_{-3}}{\overset{k_3}{\rightleftharpoons}} Ta_8O_2CH_2(CH_4)^+ \tag{3.7c}$$

$$Ta_8O_2(CH_4)^+ \underset{k_{-4}}{\overset{k_4}{\rightleftharpoons}} Ta_8O_2(CH_4)_2^+ \tag{3.7d}$$

$$Ta_8O_2CH_2(CH_4)^+ \underset{k_{-5}}{\overset{k_5}{\rightleftharpoons}} Ta_8O_2CH_2(CH_4)_2^+ \tag{3.7e}$$
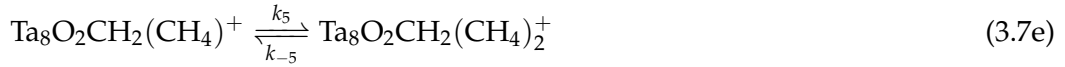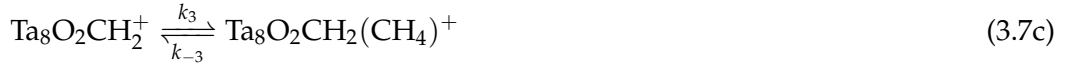
TABLE 3.2: Termolecular rate constants ($k^{(3)}$) of forward reactions including $k_{-1}^{(3)}$ (in 10^{-24} $cm^6\ s^{-1}$) and bimolecular rate constants ($k^{(2)}$) of true back reactions (in $10^{-14}\ cm^3\ s^{-1}$) of the catalytic non-oxidative coupling of CH_4 on $Ta_8O_2^+$. The labelling follows Eq. 3.7. The absolute error of 50% is estimated by the uncertainty of the pressure gauge, which is expected to represent the largest contribution.

T	$k_1^{(3)}$	$k_{-1}^{(3)}$	$k_2^{(3)}$	$k_{-2}^{(2)}$	$k_3^{(3)}$	$k_{-3}^{(2)}$	$k_4^{(3)}$	$k_{-4}^{(2)}$	$k_5^{(3)}$	$k_{-5}^{(2)}$
300	3.3	2.7								
255	6.0	5.0								
220	6.7	5.3								
205	7.3	5.7								
197	7.7	5.9								
189	10.6	8.6								
182	13.2	11.2	0.3	2.5						
157	20.4	22.9	0.9	<0.1	0.9	0.7	0.2	3.8	0.2	<0.1
152	21.9	24.8	1.8	<0.1	1.1	<0.1	1.0	13.2	0.6	2.5
147	24.1	26.7	2.5	<0.1	1.7	1.2	0.8	6.6	1.1	3.3
142			3.2	<0.1	2.3	4.1	1.1	7.2	1.5	2.4

TABLE 3.3: Termolecular rate constants ($k^{(3)}$) of forward reactions including $k_{-1}^{(3)}$ (in 10^{-24} cm^6 s^{-1}) and bimolecular rate constants ($k^{(2)}$) of true back reactions (in 10^{-14} cm^3 s^{-1}) of the catalytic non-oxidative coupling of CD$_4$ on Ta$_8$O$_2^+$. The labelling follows Eq. 3.7. The absolute error of 50% is estimated by the uncertainty of the pressure gauge, which is expected to represent the largest contribution.

T	$k_1^{(3)}$	$k_{-1}^{(3)}$	$k_2^{(3)}$	$k_{-2}^{(2)}$	$k_3^{(3)}$	$k_{-3}^{(2)}$	$k_4^{(3)}$	$k_{-4}^{(2)}$	$k_5^{(3)}$	$k_{-5}^{(2)}$
300	1.8	1.3								
255	3.2	2.3								
220	4.0	2.9								
205	5.0	3.7								
197	5.1	3.6								
189	5.9	4.4								
182	6.7	5.1								
175	8.8	7.2	0.1	3.0						
169	13.3	10.9	0.1	0.8	0.3	3.2				
163	14.4	12.1	0.4	1.2	0.4	1.8				
152	14.8	15.0	1.0	<0.1	0.9	0.2			0.4	1.3
147	17.2	20.0	2.7	<0.1	1.7	3.9	0.6	3.8	1.2	8.5
142			3.9	<0.1	2.7	1.3	1.6	6.9	1.8	4.7

Table 3.4 displays the values of KIE corresponding to the reactions 3.7a. The values are calculated as described in the Eq. 3.5. Figure 3.6 exhibits mass spectra

TABLE 3.4: Kinetic isotope effect (KIE) corresponding to the reactions of the catalytic cycle.

T	KIE (k_1)	KIE (k_{-1})
300	1.62	1.85
255	1.69	2.00
220	1.50	1.68
205	1.31	1.39
197	1.37	1.48
189	1.62	1.76
182	1.76	1.99
152	1.33	1.49
147	1.26	1.20

reflecting the products of reactions between Ta$_8$O$_2^+$ and CH$_4$ in the REIT for specific storage times and temperatures and the kinetic fits of these reactions. Figures 3.7 3.8 show additional plots of the sums of the normalized intensities of ions containing and not containing a -CH$_2$ (-CD$_2$) moiety against the storage time.

Figure 3.9 represents additional kinetic models for the reaction between Ta$_8$O$_2^+$ and CH$_4$ in the REIT. None of these models is capable of reproducing the experimental data.
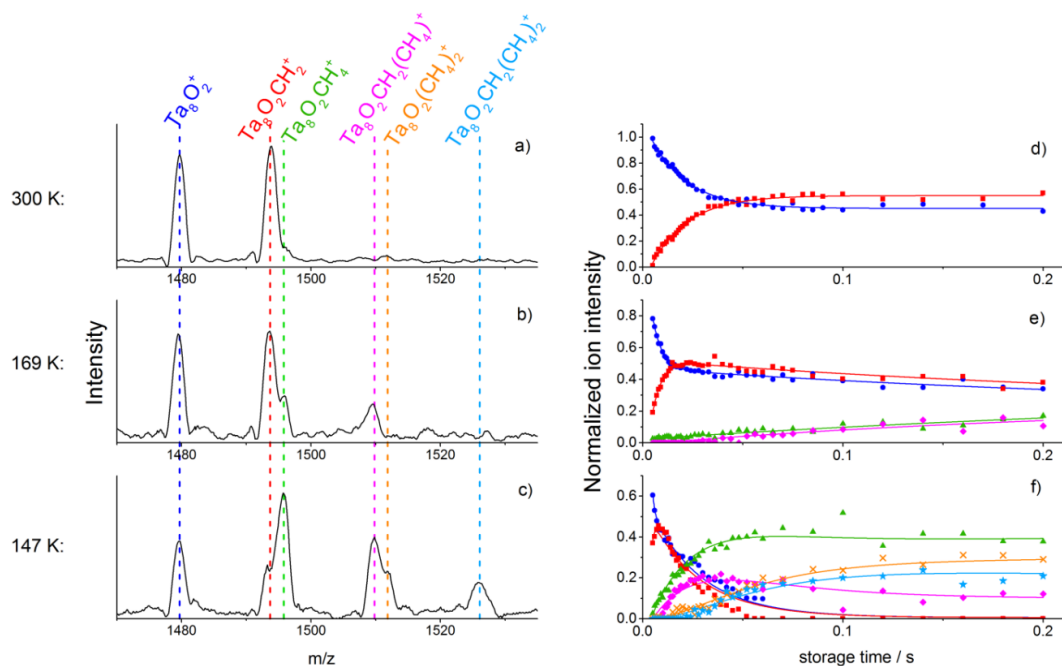
FIGURE 3.6: Left: mass spectra of the $Ta_8O_2^+$/CH_4-system measured at the storage time of 0.048 s (a), 0.1 s (b), and 0.036 s (c). Right: pseudo-first-order kinetic fits of the reaction between $Ta_8O_2^+$ and CH_4. The experimental data points correspond to the normalized intensities of the reactants, intermediates, and products marked as follows: ■ $Ta_8O_2^+$, ● $Ta_8O_2CH_2^+$, ▲ $Ta_8O_2CH_4^+$, ◆ $Ta_8O_2CH_2CH_4^+$, × $Ta_8O_2(CH_4)_2^+$, ★ $Ta_8O_2CH_2(CH_4)_2^+$. Mass spectra and kinetic fits correspond to the various temperatures of the reaction system: 300 K (a, d), 169 K (b, e), and 147 K (c, f). Reprinted with permission from [149].
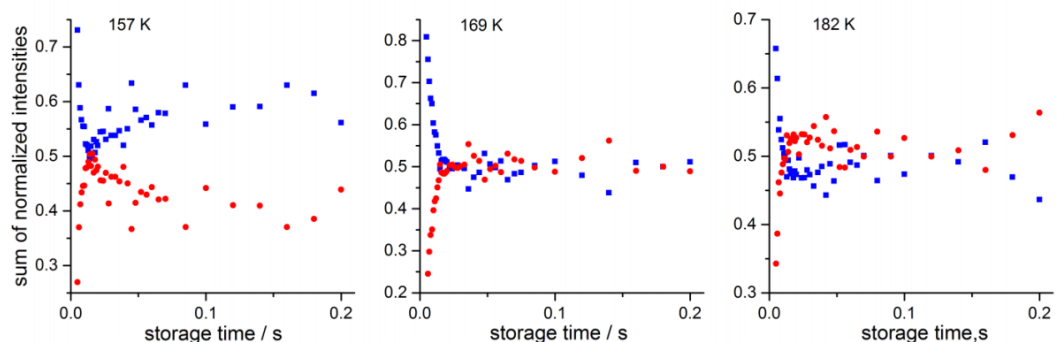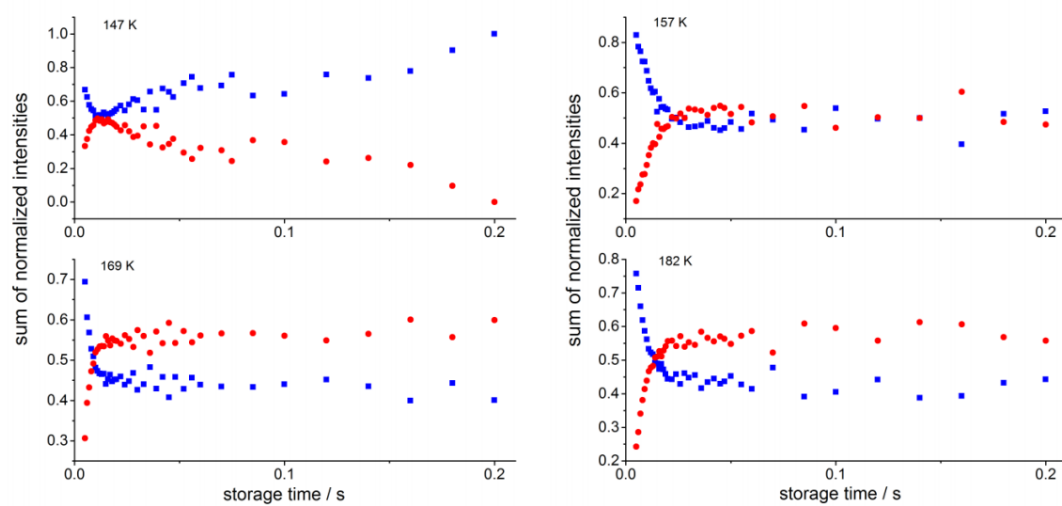

FIGURE 3.7: Sum of normalized intensities of ions containing a carbene-moiety (red), and ions not containing a carbene-moiety (blue) in the reaction of $Ta_8O_2^+$ with CH_4 at three different temperatures. Reprinted with permission from [149].

FIGURE 3.8: Sum of normalized intensities of ions containing a carbene-moiety (red), and ions not containing a carbene-moiety (blue) in the reaction of $Ta_8O_2^+$ with CD_4 at four different temperatures. Reprinted with permission from [149].

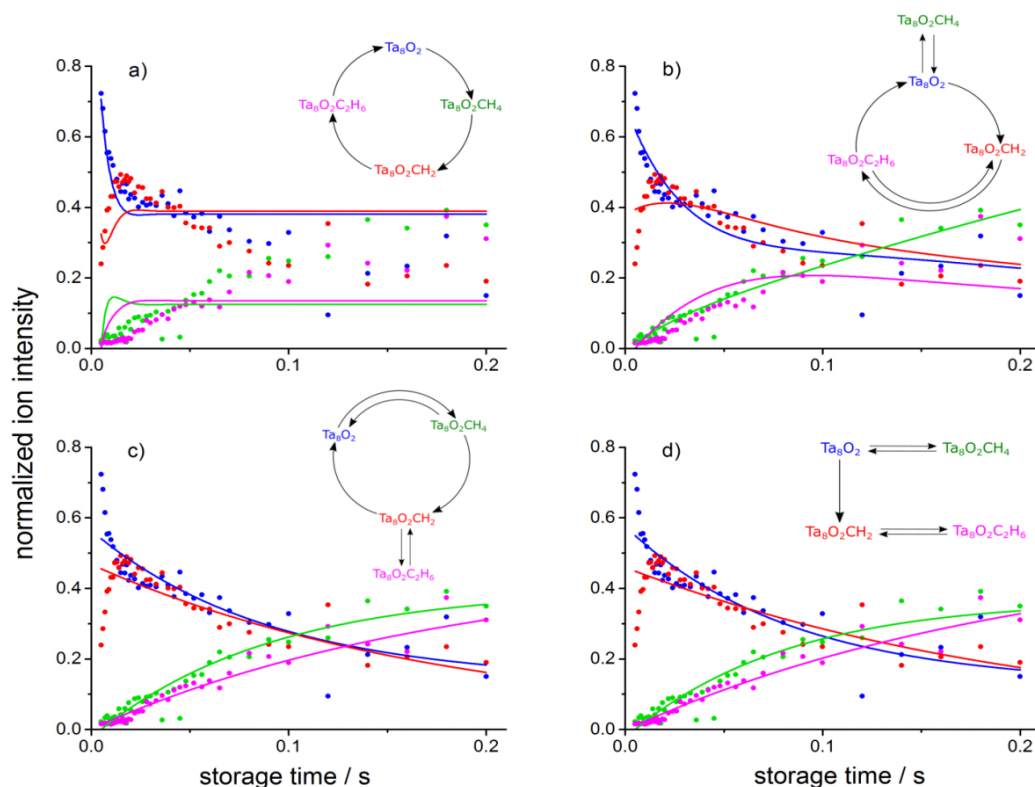FIGURE 3.9: Comparison of four additional reaction schemes of $Ta_8O_2^+$ with CH_4 at 163 K. The models are different to the two shown in the main chapter. a) Methane irreversibly adsorbs on $Ta_8O_2^+$ and then undergoes dehydrogenation to $[Ta_8O_2CH_2]^+$; the latter takes up another molecule of methane to irreversibly form $[Ta_8O_2C_2H_6]^+$, which further reacts to form the initial cluster. b) $Ta_8O_2^+$ reacts directly to form $[Ta_8O_2CH_2]^+$ in the reaction of methane dehydrogenation. The cluster-methylene complex transforms into $[Ta_8O_2C_2H_6]^+$ *via* methane physisorption, which is followed by the release of C_2H_6 and the regeneration of the bare cluster. In addition, a reversible clustering of methane on $Ta_8O_2^+$ occurs in the parallel reaction. c) Methane reversibly adsorbs on $Ta_8O_2^+$ to form $[Ta_8O_2CH_4]^+$, which converts into $[Ta_8O_2CH_2]^+$ in a single dehydrogenation step. The carbene reacts directly to the bare $Ta_8O_2^+$. The model includes the intact adsorption of methane on $[Ta_8O_2CH_2]^+$ in parallel to the main reaction channel. d) $Ta_8O_2^+$ transforms into $[Ta_8O_2CH_2]^+$ through a dehydrogenation process. The reaction back to $Ta_8O_2^+$ does not occur. Both species enable a reversible methane clustering. Reprinted with permission from [149].

4 Spectroscopic Identification of the [4Ta,C,2H]$^+$ Structure

IRMPD is an important analytical tool which provides information about structures of reaction intermediates, complementary to kinetic data. Knowledge about structures of intermediates and products provides insights about reaction mechanisms and thus facilitates the rational design of state-of-the-art catalysts. A rich body of literature addresses the problem of methane activation by charged transition metal atoms and clusters. In particular, the structures of the products of methane dehydrogenation by atomic cations of several metals were probed by IRMPD[162–167]. Prior to this work, the structural investigations of methane activation by clusters were limited only to the characterization of intermediates from the entrance channel (i.e.methane adsorption and insertion of the metal into the C-H bond) for cationic gold[168] and platinum[169, 170] clusters.

Previously, the DFT calculations supporting the study of methane activation by Ta$_4^+$ revealed that a carbide dihydride structure of the intermediate [Ta$_4$,C,2H]$^+$ is energetically preferred over a carbene structure[111]. This compound was found to be very reactive towards O$_2$, potentially enabling the formation of such products as syngas and/or formaldehyde[86]. It is therefore essential to determine the exact structure of the [4Ta,C,2H]$^+$ compound. It must be noted, that previous IRMPD studies of [M,C,2H]$^+$ structures identified exclusively carbenes (-CH$_2$) and carbyne hydrides (-H and -CH) moieties[162–167].

This chapter describes in details the IRMPD-characterization of [4Ta,C,2H]$^+$ supported by quantum chemical calculations. It demonstrates, that spectra of [4Ta,C,2H]$^+$ are dominated by vibrational bands of an H$_2$Ta$_4$C$^+$ carbide dihydride over those indicative for an HTa$_4$CH$^+$ carbyne hydride. This finding was verified by an experiment employing various methane isotopologues. The text of the chapter is based on the publication "Carbide Dihydrides: Carbonaceous Species Identified in Ta$_4^+$-Mediated Methane Dehydrogenation" written by J. Lengyel, N. Levin, M. Tschurl, U. Heiz (Technical University of Munich, Chair of Physical Chemistry), F. Wensink, O. Lushchikova, J. Bakker (Radboud University, Institute for Molecules and Materials, FELIX Laboratory), R. Barnett, and U. Landman (Georgia Institute of Technology, School of Physics)[171].

4.1 Results

The IRMPD spectra were obtained in the FELICE experiment at the FELIX lab, Nijmegen, the Netherlands. The parameters of the experiment are given in the section 4.3. The details of DFT computations performed by J. Lengyel, R. Barnett, and U. Landman can be found in the Supporting Information of the Ref. [171].

Figure 4.1 shows experimental IRMPD- and calculated DFT spectra of [4Ta,C,2H]$^+$ and some of its isotopologues. The experimental spectra correspond to the fragmentation into the channel of [4Ta,C]$^+$.
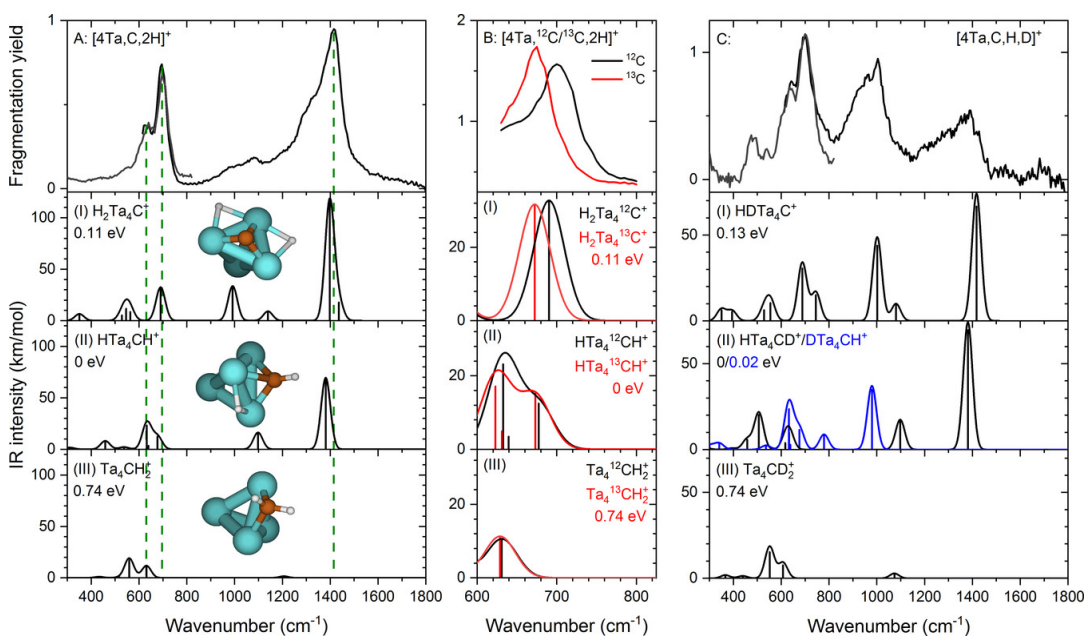
FIGURE 4.1: Top row: experimental IRMPD spectra of [4Ta,C,2H]$^+$ (A), [4Ta,^{12}C/^{13}C,2H]$^+$ (B), and [4Ta,C,H,D]$^+$ (C). Corresponding calculated spectra are displayed in rows I-III for three different structures, namely: carbide dihydride (I), carbyne hydride (II), and carbene (III). Modelling harmonic spectra were calculated and scaled at the PBE+D2/TZVP level of theory. The energy values (in units of eV) of various isomers are related to the lowest-energy structural isomer (marked as "0 eV"). Reprinted with permission from [171]

Two broad features are observed in the Fig. 4.1A at 695 and 1400 cm^{-1}. The former one has a shoulder at 630 cm^{-1}, indicating the presence of an additional band. Another low-intense resonance is situated between two most prominent bands. The calculated spectrum of a carbene isomer does not predict any peaks above 700 cm^{-1}, other than a tiny signal at 1200 cm^{-1}. In contrast, two other calculated spectra (for carbide dihydride and carbyne hydride) demonstrate a much better accordance with the experimental results. In particular, the experimental feature around 1400 cm^{-1} corresponds to the Ta-H stretch vibration, and the one around 695 cm^{-1} to the Ta-C bond stretching. These findings already suggest that the structure of [4Ta,C,2H]$^+$ most likely is represented not by carbene. However, a distinction between the other two proposed structures cannot be made based on this one experimental spectrum only. Therefore, the spectra of [4Ta,C,2H]$^+$ were compared to the spectra of its isotopologues. Fig. 4.1B shows the results of the experiment with the mixture of

$^{12}CH_4/^{13}CH_4$. Both gases were injected in the flow tube in a 1:1 proportion, and the IRMPD spectra were recorded for both isotopes simultaneously to avoid calibration errors. The substitution of ^{12}C with its ^{13}C isotope leads to the red-shift of about 27 cm^{-1} of the peak at 695 cm^{-1}. This peak, however, remains at the same position upon deuteration of methane (Fig. 4.1C), what confirms that it indeed derives from the vibration of a C-bond. The shift of a peak position upon isotopic substitution has an origin similar to that of the kinetic isotope effect (KIE), which is explained in the subsection 3.1.3. The best agreement with the experimental results is demonstrated by the calculated spectrum for carbide dihydride (Fig. 4.1B:I). The presence of carbyne hydride cannot be discarded nonetheless, even though the shift of the C-H vibrational frequency around 630 cm^{-1} is less pronounced upon $^{12}C/^{13}C$ substitution. It can be suggested therefore, that in Fig. 4.1A the peak at 695 cm^{-1} stems from Ta-C stretching in carbide dihydride, and the one at 630 cm^{-1} from the motion of a C-H group in carbyne hydride.

When one hydrogen atom in [4Ta,C,2H]$^+$ is replaced by a deuterium atom, several additional pronounced features appear in the IRMPD spectrum (Fig. 4.1C). The most intense of those is the peak around 1000 cm^{-1}. In the meantime, the intensity of the peak at 1400 cm^{-1} is remarkably reduced. The shifted positions of the peaks in [4Ta,C,H,D]$^+$ in comparison to [4Ta,C,2H]$^+$ can be attributed to the vibrational bands predicted by DFT-calculations (Fig. 4.1C:I-III). Thus, the new peak around 1000 cm^{-1} matches the Ta-D vibration in both carbide dihydride and carbyne hydride. This also explains the reduction of the intensity of the peak at 1400 cm^{-1}: as one of the H-atoms is replaces by a D-atom, the intensity of the Ta-H vibration declines accordingly. A further distinction based on the experimental spectrum of [4Ta,C,H,D]$^+$ is impeded by the similarity of the calculated spectra corresponding to these two structures.

Further investigation is based on the dissociation patterns of [4Ta,C,2D]$^+$, in which both hydrogen atoms are replaced by deuterium. Due to a very large KIE associated with dehydrogenation of methane by Ta$_4^+$[111], mass spectra of the Ta$_4^+$/CD$_4$ and Ta$_4^+$/CD$_2$H$_2$ systems are dominated by the product of the intact methane adsorption (Fig. 4.3). The IR-induced fragmentation of this species contaminates the fragmentation channel of [4Ta,C,2D]$^+$, which leads to the overlapping of vibrational features from [4Ta,C,2D]$^+$ and Ta$_4^+$(CD$_4$)/Ta$_4^+$(CH$_2$D$_2$). In order to deduce the effect of perdeuteration on dissociation energies, the IRMPD spectra of methane (CD$_4$ and CH$_2$D$_2$) complexes on [4Ta,C,2D]$^+$ were compared with the spectra of methane complexes on bare Ta$_4^+$ (Fig. 4.2A,B). Due to the phenomenon of internal vibrational energy redistribution and relatively low binding energies of adsorbates, a single act of fragmentation requires fewer photons what is reflected in less broadened spectral peaks [172]. However, the presence of loosely bound methane molecules brings in additional absorption bands in the spectra. As can be seen in Figures 4.2(A,B), these bands occur at the high-energy end of the spectra (above 900 cm^{-1}). This conclusion

can be made based on the similarity between spectral features of the methane complexes of both bare Ta$_4^+$ and [4Ta,C,2D]$_4$ in this energy region. In addition, ground state vibrational frequencies of free methane molecules[173], marked with dashed lines in Fig. 4.2(A,B), almost coincide with peak maxima. Slight mismatches between peak positions and dashed lines can result from the complexation with tantalum clusters. A split band at 690 and 720 cm^{-1} is not featured in the spectra of [4Ta]$^+$·(CD$_4$)$_n$ and [4Ta]$^+$·(CH$_2$D$_2$)$_n$, and it can be therefore concluded that it represents one of the adsorption bands of [4Ta,C,2D]$^+$. The DFT computations predict a Ta-C stretching and a Ta-D-Ta bending vibrations at 687 and 706 cm^{-1} in the carbide dihydride isomer, what perfectly matches the experimental spectra. However,

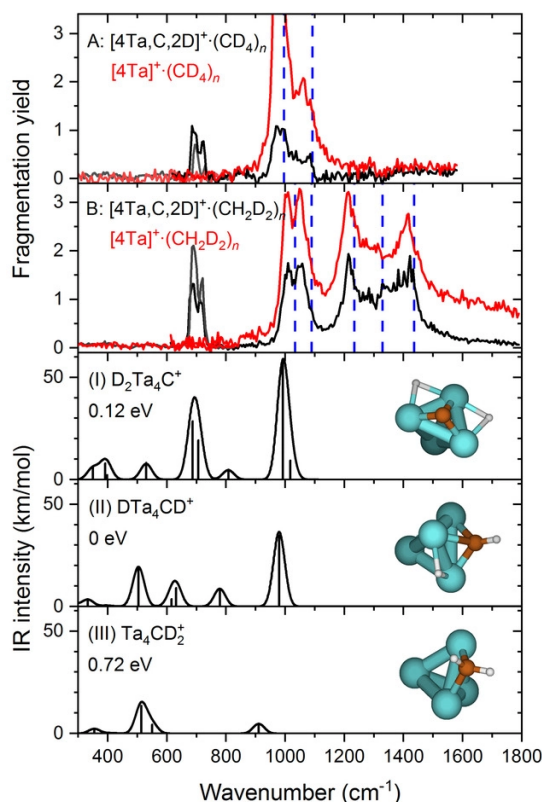FIGURE 4.2: Panel A: experimental IRMPD spectra of [4Ta,C,2D]$^+$·(CD$_4$)$_n$ (black line) and [4Ta]$^+$·(CD$_4$)$_n$ (red line). Panel B: experimental IRMPD spectra of [4Ta,C,2D]$^+$·(CH$_2$D$_2$)$_n$ (black line) and [4Ta]$^+$·(CH$_2$D$_2$)$_n$ (red line). Panels (I–III): modelled spectra of H$_2$Ta$_4$C$^+$ carbide dihydride (I), HTa$_4$CH$^+$ carbyne hydride (II), and Ta$_4$CH$_2^+$ carbene (III), calculated at the PBE+D2/TZVP level of theory. Experimental IR frequencies of free methane moieties are marked by vertical dashed lines[173]. The energy values (in units of eV) of various isomers are related to the lowest-energy structural isomer (marked as "0 eV"). Reprinted with permission from [171]

even though the same computations for both carbide dihydride and carbyne hydride suggest several peaks below 900 cm^{-1}, no signals in addition to the aforementioned doublet around 700 cm^{-1} were detected experimentally in this region. This can be explained by the low efficiency of the excitation of respective vibrational modes, what in principle agrees with relatively low calculated intensities of these peaks. Therefore, the presence of carbyne hydride can be neither discarded nor confirmed

based on this spectrum only.

4.2 Summary

The structure of the [4Ta,C,2H]$^+$-compound, an intermediate formed in the reaction of methane dehydrogenation by Ta$_4^+$, was investigated by means of IRMPD spectroscopy supported by DFT calculations of its various isomers. The analysis of the IR spectra did not show any features which would evidence the presence of a carbene isomer. The distinction between carbyne hydride and carbide dihydride is based on the examination of the IR patterns resulted from isotopic substitutions of the carbon and hydrogen atoms. Thus, the split band at 690 and 720 cm^{-1} was unambiguously assigned to a Ta-C stretching and a Ta-D-Ta bending vibrations in the carbide dihydride isomer. Such type of products of methane dehydrogenation has not been reported previously for other metal-cluster systems and was believed to be too endothermic to be considered[165, 166]. This study shows that this structure must not be neglected. The presence of the carbyne hydride structure of [4Ta,C,2H]$^+$ cannot be discarded though, as the bands at 630, 695, and 1400 cm^{-1} in its IR spectra can be assigned to the Ta-H and Ta-C vibrations.

The dominance of the carbyne hydride isomer can justify the formation of valuable products in the reactions of Ta$_4$CH$_2^+$ towards oxygen[86]. In this regard, IRMPD spectroscopy has again proved to be a valuable complementary technique to gas-phase kinetic experiments, and gas-phase studies in general have been demonstrated to be a useful tool to investigate the chemistry of metal-cluster catalysts.

4.3 Supplementary Information

Given below are the details of the experiment on the structural analysis of [4Ta,C,2H]$^+$ performed at the Free Electron Laser for Intra-Cavity Experiments (FELICE) facility. More specifically, the process of the cluster formation and the parameters of the laser radiation are described.

Charged tantalum clusters are generated in a Smalley-type laser ablation cluster source[62]. More specifically, a pulse of the second harmonic of a Nd:YAG laser (Quantel Brio, 80 mJ/pulse, 532 nm wavelength, 5 ns pulse length, 10 Hz repetition rate) ablates a rotating and translating metal rod driven by a two-phase stepper motor. The produced metal plasma expands into a molecular beam channel, one end of which is connected to a gas valve (General Valve Series 9, backing pressure up to 8 bar) to inject buffer gas, and the other one — to a copper reaction flow tube. The helium buffer gas enables cluster formation and plays the role of the cluster carrier. Reactant gases are injected in the flow tube *via* a pulsed valve (General Valve Series 9). Upon leaving the reaction channel, the ion beam first undergoes expansion into vacuum and is then shaped by a skimmer and a slit aperture to enter the interaction

chamber, where it interacts with an IR laser pulse. A pulse of high voltage applied to the ToF acceleration plates bends ions into the reflectron-ToF tube (R $\approx$ 1500), where the ion masses are recorded by a chevron-type microchannel plate detector.

During the experiments at FELICE, the molecular ion beam is studied inside the optical cavity of the FEL, which greatly enhances the intensity of the radiation accessible to the studied molecules and ions. In the FELICE experiment discussed in this thesis, the spectral range covered 300 to 1800 cm^{-1} and consisted of two regions corresponding to different energies of used electrons. The 8-μs-long macropulses were characterised by a spectral width (full-width at half-maximum) of ca. 0.6% of the central frequency and the repetition rate of 5 Hz. Their energy ranged from 0.5 at 1800 cm^{-1} to 1.1 J at 600 cm^{-1}, and the maximum IR fluence amounted to 5 J/cm^2 at 1800 cm^{-1}. Since FEL operates at 5 Hz frequency, and the Nd:YAG laser for cluster generation at 10 Hz, each measurement of fragments can be compared with an aforegoing measurement of parent ions. The resulting spectra are converted to laser-power corrected fragmentation yield $Y_f(\omega)$:

$$Y_f(\omega) = \ln\left(1 + \frac{I_f(\omega) - I(\omega)}{I_p(\omega)}\right), \tag{4.1}$$

where $I_f(\omega)$ and $I_p(\omega)$ are the integrated intensities of fragment and parent ions after IR laser irradiation at frequency ω, and and I_f is the integrated intensity of fragment ions without laser irradiation.

The IRMPD spectra recorded in this work represent the fragmentation-yield channel [4Ta,C,2H]$^+$ $\longrightarrow$ Ta$_4$C$^+$ + H$_2$. The endothermicity of this reaction calculated at PBE+D2/TZVP level of theory amounts to 1.2 eV for the carbene, 1.8 eV for the carbide dihydride, and 1.9 eV for the carbyne hydride. The dissociation therefore requires the absorption of multiple photons.

The theoretical atomic arrangements and vibrational characteristics were obtained using Born-Oppenheimer spin-density-functional theory molecular-dynamics(BO-SDFT-MD) calculations performed by R. Barnett and U. Landman[174]. In addition, IR spectra and reaction energetics were modeled by J. Lengyel with DFT calculations at the PBE/TZVP level of theory[175] with Grimme's D2 dispersion correction[176] as implemented in the Gaussian package[177]. In this work, the experimental measurements are compared to the results from the latter one due to excellent agreement between results obtained with both calculation approaches. Harmonic frequencies were scaled by the factor of 0.96 to correct for anharmonicities, and convoluted with a 20 cm^{-1} (47 cm^{-1} FWHM) Gaussian line-shape function to facilitate comparison to the experiment. More detailed description of the DFT computations along with the tables of vibrational frequencies of [4Ta,$^{12/13}$C,2$^{1/2}$H]$^+$ isomers can be found in the Supporting Information of the Ref. [171].
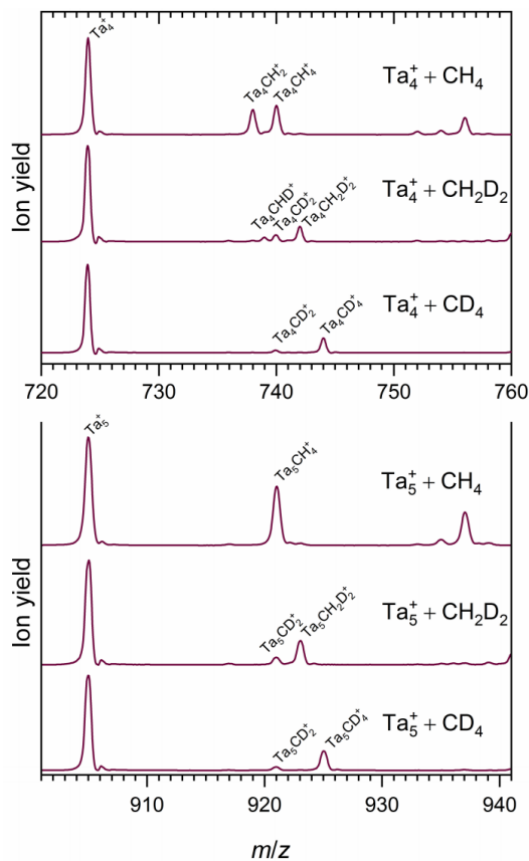
FIGURE 4.3: Mass spectra of the products of the reactions between Ta_4^+ (top three) and Ta_5^+ (bottom three) with different methane isotopologues. Similar results were obtained in the previous gas-phase investigation of these reactions[111]. The low intensities of $Ta_4CD_2^+$ in comparison with $Ta_4CH_2^+$ indicate large KIE associated with the reaction of methane dehydrogenation by Ta_4^+. Ta_5^+ only loosely binds methane in the process of cluster expansion into vacuum. Reprinted with permission from [171]

5 CO$_2$-activation by size-selected tantalum cluster cations (Ta$^+_{1-16}$)

The gradually increasing level of CO$_2$[25], the primary greenhouse gas, poses an unignorable threat of global warming[178]. Therefore, control and reduction of CO$_2$ emissions represent the most significant environmental challenge for the industry and energy production sector. One way to tackle this issue is to employ catalysts to convert carbon dioxide into industrially valuable products[179], which may also help mitigate the dependence on depleting fossil fuels.

In recent decades, numerous kinetic studies were performed to elucidate reaction patterns in the interactions between charged metal clusters with CO$_2$ in the gas phase[96, 97, 101, 103, 104, 109]. Tantalum compounds serve as ideal model systems for studying this reaction due to the element's unique reactivity originating from relativistic effects, which for example play an important role in Ta-C bond formations, or its oxophilicity, which represents a strong driving force in reactions with oxygen-containing species[73, 83]. Furthermore, tantalum was also found to be one of the few elements whose singly charged atom cations promote decarbonylation of CO$_2$ molecules[96]. In the course of this reaction, the tantalum cation is getting oxidized with the formation of TaO$^+$, and a neutral CO moiety is released into the gas phase. For bare tantalum clusters this oxidation may lead to additional complications, as the oxophilicity of the metal results in a highly exothermic oxide formation so that even under multi-collision conditions fragmentation may occur. Such a scenario is observed for small and intermediate tantalum cluster cations when being reacted with O$_2$[123, 124], and only for clusters with more than 12 atoms fragmentation by the ejection of TaO units is not observed any longer[180]. However, as CO$_2$ is a much weaker oxidant, it is questionable if such a pathway does occur at all in reactions with carbon dioxide.

In this chapter the reaction sequences of bare tantalum cluster cations Ta^+_n (n = 1-16) with CO$_2$ under multi collision conditions is present.

5.1   Results

As can be seen in the mass spectra in Fig. 5.1, the reaction of CO$_2$ (Westfalen, 5.0) with tantalum cluster cations follows two different pathways. The priority of either of them depends on the cluster size and on the number of CO$_2$ molecules that have already reacted with this cluster.
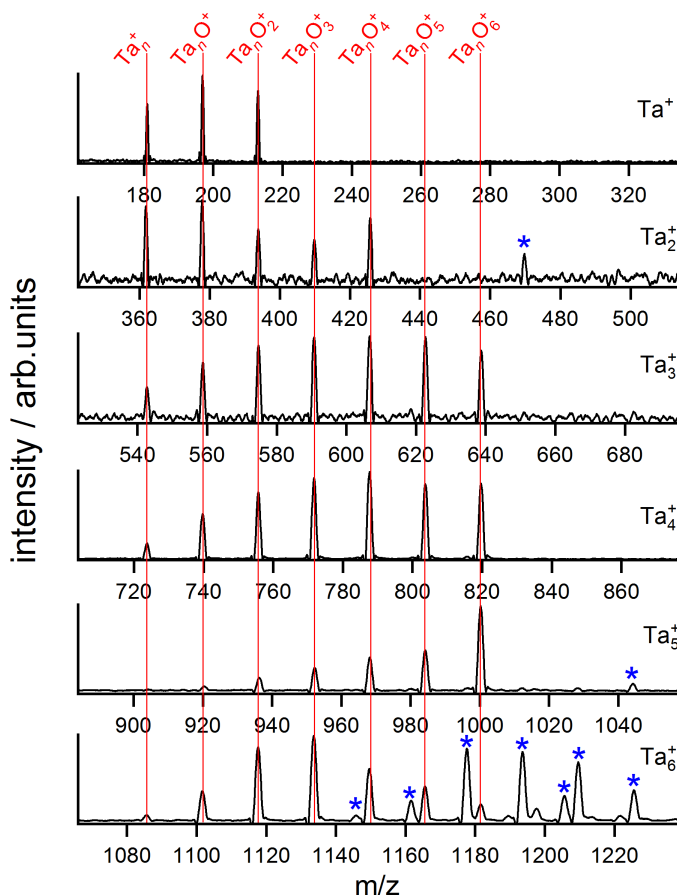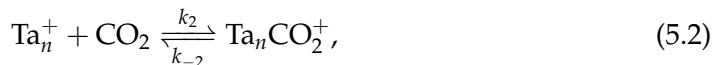

FIGURE 5.1: Mass spectra of size-selected Ta$_n^+$ (*n* = 1-6) and the corresponding products of their reaction with CO$_2$ after being stored in the ion trap for 29 ms. Peaks denoted by asterisks indicate products of molecular adsorption of CO$_2$. The total pressure in the trap amounts to 0.82 Pa, the proportion of carbon dioxide in the mixture is 10 ppm.

Already upon the association with the first CO$_2$, Ta$_n^+$ clusters facilitate both pathways depending on the number of atoms in the clusters: the first pathway represents a decarbonylation process, in which an oxygen atom transfer (OAT) from CO$_2$ to the metal species is accompanied by a loss of neutral CO, thus yielding a tantalum monoxide Ta$_n$O$^+$. The second reaction occurs via the adsorption of carbon dioxide and subsequent formation of products with elemental composition [Tan,C,2O]$^+$. Both reaction pathways can be expressed accordingly:

$$Ta_n^+ + CO_2 \xrightarrow{k_1} Ta_nO^+ + CO, \tag{5.1}$$

$$Ta_n^+ + CO_2 \underset{k_{-2}}{\overset{k_2}{\rightleftharpoons}} Ta_nCO_2^+, \tag{5.2}$$

where k_1, k_2, and k_{-2} denote the rate coefficients of the respective reaction. In a very good approximation, the decarbonylation reaction (Eq. 5.1) can be considered irreversible and, therefore, its back reaction can formally be omitted. This assumption is justified by the very low concentrations of CO in the trap, what originates from low reaction conversions due to the low amount of clusters in the trap and a constant replenishment of the reactant gas. In contrast to the OAT, it remains unclear for the second pathway, whether a C-O bond is cleaved or even weakened, because mass-spectrometric detection alone does not supply any structural information on the investigated compounds. However, as the observed reactions occur at room temperature and in a consecutive manner, they can be easily distinguished from a mere condensation/physisorption of CO_2. It seems thus much more likely that a chemisorption process occurs in these reactions. Different to an oxidation by dioxygen[123, 124], fragmentation of the metal clusters is not observed. Furthermore, formation of carbides (Ta_nC^+) or a release of one oxygen molecule (Ta_nCO^+) does not occur as well. The selectivity of the two reaction pathways can therefore be expressed with the corresponding branching ratios (BR), given for the OAT by:

$$BR_{OAT} = \frac{k_1}{k_1 + k_2}, \tag{5.3}$$

When evaluated as a function of cluster size, the BRs of the reaction with the first CO_2 molecule (Tab. 5.1) exhibit a particular trend (Fig. 5.2a). While species with less than six tantalum atom exclusively undergo OAT, larger clusters start to feature the incorporation of entire CO_2 molecules without a desorption of any neutral fragment. While this second reaction pathway is already observed for Ta_7^+, it only becomes the dominant reaction for Ta_8^+ and larger clusters. For the clusters of such sizes BRs toward OAT lie in the range of 0–30% (Fig 5.2a). The reaction behavior of Ta_7^+ marks the transition from one reaction regime into another and reflects properties of both small and larger clusters. On the one hand, this cluster preferably enables decarbonylation of CO_2 with a BR_{OAT} of 87±12%, sharing this characteristic with the reactions of smaller clusters. On the other hand, adsorption of CO_2 without desorption of a neutral already becomes a significant pathway that is dominant for larger sizes. When the reactivity of both pathways is evaluated, it becomes apparent that the decrease of the OAT rates (Fig. 5.2b) is compensated by the increase in the rates of CO_2 adsorption. This results in a modest but constant rise of the total reactivity, which is the sum of both reaction rates (or rate coefficients), with increasing cluster size (Fig. 5.2c). The origin of the particular reaction behavior most likely stems from an increase in the steric factor for larger clusters and further indicates

TABLE 5.1: Bimolecular rate coefficients $k^{(2)}$ in units of 10^{-8} cm^3 s^{-1} and branching ratios (see Eq. 5.3) of the first-step CO$_2$-decarbonylation and CO$_2$-adsorption reactions by bare Ta$_n^+$. For each cluster size an average value of two or more measurements is presented with error bars reflecting corresponding statistical uncertainties. Fractions of CO$_2$ in buffer gas vary between 10 and 25 ppm, the total pressure in the trap is 0.82 Pa.

n	$k_1^{(2)}$	$k_2^{(2)}$	$\mathbf{BR}_{OAT}$
1	1.1±0.1		100
2	1.6±0.2		100
3	2.7±0.1		100
4	3.3±0.3		100
5	3.7±0.4		100
6	5.4±1.3		100
7	5.2±3.3	0.8±0.7	87.4±12.1
8	1.4±0.9	3.5±2.5	29.1±19.8
9	0.5±0.4	5.9±3.1	8.4±7.5
10	0.6±0.4	7.3±2.7	7.8±5.5
11	0.1±0.1	5.5±1.7	1.7±1.7
12	2.6±1.1	4.9±1.5	34.6±11.4
13	2.2±0.1	5.5±1.6	28.4±6.1
14	0.7±0.5	6.8±2.9	9.0±6.6
15	1.5±1.5	7.6±1.2	16.3±13.8
16	1.1±1.1	7.1±1.8	13.1±11.8

that the course of the reaction features similar characteristics (*e.g.* similar reaction steps) even for different cluster sizes.

5.1.1   Reactivity of Ta$_{1-6}^+$-clusters

As shown in Fig. 5.1, small Ta$_n^+$ clusters with n = 1-6 can react with CO$_2$ with subsequent CO elimination. In this case, multiple decarbonylation steps, *i.e.*, tantalum oxidation, occur in a sequence of consecutive reactions, and the number of such steps is strongly size-dependent. While all these small clusters are characteristic to facilitate the decarbonylation as a first reaction step, only monomer, trimer, and tetramer exclusively form tantalum oxides in all the consecutive reaction steps. Dimer and pentamer strongly prefer decarbonylation, but a trace amount of intermediates corresponding to CO$_2$ adsorption are detected in the mass spectra as well. Ta$_6^+$ forms exclusively an oxide in the first reaction step, but features significant rates for both reaction pathway in every consecutive reaction step until the clusters are saturated with CO$_2$.

The atomic tantalum cation, Ta$^+$, was found to be selective toward the decarbonylation reaction and facilitates two consecutive reactions yielding TaO$_2^+$ and two CO molecules as products. The bimolecular rate coefficient of decarbonylation reactions is $1.1 \pm 0.1 \times 10^{-8}$ cm^3 s^{-1} for both the first and the second steps. The observed two-step reaction is in line with the previously reported Ta$^+$-mediated activation of
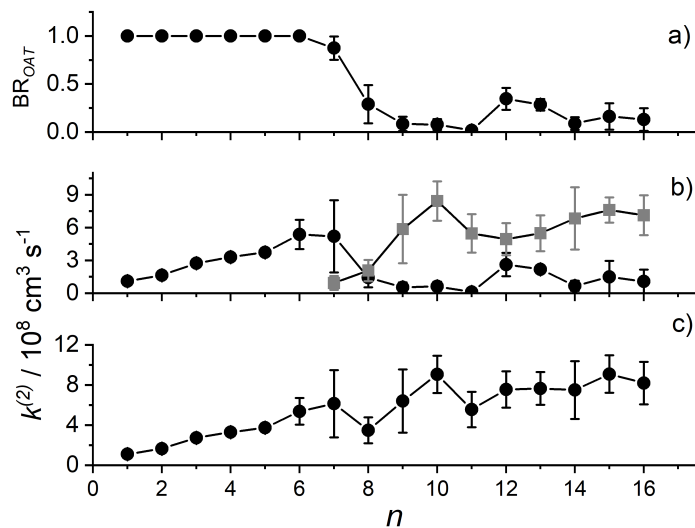
FIGURE 5.2: Selectivities and total reactivities of bare tantalum clusters Ta_n^+ (n = 1-16) in their reaction with the first CO_2 molecule. a) Branching ratios of the oxygen atom transfer (BR_{OAT}) for a reaction between the first CO_2 molecule and bare Ta_{1-16}^+ clusters; b) bimolecular rate coefficients ($k^{(2)}$) of the decarbonylation reaction (black) and the adsorption of CO_2 without fragmentation (gray); c) bimolecular rate coefficients of the total reactivity. For each cluster size an average value of two or more measurements is presented with error bars reflecting corresponding statistical uncertainties. All data represent values obtained at the total pressure of 0.82 Pa in the trap with the proportion of carbon dioxide in the mixture of 10 ppm.

CO_2 by the groups of Schwarz[85] and Bohme[96]. Their reaction rates are, however, an order of magnitude lower than those received in our experiment. This discrepancy can be explained by significantly different reaction conditions in all three experiments. It ought to be mentioned that this work focuses not on reporting the absolute rate coefficients but rather trends in relative reactivity, providing how cluster size affects the CO_2 activation. Ta_2^+ is more reactive than the monomer, with a rate coefficient of $1.6 \pm 0.2 \times 10^{-8}$ cm^3 s^{-1} for the first decarbonylation step, and offers four consecutive decarbonylations with gradually increasing reaction rates. For larger clusters in this series, *i.e.*, Ta_3^+–Ta_6^+, the number of successive decarbonylations typically increase with increasing cluster size, as shown in Fig. 5.1. Eq. 5.4 summarizes this sequential process, which yields tantalum oxides with maximum coverage of Ta_n^+ clusters with oxygen:

$$ Ta_n{}^+ \xrightarrow[-CO]{+CO_2} Ta_nO^+ \xrightarrow[-CO]{+CO_2} ... \xrightarrow[-CO]{+CO_2} Ta_nO_m{}^+ \tag{5.4} $$
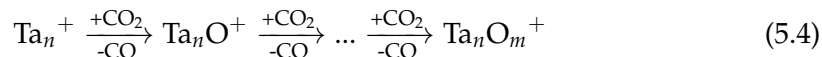
For example, the final oxidation product for the trimer and the tetramer is $Ta_{3,4}O_6^+$, for the pentamer is $Ta_5O_7^+$, and for the hexamer $Ta_6O_9^+$. The bimolecular reaction coefficients for the reactions of bare Ta_{1-6} with CO_2 are listed in Table 5.2.

An upward trend in the reaction rates associated with decarbonylation of CO_2 is also found for the first reaction step (Fig. 5.2b), indicating that larger clusters are more reactive than smaller ones likely due to a more efficient uptake of CO_2

molecules by larger tantalum clusters (as their geometrical cross-section increases as a function of the cluster size). This hypothesis is supported by comparing Figs. 5.2b and 5.2c, when the overall reactivity (decarbonylation and adsorption) is gradually increasing even for clusters with $n \geq 7$.

5.1.2   Reactivity of Ta$^+_{7-16}$-clusters

Ta$^+_7$ and larger clusters exhibit the adsorption of an entire carbon dioxide species in every reaction step. Consequently, the kinetic models (Fig. 5.7) become quite complex following the scheme displayed in Fig. 5.3. However, for all larger clusters CO$_2$ adsorption without fragmentation in general dominates over OAT. This trend is particularly pronounced at later reaction steps, in which usually only this pathway is observed.
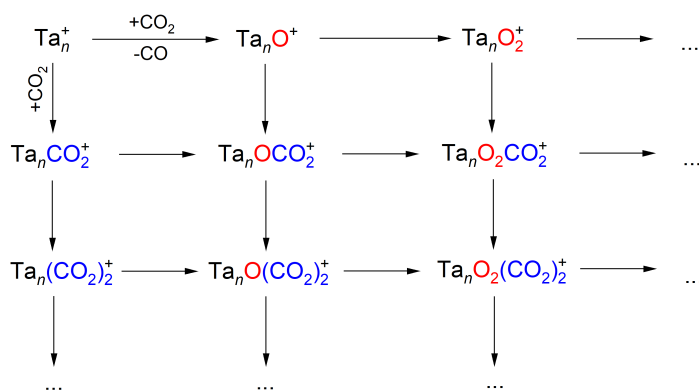
FIGURE 5.3: Reaction scheme for Ta^+_n-clusters with $n>6$ for several consecutive reactions with CO$_2$. In every reaction step, both reaction pathways are in principle enabled, but ultimately adsorption of CO$_2$ without any fragmentation prevails entirely over OAT.

The rates of decarbonylation change accordingly, as shown in Fig. 5.1b. While Ta$^+_7$ facilitates the reaction with the rate of $5.2 \pm 3.3 \times 10^{-8}$ cm^{3}s^{-1}, similar to Ta$^+_6$, the same reaction on Ta$^+_8$ is four times slower. Only trace amounts of Ta$_{11}$O$^+$ are observed in the mass-spectra, which may come unfiltered from the cluster source or be the result of interactions with residual water in the ion trap. However, Ta$^+_{12}$ and Ta$^+_{13}$ both reduce CO$_2$ with significant rates: $2.6 \pm 1.1 \times 10^{-8} cm^3 s^{-1}$ and $2.2 \pm 0.1 \times 10^{-8} cm^3 s^{-1}$ respectively. Moreover, Ta$^+_{12}$ can perform three, and Ta$^+_{13}$ — two consecutive OAT reactions. It ought to be mentioned that in the case of large Ta^+_n-clusters, the adsorption of CO$_2$ starts to be dominant. Therefore, the rate of the total reactivity of an initial cluster, $k^{(2)}_{tot.}$, has to be expressed as:

$$k^{(2)}_{tot.} = k^{(2)}_1 + k^{(2)}_2, \tag{5.5}$$

where $k^{(2)}_1$ and $k^{(2)}_2$ are the bimolecular rate coefficients for decarbonylation and intact adsorption, respectively. As shown in Fig. 5.1c, the rate coefficients measured

as a function of cluster size are gradually increasing with increasing size of Ta_n^+ clusters, even in the case when the reaction rates of decarbonylation significantly drops (Fig. 5.1b). Kinetic modelling reveals that compounds with compositions $Ta_{7-16}(CO_2)_{x>0}^+$ are not intermediates for $Ta_{7-16}O(CO_2)_{x-1}^+$. Therefore, these two types of species must be considered products of different reaction channels, which infers that species with formally intact adsorption of CO_2 represent stable products rather than quenched intermediates.

5.2 Discussion

The results of the reactions of bare Ta_n^+ (*n*=1-16) clusters exposed to carbon dioxide demonstrated strong dependence of the degree of Ta_n^+-oxidation and CO_2-adsorption rates on the number of Ta atoms in a reactant cluster. Geometric as well as electronic effects may be considered to affect the reactivity and will be discussed in the following in application to the current study. The total reactivity of small bare Ta_{1-6}^+ scales almost linearly with incrementing number of Ta atoms in a cluster (Fig. 5.2). The observed behaviour may be attributed to the increase in the sizes of clusters, which in turn may lead to the increase of the reaction cross-section. For larger clusters (Ta_{7-16}^+), the dependence of the total reactivity of a bare cluster on its size flattens, what is in line with the assumption that the steric factors of large spherical clusters (and consequently their collision rates) follow roughly $n^{1/3}$ dependence, where *n* is the number of atoms in a cluster. This is supported by the calculations performed by Fa *et al.* for Ta_N (*N*=2-23), predicting that all clusters in the investigated range have convex shapes with the exception of Ta_{15}, thus suggesting the increase of the cluster's size with each addition of one Ta-atom[181]. Apart from reaction rates and selectivity towards decarbonylation of CO_2, the reaction properties stay nearly the same and no pronounced size effects are observed.

Molecular configurations were investigated both experimentally and theoretically in previous publications for selected oxides of Ta-clusters. It was discovered, that oxygen atoms bind a metal core in a bridging manner[111, 182, 183], thus limiting the number of available sites of bonding. Therefore, based on the proposed geometries of Ta_n clusters[181], much higher oxidation states are expected in the final products of reactions of Ta_n^+ with CO_2, than it has been observed in the experiment. For example, Ta_4^+, which has a shape of a slightly Jahn-Teller-distorted tetrahedron[111, 181] with six edges, can indeed bring about six consecutive OATs in reactions with CO_2, but Ta_5^+, whose shape is calculated to be a heavily distorted trigonal bipyramid[111, 181], can only perform seven decarbonylation steps, with the the rate of the seventh step being largely suppressed in comparison to the sixth one. To explain this phenomenon, electronic effects must be regarded as well. Activation of a CO_2-molecule, which represents a closed-shell system, by atomic cations of transition metals is promoted by donation of electrons from d-orbitals into a π*-antibonding molecular orbital of CO_2, thus bending and loosening

the C=O bond, which may lead to its complete rupture and formation of a metal-oxygen bond stronger than that of CO-O. Therefore, the probability of an OAT from a CO$_2$ molecule to a metal cation depends on the availability of valence electrons on the metal centers. It can be thus inferred, that metal cores in Ta$_n^+$-oxides with specific oxidation states of Ta do not possess enough electronic density to promote activation of yet another molecule of carbon dioxide.

The oxidation of bare Ta clusters by CO$_2$ is in striking contrast with the results of the kinetic study on the reactivity of bare Ta$_n^+$-clusters towards O$_2$. In this study, typically much higher oxides were observed[123, 124, 180]. This can be directly explained with significantly different thermodynamic preconditions: carbon dioxide is almost 400 kJ/mol more stable than molecular oxygen. This can be attributed, again, to the closed-shell stabilization, thus making the activation of CO$_2$ energetically less efficient. Thermochemical effects are also reflected in the stability of metal clusters. Heat released in the reactions between small Ta$_n^+$ and O$_2$, destabilized the metal core facilitating the release of TaO neutral fragment; however, no degradation of metal clusters was observed in the reaction towards CO$_2$.

Electron density and structural features may cause the transition between almost exclusive O-atom transfer from a CO$_2$ molecule to smaller Ta$_n^+$ clusters (*n*=1-6) to the formation of CO$_2$-adducts on larger clusters. Assuming a less exothermic reaction and a progressing delocalization of d-orbitals hindering the activation of carbon dioxide, the intermediate cluster-CO$_2$ complex can be stabilized more efficiently, and the corresponding signal occurs in the mass-spectra for larger Ta$_n^+$ clusters. Similar effect was previously observed in the study of large Ta-cations (Ta$_{13-40}^+$) in their reactions with molecular oxygen[180].

5.3 Summary and Outlook

The gas-phase kinetic experiments reveal two regimes in the reactivity of bare cationic Ta$_n^+$ clusters (*n* = 1-16) towards carbon dioxide. In the first regime, Ta$_{1-6}^+$ perform exclusively decarbonylation reactions upon association with the first molecule of CO$_2$, *i.e.* an OAT from the CO$_2$ molecule to a metal cluster followed by the desorption of a neutral CO. The number of such consecutive OATs that a cluster can perform and corresponding reaction rates are size-dependent. Slow reactions of CO$_2$ adsorption not followed by the release of a neutral fragment were also observed for Ta$_2^+$, Ta$_5^+$, and Ta$_6^+$. In the second reaction regime, the dominant pathway for larger tantalum clusters (Ta$_{7-16}^+$) is the adsorption of CO$_2$, what is reflected in the branching ratios of OAT (Eq. 5.3) being lower than 50%. These clusters exhibit rather complex reaction patterns, where the products of CO$_2$ adsorption are also capable to perform OATs. Ta$_7^+$ represents the transition from one reaction regime into another and reflects properties of both small and larger clusters.

The abrupt change of reaction behaviour can be related to its thermodynamics.

Preliminary DFT calculations made by Johannes Margraf (FHI Berlin) using harmonic approximation already demonstrate a significant drop of the heat of the OAT reaction for Ta_8^+ in comparison to the smaller clusters (Fig. 5.4). Calculated heat capacities of Ta_n^+, $n = 2,4,6,8,10$ show that larger clusters heat significantly less because they have more vibrational modes to distribute the energy in. Taken together, these results support the idea that the CO desorbs from the small clusters because they heat up much more during the reaction. Such heat effects may play a crucial role in heterogeneous catalysis[184] too, and aspects such as the catalyst's heat capacity or the thermal coupling to the support may prove essential for the reaction outcome. Taking into account vibrational anharmonicities will bring more quantitatively accurate results for small clusters (*e.g.* Ta_2^+ and Ta_4^+).
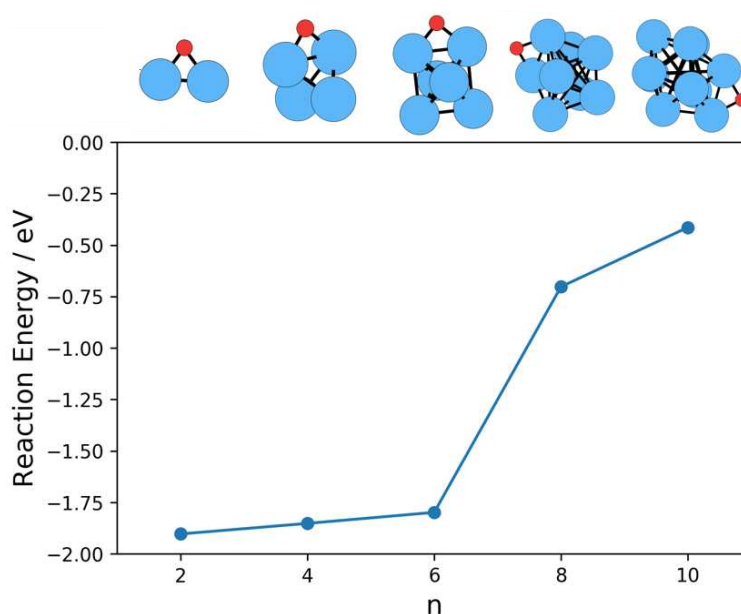
FIGURE 5.4: Reaction energy for $Ta_n^+ + CO_2 \longrightarrow Ta_nO^+ + CO$, $n = 2,4,6,8,10$. The reaction of OAT by Ta_8^+ is much less exothermic than the one performed by smaller clusters. Preliminary results, calculated by Johannes Margraf (FHI Berlin).
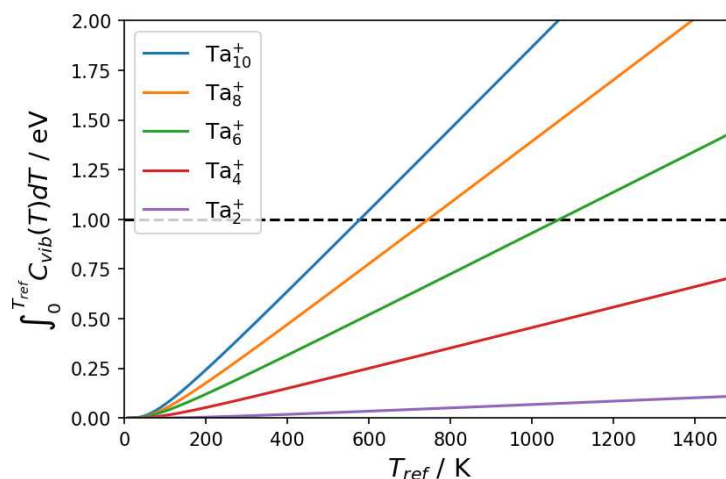
FIGURE 5.5: Integrated heat capacities of Ta^+_n, n = 2,4,6,8,10. The position at which a curve crossed the dashed line shows how much the corresponding cluster would heat up from 0K if one puts 1 eV of energy into its vibrational modes. Preliminary results, calculated by Johannes Margraf (FHI Berlin).

5.4   Supplementary Information

This section provides additional information on the reaction kinetics. Tables 5.3,5.2,5.4 list the reaction rates of CO$_2$-decarbonylation and adsorption reactions by bare and ligated Ta^+_n (n = 1-10). Figure 5.6 exhibits mass spectra of bare clusters Ta$^+_{1,2,4,5,6}$ and the products of their reaction with C^{18}O$_2$. The comparison with Fig. 5.1 confirms the correct assignment of the observed masses. Finally, figure 5.7 displays kinetic traces for the reactions of isolated bare Ta^+_n, n = 1-10 with CO$_2$.

For the DFT computations of Ta^+_n and Ta$_n$O$^+$, the ORCA package with the revPBE functional and def2-TZVP basis set was used[185–187]. Geometry optimization were carried out with tight convergence settings for both the self-consistent-field and optimizer. To verify that the optimized geometries are true minima on the potential energy surface, frequency calculations were carried out, and the absence of vibrational modes with imaginary frequencies was confirmed. Reported reaction energies include the zero-point vibrational energy contribution, but no thermal effects. Heat capacities were calculated within the harmonic approximation. Initial geometries of global minimum structures were taken from the work of Du and coworkers[188].

TABLE 5.2: Bimolecular rate coefficients $k^{(2)}$ in units of 10^{-8} cm^3 s^{-1} of consecutive CO$_2$-decarbonylation and adsorption reactions by Ta$_n^+$ (n = 1-6) and Ta$_6$OCO$_2^+$. For each reaction an average value of two or more measurements is presented with error bars reflecting corresponding statistical uncertainties. Fractions of CO$_2$ in the buffer gas vary between 10 and 25 ppm, the total pressure in the trap is 0.82 Pa.

products	Ta$^+$	Ta$_2^+$	Ta$_3^+$	Ta$_4^+$	Ta$_5^+$	Ta$_6^+$	Ta$_6$OCO$_2^+$
+O	1.1±0.1	1.6±0.2	2.7±0.1	3.3±0.3	3.7±0.4	5.4±1.3	2.2±0.1
+CO$_2$							
+O$_2$	1.1±0.1	1.9±0.3	3.2±0.03	3.2±0.3	4.0±0.3	4.5±1.0	3.7±0.6
+OCO$_2$						<0.1	2.8±0.8
+O$_3$		3.2±0.3	3.5±0.2	3.8±0.4	3.6±0.2	4.0±0.8	5.1±1.4
+O$_2$CO$_2$						0.5±0.2	0.4±0.3
+O$_4$		3.8±0.3	3.9±0.1	4.0±0.5	4.0±0.3	3.0±0.8	3.3±0.3
+O$_3$CO$_2$						2.4±0.8	0.5
+O$_5$			4.2±0.4	3.6±0.5	4.0±0.3	3.4±2.2	0.5±0.2
+O$_4$CO$_2$						3.6±1.5	
+O$_6$			3.3±0.6	3.2±0.5	3.8±0.5	3.8±2.1	
+O$_5$CO$_2$						1.4±1.0	
+O$_7$					0.08±0.05	4.1±0.7	
+O$_6$CO$_2$					<0.1		
+O$_8$						2.6±0.3	
+O$_7$CO$_2$							
+O$_9$						3.2±0.6	
+O$_8$CO$_2$							

TABLE 5.3: Bimolecular rate coefficients $k^{(2)}$ in units of 10^{-8} cm^3 s^{-1} of consecutive CO$_2$-decarbonylation and adsorption reactions by Ta$_n^+$ (n = 7-8). For each reaction an average value of two or more measurements is presented with error bars reflecting corresponding statistical uncertainties. Fractions of CO$_2$ in buffer gas vary between 10 and 25 ppm, the total pressure in the trap is 0.82 Pa.

products	Ta$_7^+$	Ta$_7$CO$_2^+$	Ta$_7$(CO$_2$)$_2^+$	Ta$_8^+$	Ta$_8$CO$_2^+$	Ta$_8$(CO$_2$)$_2^+$
+O	5.9±2.8	6.2±3.9	-	2.1±0.4	2.6±0.8	0.9±0.6
+CO$_2$	1.5±0.4	2.9±0.9		4.4±2.3	3.0±1.2	3.5±1.1
+O$_2$	4.4±1.6	-	-	2.2±0.3	2.3±1.4	2.2±0.6
+OCO$_2$	1.7±0.7	3.9±1.7	5.0±1.5	3.7±1.5	3.7±0.7	2.0±0.6
+O$_3$	1.7±0.5	1.3±0.9	0.8±0.2	-	3.3±2.1	1.8±0.7
+O$_2$CO$_2$	4.0±2.2	3.5±1.1	1.5±0.7	6.4±2.7	4.5±0.6	3.6±0.3
+O$_4$	-	2.9±1.8	0.6±0.4		-	1.9±0.3
+O$_3$CO$_2$	8.2±4.5	5.0±1.5	3.2±2.5		13.1±3.8	
+O$_5$		5.4±0.1	1.5±1.3			
+O$_4$CO$_2$		6.8±3.7	2.0±0.8			
+O$_6$		-				
+O$_5$CO$_2$		3.4±0.6				

TABLE 5.4: Bimolecular rate coefficients $k^{(2)}$ in units of 10^{-8} cm^3 s^{-1} of consecutive CO$_2$-decarbonylation and adsorption reactions by Ta$_n^+$ (n = 9-10). For each reaction an average value of two or more measurements is presented with error bars reflecting corresponding statistical uncertainties. Fractions of CO$_2$ in buffer gas vary between 10 and 25 ppm, the total pressure in the trap is 0.82 Pa.

products	Ta$_9^+$	Ta$_9$CO$_2^+$	Ta$_9$(CO$_2$)$_2^+$	Ta$_{10}^+$	Ta$_{10}$CO$_2^+$	Ta$_{10}$(CO$_2$)$_2^+$
+O	0.8±0.2	1.1±0.1	1.0±0.1	0.6±0.4	2.1±0.4	1.1±0.5
+CO$_2$	4.6±0.6	3.1±0.1	2.6±0.0	9.1±1.6	5.1±0.8	3.2±0.4
+O$_2$	-	1.7±0.5	0.5±0.4	-	-	3.0±1.4
+OCO$_2$	5.2±1.7	3.8±0.7	2.7±0.1	9.7±3.1	11.5±1.8	3.1±1.2
+O$_3$		-	-			-
+O$_2$CO$_2$		9.0±4.1	4.5±0.2			10.3±5.1

FIGURE 5.6: Mass spectra of size-selected Ta$_n^+$ (n = 1,2,4,5,6) and the corresponding products of their reaction with C^{18}O$_2$ at different ion-trap storage times. Peaks denoted by asterisks indicate products of molecular adsorption of C^{18}O$_2$. The total pressure in the trap amounts to 0.82 Pa, the proportion of carbon dioxide in the mixture is 20 ppm.
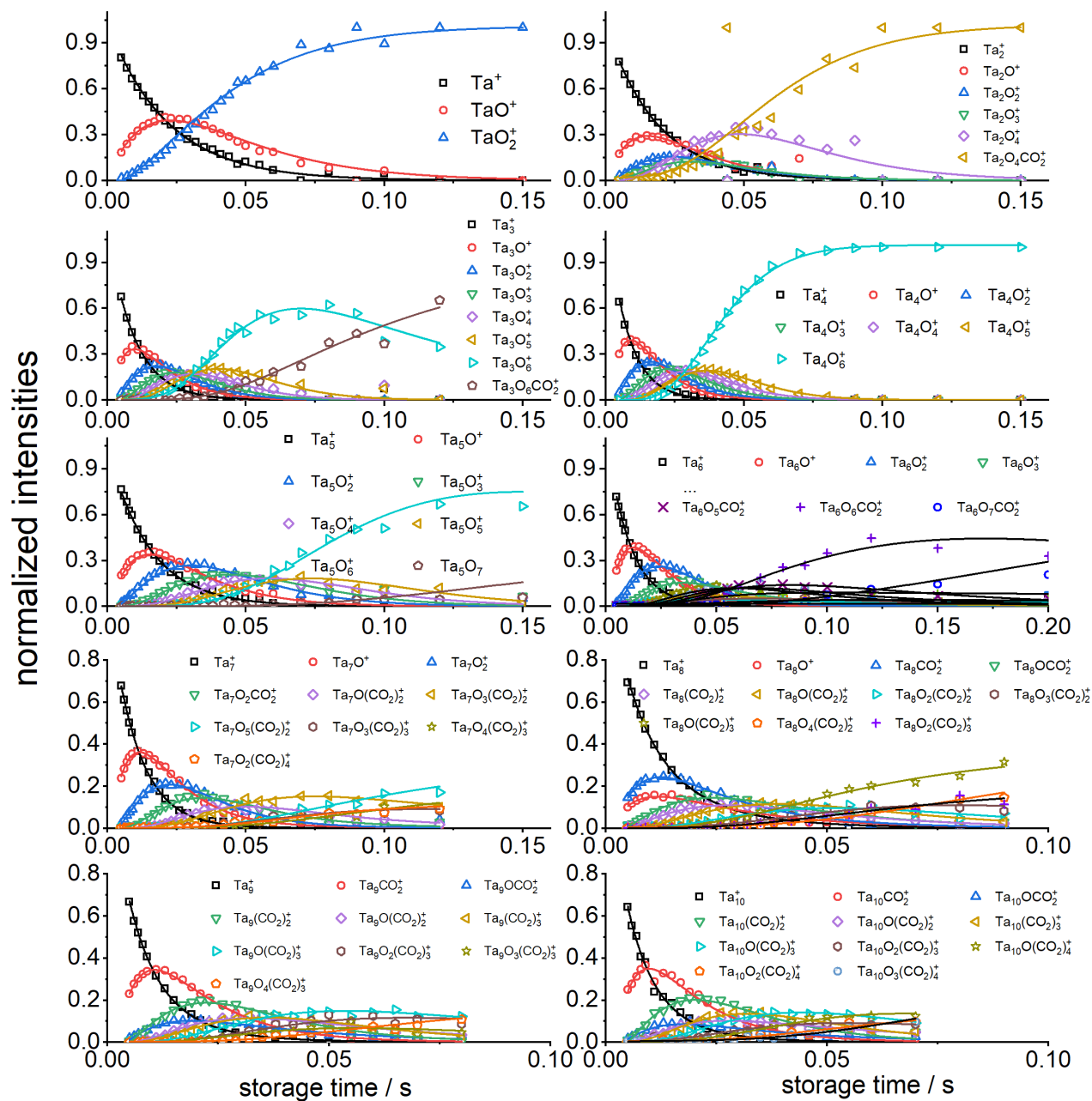
FIGURE 5.7: Kinetic modelling of the reactions between Ta_{1-10}^+ and CO_2. For the reactions of Ta_{6-10}^+, only the most abundant species are displayed. The total pressure in the trap amounts to 0.82 Pa, the proportion of carbon dioxide in the mixture is 10 ppm.

6 Direct Coupling of Methane and Carbon Dioxide on $Ta_{1,4}^+$

Despite the high value of products of methane and carbon dioxide valorisation, the efficient use of both molecules together is still not feasible commercially. Until now, only dry reforming of CH_4 and CO_2 (Eq. 1.10)has been applied on the industrial scale to produce syngas (CO + H_2)[189] in an energetically highly demanding process. Catalytic coupling of CH_4 and CO_2 under mild conditions is a very attractive route, which, however, requires a catalyst that can activate both molecules and bring about coupling thereof (C-C or C-O bond formation). Although there are a few reports on the heterogeneous catalysis of such processes[190–194], they usually exhibit relatively poor selectivity and low yields of the desired products like acetic acid, which makes them commercially not competitive.

Gas-phase investigations can provide mechanistic insights into chemical processes occurring in the activation of methane and carbon dioxide. While there are quite some studies focused on either of these two reactions, the number of papers addressing the direct coupling of CO_2 and CH_4 is limited to studies of atomic Ta^+[85], bimetallic CuB^+[106], and anionic $RhVO_3^-$ [107]. Tantalum is a prospective catalyst, as this element has been demonstrated to enable various coupling reactions, such as non-oxidative coupling of methane (see Chapter 3), methane oxidation[86], and potentially ammonia synthesis[195].

In this chapter, the reactions of Ta^+ and Ta_4^+ towards activation of methane and CO_2 are scrutinised in both gas-phase kinetic experiments and DFT calculations.

6.1 Results

6.1.1 Reactions between isolated $Ta_{1,4}CH_2^+$ and CO_2 in the gas phase

The focus of the first experiment is on the reaction of the size-selected $TaCH_2^+$ with carbon dioxide, *i.e.*, the system with already activated methane. Several studies reported that the dissociative adsorption of methane on the metal is the first step in the CH_4/CO_2 coupling[190, 196, 197]. Activation of methane prior to the reaction with CO_2 significantly simplifies the reaction scheme by eliminating the collisions of reaction intermediates with additional methane molecules. The mass spectra, shown in Figure 6.1, reveal a total of six different species in the reaction sequence, namely

FIGURE 6.1: Mass spectra taken at different reaction times (A) and kinetic analysis (B) of room-temperature reactions of mass-selected $TaCH_2^+$ ions with CO_2. The experimental data points correspond to the normalized intensities of the reactants, intermediates, and products marked as follows: ■ $TaCH_2^+$, ● TaO^+, ▲ $Ta(O)CH_2^+$, ▼ TaO_2^+, ◆ $Ta(O)CH_2CO_2^+$, ◄ $Ta(O)CH_2(CO_2)_2^+$. Panel (C) represents the underlying mechanism suggested by the kinetic fit. The total pressure in the trap amounts to 0.82 Pa, the proportion of carbon dioxide in the mixture is 100 ppm

$TaO_{1,2}^+$, $Ta(O)CH_2^+$, and $Ta(O)CH_2(CO_2)_{1,2}^+$. The underlying reaction mechanism analyzed by a pseudo-first order kinetic fit confirms that the process starts with two competing parallel reactions. While $Ta(O)CH_2^+$ is formed through the CO_2 deoxygenation on the carbene, the presence of TaO^+ indicates that $Ta(O)CH_2^+$ can also undergo C–C coupling with CO_2 by the loss of a C_2H_2O unit. Both intermediates can, however, react further with CO_2: $Ta(O)CH_2^+$ is converted either to the adsorption products $Ta(O)CH_2(CO_2)_{1,2}^+$ or to TaO_2^+, which likely again results from C–C coupling with concomitant elimination of a C_2H_2O moiety. Overall, the primary gaseous reaction products are CO formed in a deoxygenation and the ketene C_2H_2O (ethenone). The formation of ketene is energetically favored over other possible stereoisomers such as ethynol or an oxirene[85]. It should be stressed that the observation of the two-step coupling, *i.e.*, deoxygenation (Eq. 6.1) followed by C-C coupling (Eq. 6.2), is in agreement with the earlier measurement of Wesendrup and Schwarz[85].

$$TaCH_2^+ + CO_2 \longrightarrow TaOCH_2^+ + CO \tag{6.1}$$

$$TaOCH_2^+ + CO_2 \longrightarrow TaO_2^+ + H_2C_2O \tag{6.2}$$
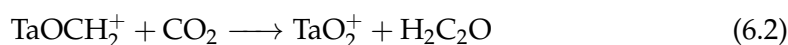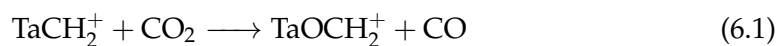
Similar to the trend noticed in the discussion of the reactivity of the bare Ta^+ towards CO_2 (Chapter 5), the rates reported by Wesendrup and Schwarz are an order of magnitude lower than those received in our experiment (Table 6.1), what can be ascribed to the significantly different reaction conditions. In addition to these two

TABLE 6.1: Bimolecular rate coefficients $k^{(2)}$ in units of $10^{-9}\,\mathrm{cm^3\,s^{-1}}$ of the reactions between isolated $TaCH_2^+$ and CO_2. For each reaction an average value of two or more measurements is presented with error bars reflecting corresponding statistical uncertainties. Fractions of CO_2 in the buffer gas vary between 25 and 200 ppm, the total pressure in the trap is 0.82 Pa.

reactions	$k^{(2)}$
$TaCH_2^+ + CO_2 \longrightarrow TaO^+ + H_2C_2O$	1.8±1.1
$TaCH_2^+ + CO_2 \longrightarrow TaOCH_2^+ + CO$	9.0±2.4
$TaO^+ + CO_2 \longrightarrow TaO_2^+ + CO$	7.1±4.6
$TaOCH_2^+ + CO_2 \longrightarrow TaO_2^+ + H_2C_2O$	4.2±2.4
$TaOCH_2^+ + CO_2 \longrightarrow TaOCH_2CO_2^+$	9.2±4.9
$TaOCH_2CO_2^+ + CO_2 \longrightarrow TaOCH_2(CO_2)_2^+$	8.6±2.8

reactions, the kinetic fit identifies a new coupling reaction, which occurs directly from $TaCH_2^+$ as a single-step process without the necessity to generate $Ta(O)CH_2^+$. A more detailed kinetic analysis reveals that CO_2 deoxygenation as the first step is preferred over C–C coupling with a branching ratio of 82%:18%. Yet, as the subsequent C–C coupling on $Ta(O)CH_2^+$ is suppressed by a factor of 2.3 in comparison to the CO_2 adsorption (30%:70%), the contribution of both pathways yields approximately 43%. In the reactions of the size-selected $Ta_4CH_2^+$ with CO_2, seven species are detected in the mass spectra, shown in Figure 6.2. Within the first 9 ms, the mass spectrum is dominated by the reactant, as well as a less intense signal associated with Ta_4CO^+ and traces of Ta_4C^+, $Ta_4CO_2^+$, and $Ta_4C(CO_2)^+$. As the reaction progresses, further oxygenated species, $Ta_4CO_{2-7}^+$, appear along with trace amounts of the CO_2 adsorption product, $Ta_4CO_{1-7}(CO_2)^+$. According to the kinetic models, $Ta_4CH_2^+$ exclusively dissociates either into a formaldehyde-like (H_2CO) species or syngas ($H_2 + CO$). After that, further carbon dioxide molecules are either adsorbed or deoxygenated.

6.1.2 Quantum-Chemical Investigations of the Coupling Reactions

It appears in the above results, that there is a fundamental difference between tantalum clusters' ability to mediate CH_4 and CO_2 coupling: monomers promote C–C coupling, whereas tetramers lead to C–O coupling. The atomic tantalum ion pathway has been examined extensively in the literature[85, 105]. However, as described above, a single step coupling was identified in this experiment, and therefore the respective quantum chemical exploration has not been discussed in the previous work. To this end, density functional theory (calculations were performed by Konstantin
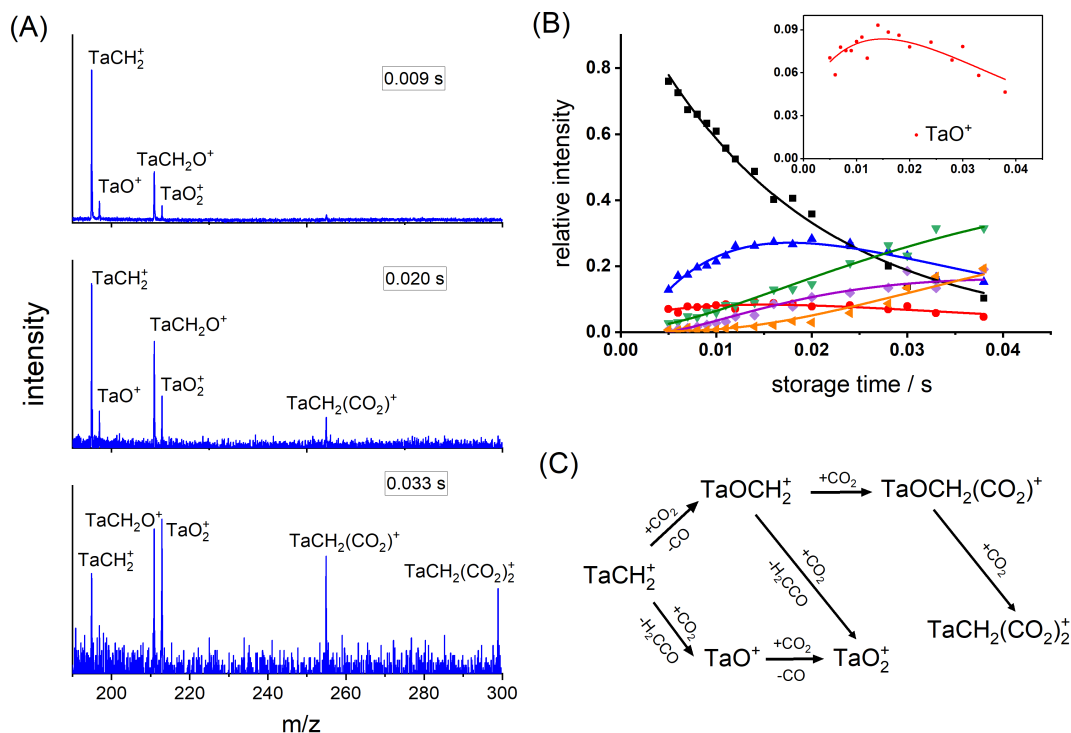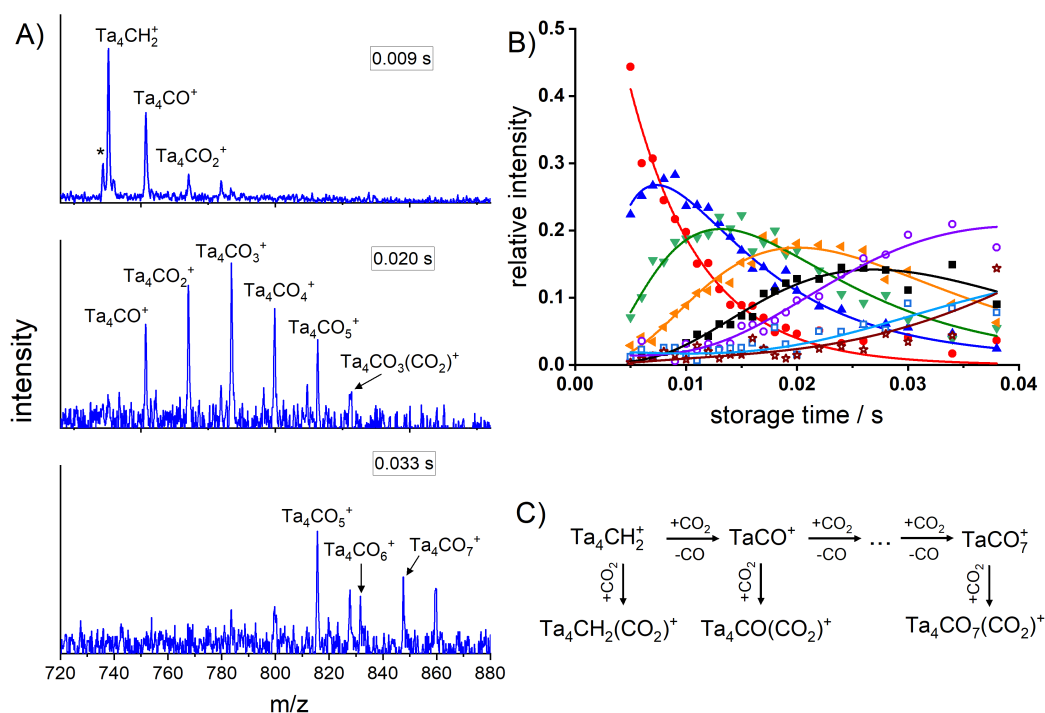
FIGURE 6.2: Mass spectra taken at different reaction times (A) and kinetic analysis (B) of the room-temperature reaction of mass-selected $Ta_4CH_2^+$ ions with CO_2. The experimental data points correspond to the normalized intensities of the reactants, intermediates, and products marked as follows: ● $Ta_4CH_2^+$, ▲ Ta_4CO^+, ▼ $Ta_4CO_2^+$, ◄ $Ta_4CO_3^+$, ■ $Ta_4CO_4^+$, ○ $Ta_4CO_5^+$, □ $Ta_4CO_6^+$, ★ $Ta_4CO_7^+$. The peak denoted by an asterisk indicates Ta_4C^+ generated in the cluster source and not filtered out in the QMF due to the small mass difference between Ta_4C^+ and $Ta_4CH_2^+$. For the sake of clarity, the products of physisorption are not displayed. Panel (C) represents the underlying mechanism suggested by the kinetic fit. The total pressure in the trap amounts to 0.82 Pa, the proportion of carbon dioxide in the mixture is 100 ppm

Jakob, TU Munich) is applied to calculate ground state energies and other thermo-chemical properties of the suggested mechanism. The main focus is, therefore, set on the two different channels leading to the same reaction outcome, TaO_2^+:

$$TaCH_2^+ + 2\,CO_2 \longrightarrow TaO_2^+ + CO + C_2H_2O \qquad (6.3)$$

$$TaCH_2^+ + CO_2 \longrightarrow Ta(O)CH_2^+ + CO \qquad (Ia)$$

$$Ta(O)CH_2^+ + CO_2 \longrightarrow TaO_2^+ + C_2H_2O \qquad (Ib)$$

$$TaCH_2^+ + CO_2 \longrightarrow TaO^+ + C_2H_2O \qquad (IIa)$$

$$TaO^+ + CO_2 \longrightarrow TaO_2^+ + CO \qquad (IIb)$$

TABLE 6.2: Bimolecular rate coefficients $k^{(2)}$ in units of 10^{-9} cm^3 s^{-1} of the reactions between isolated $Ta_4CH_2^+$ and CO_2. For each reaction an average value of two or more measurements is presented with error bars reflecting corresponding statistical uncertainties. Fractions of CO_2 in the buffer gas vary between 25 and 200 ppm, the total pressure in the trap is 0.82 Pa.

reactions	$k^{(2)}$
$Ta_4CH_2^+ + CO_2 \longrightarrow Ta_4CO^+ + H_2CO$	13.1±2.6
$Ta_4CO^+ + CO_2 \longrightarrow Ta_4CO_2^+ + CO$	13.4±2.7
$Ta_4CO_2^+ + CO_2 \longrightarrow Ta_4CO_3^+ + CO$	11.9±2.1
$Ta_4CO_3^+ + CO_2 \longrightarrow Ta_4CO_4^+ + CO$	9.3±2.3
$Ta_4CO_4^+ + CO_2 \longrightarrow Ta_4CO_5^+ + CO$	10.3±3.0
$Ta_4CO_5^+ + CO_2 \longrightarrow Ta_4CO_6^+ + CO$	3.6±1.4
$Ta_4CO_6^+ + CO_2 \longrightarrow Ta_4CO_7^+ + CO$	4.7±2.2
$Ta_4CO^+ + CO_2 \longrightarrow Ta_4CO(CO_2)^+$	2.9±2.3
$Ta_4CO_2^+ + CO_2 \longrightarrow Ta_4CO(CO_2)^+$	1.6±0.8
$Ta_4CO_3^+ + CO_2 \longrightarrow Ta_4CO(CO_2)^+$	0.7±0.5
$Ta_4CO_4^+ + CO_2 \longrightarrow Ta_4CO(CO_2)^+$	<0.1
$Ta_4CO_5^+ + CO_2 \longrightarrow Ta_4CO(CO_2)^+$	2.9±1.6

An investigation of initial and final state reveals (Fig. 6.3) that the overall reaction is exergonic in the singlet case with a reaction energy of ΔE_r = -1.13 eV (ΔG_r° = -1.18 eV) and endergonic in the triplet with ΔE_r = 0.95 eV (ΔG_r° = 0.88 eV). Other multiplicities are not considered in the following investigation as they are energetically unfavorable. This striking difference arises as the triplet state is favored in case of the carbene (by 0.56 eV) while TaO_2^+ strongly favors a singlet configuration (by 1.52 eV). Interestingly, the situation is inverted in case of the reaction intermediates where the carbene $Ta(O)CH_2^+$ prefers the singlet (0.33 eV) and the tantalum monoxide, TaO^+, prefers the triplet state (1.02 eV). Therefore, spin-crossing effects must be considered to play a role in this process[78].

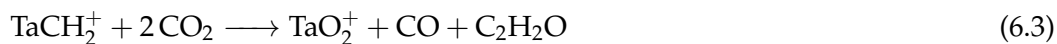Focusing on the first reaction channel (Eq. Ia,Ib), one finds that the formation of the reaction intermediate is energetically downhill in case of both multiplicities, even though the reaction is more favored for singlet states, as shown in Figure 6.3A. These observations are in good agreement with the earlier calculations by Sändig and Koch[105]. However, the conversion of the intermediates into the final product is endergonic for both spin multiplicities. At the same time, the physisorption of carbon dioxide is exergonic with an adsorption energy of 1.1–1.4 eV, meaning that the adsorption of CO_2 is energetically preferential in this case. The second reaction channel (Figure 6.3B) is significantly different. While an exergonic reaction is found in the triplet case, the formation of TaO^+ and H_2C_2O is actually slightly endergonic by about 0.01 eV, showing that path II (Eq. IIa,IIb) is less favorable than path I (Eq. Ia,Ib). However, due to a strong chemisorption of the evolving ketene, the reaction is likely to occur regardless of the overall reaction energy. In this case, the $TaCH_2^+$ acts like typical nucleophilic carbene, which explains its tendency to allow direct C-C coupling with carbon dioxide, as the carbon atom in CO_2 is positively

polarized. The following product formation, TaO_2^+, is then significantly exergonic for singlet states, in contrast to reaction path I, and strongly exergonic for triplet states. Hence, the triplet state of TaO^+ can be considered as a trap state, as its formation is energetically favorable while consequent reactions are energetically unlikely. Overall, the thermochemical calculations are in line with the experimental reaction rates. The calculations correctly predict that CO_2 deoxygenation leading to formation of $Ta(O)CH_2^+$ is favored over the one step coupling. Additionally, further kinetic reasons might support this conclusion as deoxygenation will likely proceed via a less complex transition state compared to the direct coupling (triangular instead of square transition state). Secondly, the reaction intermediate $Ta(O)CH_2^+$ energetically prefers CO_2 adsorption over C-C coupling, in agreement with the branching ratio of 30:70. However, as the calculations might predict this branching too much in favor of CO_2 adsorption, it is important to mention that this adsorption process might also be a crucial part of the coupling reaction, enabling the formation of the transition state.

While for atomic tantalum ions the spin state plays a fairly significant role, it is known that cationic tantalum tetramers prefer to be in a doublet state[111]. Since the higher number of atoms leads to an increase in structural complexity, several stereoisomers of the involved species must be considered. In the previous study which was described in detail in Chapter 4 and in Ref. [171], structure and energetics of the possible initial stereoisomers have already been discussed. It was found that a carbyne hydride (HTa_4CH^+) and carbide dihydride ($H_2Ta_4C^+$) isomers are favored over the carbene one. On the tantalum tetramers, the single charge can distribute somewhat evenly on the four different atoms[111], which consequently leads to a decrease in partial charge. This destabilizes the carbene compared to the other stereoisomers, as the tantalum sites are less electrophilic. In this work, the carbyne hydride is found to be 0.07 eV below the carbide dihydride (Fig. 6.3C), in line with the previous study[171] given the accuracy of the different computational methods. The investigation of the final state also shows possible formation of two different stereoisomers of $[Ta_4CO]^+$: a carbide oxide (OTa_4C^+) and a carbonyl (Ta_4CO^+). Structural optimization, however, reveal a striking energy difference of almost 2.0 eV, strongly favoring OTa_4C^+. Hence, from a thermodynamic point of view the formation of a carbide oxide during the reaction is preferred. However, it is likely that kinetic phenomena dominate the reaction outcome as the formation of a carbide oxide might need the cleavage of two C=O bonds, while formation of a carbonyl might only require one to be broken. In the latter case, one has also to consider a structure of the dissociated CH_2O species, which can be either a formaldehyde molecule (H_2CO) or a mixture of CO and H_2 (also known as a syngas) products. Note that H_2CO is favored energetically over the formation of syngas by 0.07 eV[10]. This difference is relatively small compared to the large difference between the tantalum stereoisomers. However, a strong chemisorption of formaldehyde on both tantalum

species indicates that formaldehyde is likely to form. Further, the quantum chemical calculations also show that hydrogen evolution would be connected to a reaction barrier of at least 0.39 eV and is hence unlikely. In any case, the formation of syngas molecules is also a plausible option as recently reported for rhodium–titanium oxide anions[198]. As a result, the CH_2O species might be either a formaldehyde molecule, CO/H_2, or a mixture thereof.

$$Ta_4CH_2^+ + CO_2 \longrightarrow Ta_4CO^+ + H_2CO \tag{6.4}$$

6.1.3 Reactions between isolated $Ta_{1,4}^+$ and CO_2 in the gas phase

Finally, the capability of small bare clusters to mediate the coupling of methane and carbon dioxide is addressed experimentally by probing the respective reaction mediated by bare metal cluster ions. The bare cluster cations are generated in a laser vaporization source, mass-selected (*i.e.*, Ta^+ and Ta_4^+) and stored for a reactivity experiment in the ion trap reactor, in which a mixture of methane and carbon dioxide were introduced. The results of the kinetic analysis are presented in Figure 6.4 and Table 6.3. Scheme 6.3A illustrates the underlying mechanism for the reaction of mass-selected Ta^+ cations with methane and carbon dioxide at 300 K under multicollisional conditions. It is obvious that Ta^+ can react first either with CH_4 or with CO_2. Despite the complex reaction scheme, four types of reactions were identified using reaction kinetics, namely CH_4/CO_2 coupling, CO_2 deoxygenation, CH_4 dehydrogenation, and adsorption of CO_2 or CH_4. The experiment showed that both coupling reactions occurred: one *via* the $Ta(O)CH_2^+$ intermediate and the other through direct conversion. While the latter reaction produces TaO^+, CO_2 oxygenation by Ta^+ is another reaction channel contributing to TaO^+ moiety. As shown by kinetic modeling, the dominant process is coupling with a rate of $2.0 \pm 0.7 \times 10^{-8}$ cm^3 s^{-1} compared to decarbonylation 3.3 times slower. It should be noted, however, that the kinetics does not fit experimental data without accounting for coupling reactions. In parallel, a four step consecutive dehydrogenation of methane molecules is observed, which is consistent with previous experiments on the reaction of tantalum cations with methane[112]. Almost all intermediates are involved in CO_2 deoxygenation, which is consistent with a recent report on CO_2 activation (see Chapter 5).

Both methane and CO_2 react in parallel with Ta_4^+. This reaction scheme appears to be even more complex than the Ta^+ chemistry, since the tantalum tetramer offers more oxidation steps than its monomeric analogue (see Chapter 5). Furthermore, it also offers different reactions like those involving intact adsorption. However, despite the complex reaction scheme, $Ta_4CH_2^+ + CO_2$ chemistry can still be identified, just as can the ion chemistry reactions between bare clusters and either methane or CO_2 can be observed (see Figure 6.5 and Table 6.4).
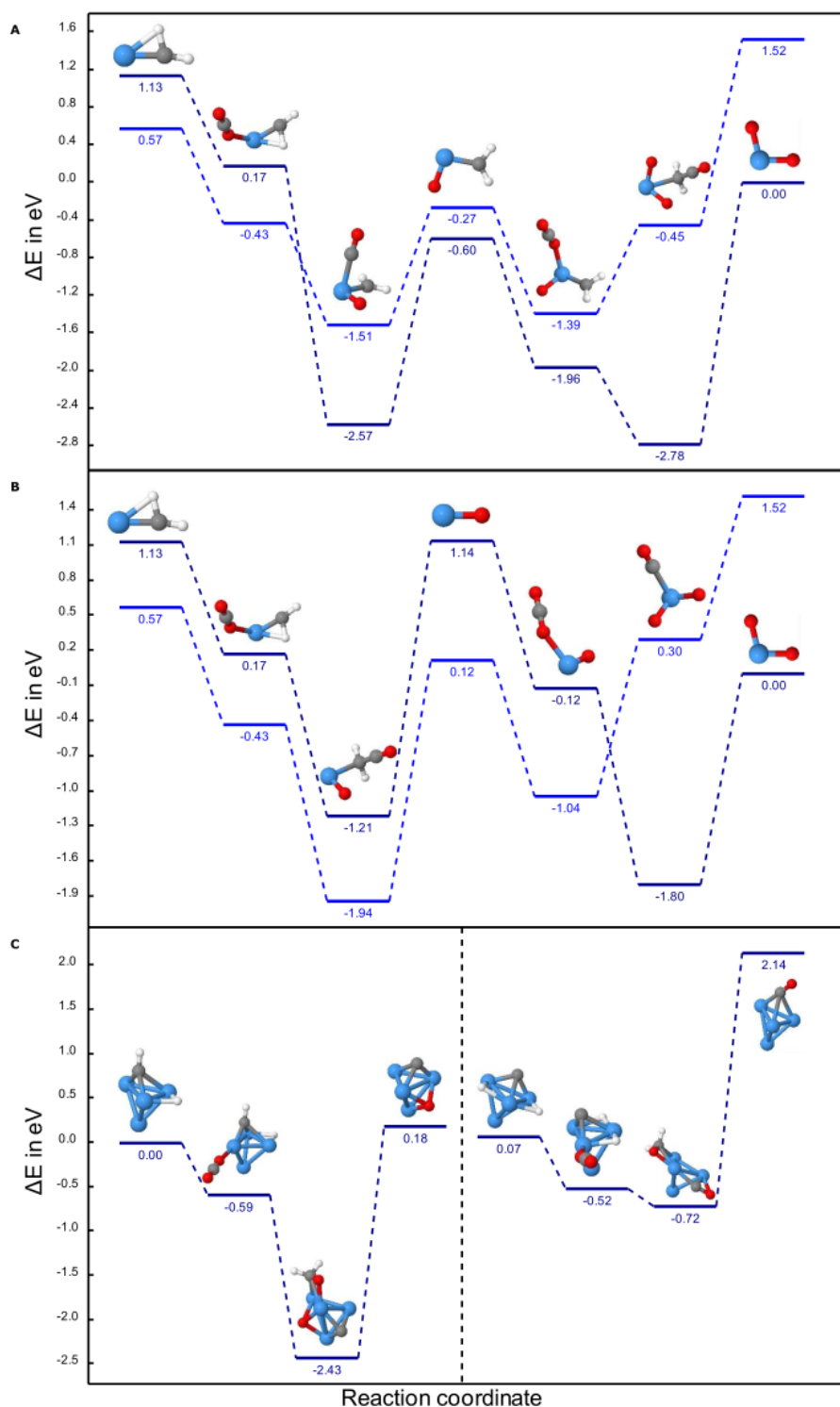
FIGURE 6.3: Zero-point corrected energies of all considered initial and final states as well as reaction intermediates for different reaction channel. Panel A and Panel B illustrate the coupling reactions mediated by single tantalum ions, $TaCH_2^+ + CO_2$, Panel A the reaction channel (I), Panel B the reaction channel (II). In both cases, singlet multiplicity is shown in dark blue, while triplet multiplicity is shown in light blue. Panel C illustrates pathways for tetrameric tantalum ions, $Ta_4CH_2^+ + CO_2$, with carbyne hydride on the left and carbide dihydride on the right. Note that all values are derived from the lowest energy initial/final states - TaO_2^+ for an atomic tantalum and HTa_4CH^+ for a tetrameric tantalum. Calculated by Konstantin Jakob (TU Munich).

6.2 Summary

The reaction of C-C coupling was previously observed in the $Ta^+/CH_4/CO_2$ system under single-collision conditions[85]. The proposed mechanism includes three steps: in the first one, Ta^+ performs a dehydrogenation reaction, the as-formed $TaCH_2^+$ further reacts with a molecule of CO_2 to form a $TaOCH_2^+$ intermediate, which in turn enables the coupling with another CO_2 molecule followed by the dissociation of a neutral H_2C_2O. In the experiment described in this chapter, the alternative pathway was observed, that suggests direct coupling of isolated $TaCH_2^+$ with CO_2. As revealed by DFT calculations, this pathway features significant barriers, which is reflected in its relatively low branching ratios.

Coupling of methane and carbon dioxide molecules was also observed and described for their reaction with Ta_4^+. In this system, a bare cluster first performs a methane dehydrogenation to form $Ta_4CH_2^+$, which then reacts with CO_2 to form a C-O bond and release a neutral [2H,C,O]. DFT analysis demonstrates that the $Ta_4CH_2^+$ ion that takes part in the coupling reaction most likely features the carbyne hydride structure (HTa_4C^+). While its reaction with CO_2 is slightly endothermic, the reaction of carbide dihydride, which was previously found to be the most dominant isomer of $[4Ta,C,2H]^+$ (see Chapter 4), is endothermic by over 2 eV.

These findings yet again demonstrated the high potential of Ta clusters to become useful catalysts in the future. Even though their chemistry is highly unselective in the systems described in this chapter, tantalum atoms and clusters can be used in more complex environments to tune the reactivity of a catalyst.

6.3   Supplementary Information

This section provides additional information about the reaction kinetics and details of the DFT calculations. Tables 6.3,6.4 list the reaction rates of different reactions of bare Ta$^+$ and Ta$^+$ and their intermediates with CO$_2$ and methane. Figures 6.4 and 6.5 demonstrate kinetic traces for the reactions of isolated bare Ta$_{1,4}^+$ with CO$_2$ and CH$_4$, and Figure 6.6 shows the corresponding mass spectra and reaction mechanisms.

The DFT calculations were realized by Konstantin Jakob (Technical University of Munich, Chair of Physical Chemistry). Electronic structure calculations were performed using the Gaussian 09 software package (Release B.01)[199]. In the rest of the work, the HSE06 hybrid level functional was used in combination with the triple-zeta Karlsruhe basis set def2TZVP for DFT calculations[187, 200, 201]. This combination has proven most accurate in the description of binding energies in metal organic TaH and TaCH$_x$ clusters in comparison to experiment. In order to calculate thermochemical properties of reactants and products as well as reaction intermediates, an initial geometry is either taken directly from the literature or prepared based on the geometries of similar reaction species. This geometry is then re-optimized for the given method and used for calculations of electronic energies, forces and force constants. Transition states are identified using a Synchronous Transit Quasi-Newton algorithm provided by Gaussian 09 (keyword: QST2), *i.e.* the combination of the quadratic synchronous transit and a Newton-Raphson optimization step that converges the system to the transition state. The two required input geometries are taken from the results of prior thermochemistry calculations.

TABLE 6.3: Bimolecular rate coefficients $k^{(2)}$ in units of 10^{-9} cm^3 s^{-1} of the reactions between isolated Ta$^+$ and a mixture of CH$_4$ and CO$_2$. For each reaction an average value of two or more measurements is presented with error bars reflecting corresponding statistical uncertainties. Fractions of CO$_2$ in the buffer gas vary between 35 and 100 ppm, fractions of methane vary between 50 and 300 ppm, relative ratios [CH$_4$]:[CO$_2$] are equal to either 1, 4.3, 5, 6.7, or 8.6. The total pressure in the trap is 0.82 Pa.

reactions	$k^{(2)}$
Ta$^+$ + CH$_4$ $\longrightarrow$ TaCH$_2^+$ + H$_2$	1.5±0.8
TaCH$_2^+$ + CH$_4$ $\longrightarrow$ Ta(CH$_2$)$_2^+$ + H$_2$	1.0±0.3
Ta(CH$_2$)$_2^+$ + CH$_4$ $\longrightarrow$ Ta(CH$_2$)$_3^+$ + H$_2$	1.9±0.6
Ta(CH$_2$)$_3^+$ + CH$_4$ $\longrightarrow$ Ta(CH$_2$)$_4^+$ + H$_2$	0.14±0.03
Ta$^+$ + CO$_2$ $\longrightarrow$ TaO$^+$ + CO	5.8±2.3
TaO$^+$ + CO$_2$ $\longrightarrow$ TaO$_2^+$ + CO	5.0±1.3
TaO$^+$ + CH$_4$ $\longrightarrow$ TaOCH$_2^+$ + H$_2$	1.3±1.1
TaOCH$_2^+$ + CO$_2$ $\longrightarrow$ TaO$_2^+$ + C$_2$H$_2$O	20.3±11.4
Ta(CH$_2$)$_2^+$ + CH$_4$ $\longrightarrow$ Ta(CH$_2$)$_2$(CH$_4$)$^+$	3.5±3.1
TaO$_2^+$ + CH$_4$ $\longrightarrow$ TaO$_2$(CH$_4$)$^+$	2.4±1.4
TaCH$_2^+$ + CO$_2$ $\longrightarrow$ TaO$^+$ + H$_2$C$_2$O	19.8±7.0
TaOCH$_2^+$ + CO$_2$ $\longrightarrow$ TaOCH$_2$(CO$_2$)$^+$	6.3±1.5
TaO$_2$(CH$_4$)$^+$ + CO$_2$ $\longrightarrow$ TaO$_2$(CH$_4$)$^+$(CO$_2$)$^+$	12.4±6.7
TaOCH$_2$(CO$_2$)$^+$ + CO$_2$ $\longrightarrow$ TaOCH$_2$(CO$_2$)$_2^+$	15.4±9.7

TABLE 6.4: Bimolecular rate coefficients $k^{(2)}$ in units of 10^{-10} cm^3 s^{-1} of the reactions between isolated Ta$_4^+$ and a mixture of CH$_4$ and CO$_2$. For most of the reactions an average value of two measurements is presented with error bars reflecting corresponding statistical uncertainties. Fractions of CO$_2$ in the buffer gas are either 25 or 50 ppm, fractions of methane are either 2500 or 5000 ppm, the relative ratio [CH$_4$]:[CO$_2$] is equal to 100. The total pressure in the trap is 0.82 Pa. Note, that Ta$_4$CO$^+$ is isobaric with Ta$_4$(CH$_2$)$_2^+$.

reactions	$k^{(2)}$
Ta$_4^+$ + CH$_4$ $\longrightarrow$ Ta$_4$CH$_2^+$ + H$_2$	0.17±0.08
Ta$_4$CH$_2^+$ + CH$_4$ $\longrightarrow$ Ta$_4$(CH$_2$)$_2^+$ + H$_2$	0.14±0.01
Ta$_4$CH$_2^+$ + CO$_2$ $\longrightarrow$ Ta$_4$CO$^+$ + H$_2$CO	6.7±6.3
Ta$_4$CO$^+$ + CO$_2$ $\longrightarrow$ Ta$_4$CO$_2^+$ + CO	no fit
Ta$_4$CO$_2^+$ + CO$_2$ $\longrightarrow$ Ta$_4$CO$_3^+$ + CO	29.8±20.1
Ta$_4$CO$_3^+$ + CO$_2$ $\longrightarrow$ Ta$_4$CO$_4^+$ + CO	15.3
Ta$_4$CO$_4^+$ + CO$_2$ $\longrightarrow$ Ta$_4$CO$_5^+$ + CO	30.1±6.4
Ta$_4^+$ + CO$_2$ $\longrightarrow$ Ta$_4$O$^+$ + CO	26.3±8.7
Ta$_4$O$^+$ + CO$_2$ $\longrightarrow$ Ta$_4$O$_2^+$ + CO	19.4±6.7
Ta$_4$O$^+$ + CH$_4$ $\longrightarrow$ Ta$_4$OCH$_2^+$ + H$_2$	0.44±0.12
Ta$_4$OCH$_2^+$ + CH$_4$ $\longrightarrow$ Ta$_4$O(CH$_2$)$_2^+$ + H$_2$	0.44±0.16
Ta$_4$CH$_2^+$ + CO$_2$ $\longrightarrow$ Ta$_4$CH$_2$(CO$_2$)$^+$	110.0±50.2
Ta$_4$CH$_2$(CO$_2$)$^+$ + CO$_2$ $\longrightarrow$ Ta$_4$CH$_2$(CO$_2$)$_2^+$	48.8±18.1
Ta$_4$O$^+$ + CO$_2$ $\longrightarrow$ Ta$_4$O(CO$_2$)$^+$	3.4±0.8
Ta$_4$O$_2^+$ + CO$_2$ $\longrightarrow$ Ta$_4$O$_2$(CO$_2$)$^+$	91.1
Ta$_4$CO$^+$ + CO$_2$ $\longrightarrow$ Ta$_4$CO(CO$_2$)$^+$	38.8±20.2
Ta$_4$CO$_2^+$ + CO$_2$ $\longrightarrow$ Ta$_4$CO$_2$(CO$_2$)$^+$	34.3±17.4
Ta$_4$CH$_2$O$^+$ + CO$_2$ $\longrightarrow$ Ta$_4$CH$_2$O(CO$_2$)$^+$	24.1±16.9
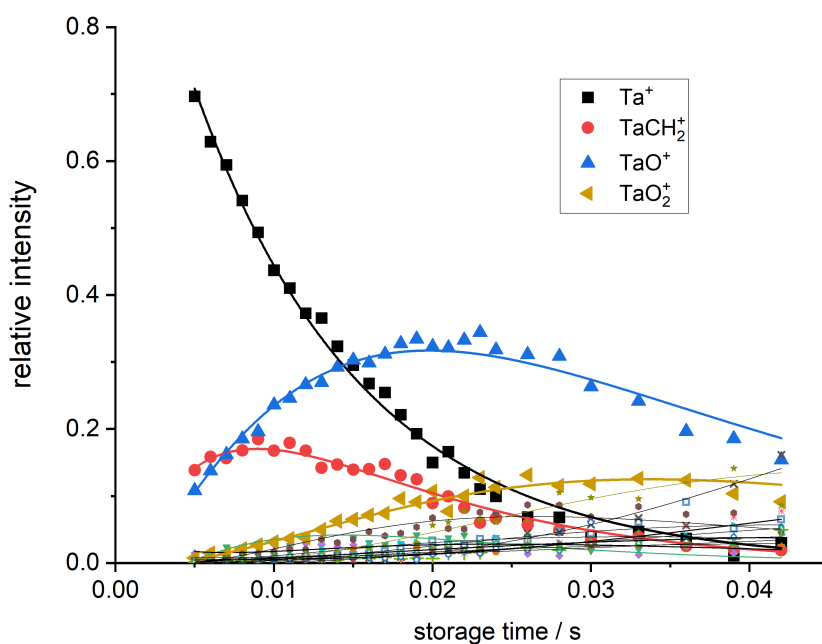
FIGURE 6.4: Kinetic analysis of the room-temperature reaction of mass-selected Ta$^+$ ions with a mixture of CO$_2$ and CH$_4$. The experimental data points correspond to the normalized intensities of the reactants, intermediates, and products. The total pressure in the trap amounts to 0.82 Pa, the proportion of carbon dioxide in the mixture is 20 ppm and of CH$_4$ 100 ppm.
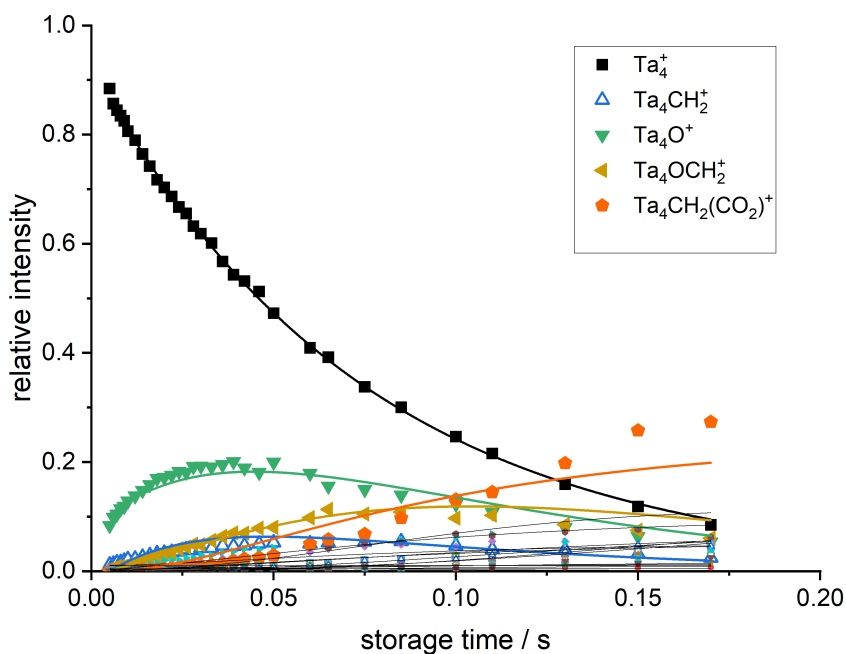
FIGURE 6.5: Kinetic analysis of the room-temperature reaction of mass-selected Ta$_4^+$ ions with a mixture of CO$_2$ and CH$_4$. The experimental data points correspond to the normalized intensities of the reactants, intermediates, and products. The total pressure in the trap amounts to 0.82 Pa, the proportion of carbon dioxide in the mixture is 25 ppm and of CH$_4$ 2500 ppm.
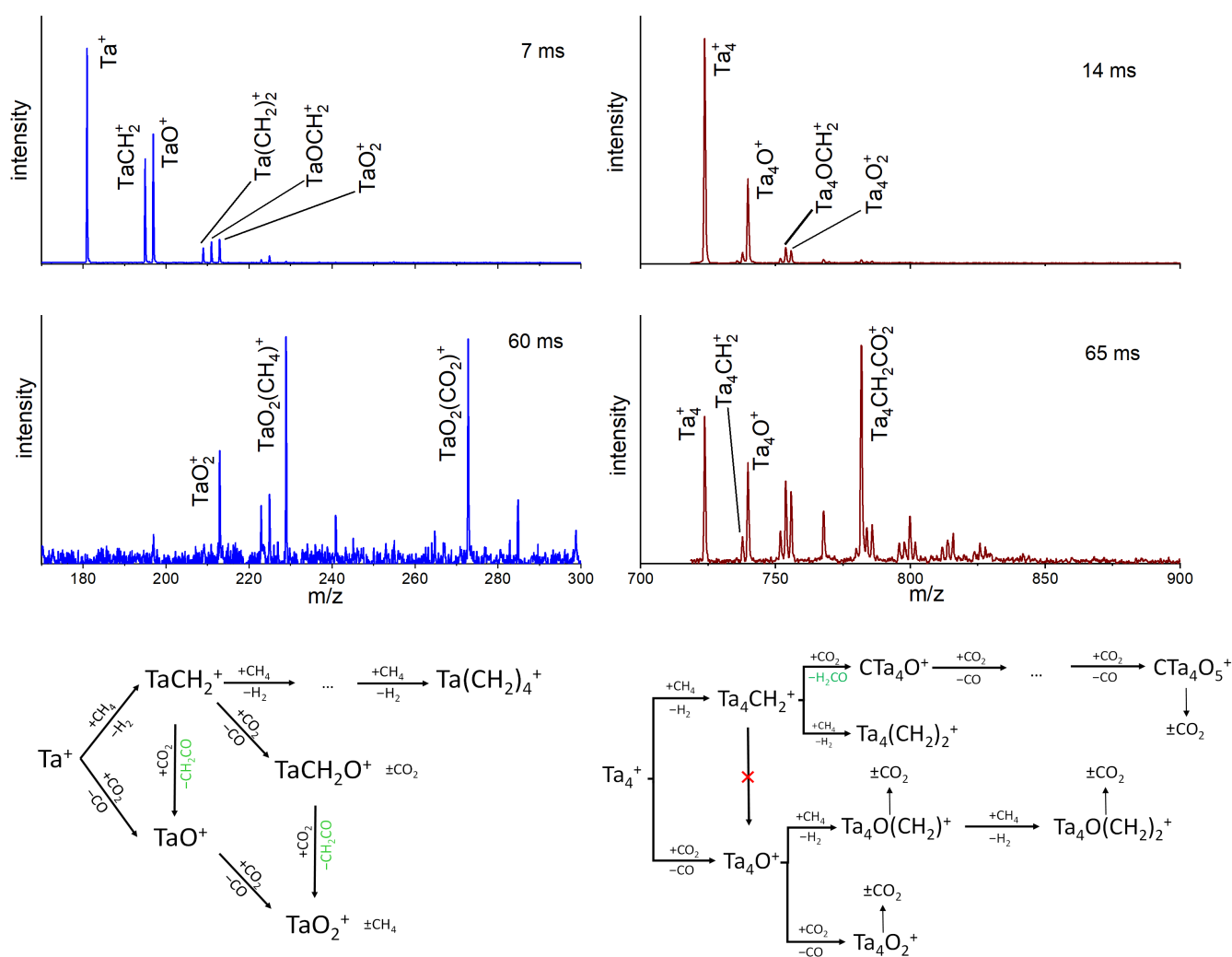
FIGURE 6.6: Left: mass spectra taken at different storage times and the underlying mechanism of the reactions between isolated Ta^+ and the mixture of 300 ppm CH_4 and 35 ppm CO_2 in the buffer gas. Right: mass spectra taken at different storage times and the underlying mechanism of the reactions between isolated Ta_4^+ and the mixture of 5000 ppm CH_4 and 50 ppm CO_2 in the buffer gas. The total pressure in the trap amounts to 0.82 Pa.

7 Conclusion and Outlook

Among atomic cations of all transition metals, only Nb^+, Ta^+, and W^+ are capable to perform both methane dehydrogenation and CO_2 decarbonylation reactions in the gas phase[81, 96]. The chemistry of tantalum clusters of various sizes and their oxides towards methane activation has been covered in numerous publications from both experimental and theoretical perspectives[73, 108–112, 135, 136, 162, 163]. The process of CO_2 activation by Ta clusters, however, has not received any attention prior to the work presented in this thesis. In this work, bare Ta_n^+ clusters (n = 1-16) reacted with CO_2 under multi-collisional conditions in the ring electrode ion trap (REIT). Two reaction regimes were discovered for this system: whereas small bare clusters Ta_{1-6}^+ carry out exclusively an oxygen-atom transfer when associated with the first reacting molecule of carbon dioxide, the dominating pathway for the reactions between Ta_{8-16}^+ and CO_2 is physi- or chemisorption without the release of CO. Ta_7^+ makes up a transition between these regimes with OAT being the main pathway, but with some CO_2 molecules being adsorbed. The reactivity of the bare tantalum clusters towards carbon dioxide can be explained in terms of thermochemical, electronic, and geometric considerations. Thus, preliminary calculations of the reaction heats revealed that there is a substantial shift in exothermicity between the decarbonylation of CO_2 by Ta_6^+ and Ta_8^+. Kinetically, inefficient decarbonylation by larger clusters can be attributed to the lack of valent 6s electrons which are necessary to activate a C-OC bond.

Furthermore, the activation of both methane and carbon dioxide in a single reaction system was investigated for Ta^+ and Ta_4^+. The former system was previously studied by Wesendrup and Schwarz under single-collision conditions[85]. They discovered, that a tantalum-carbene complex $TaCH_2^+$ carries out an OAT from a CO_2 molecule to form $TaOCH_2^+$, which further reacts with another molecule of CO_2 with the release of a neutral [2C,2H,O] species and formation of TaO_2^+. The results of the REIT experiment under multi-collision conditions indicate the presence of a parallel reaction pathway — namely, the direct coupling of $TaCH_2^+$ with CO_2 to form TaO^+ with the release of [2C,2H,O]. The quantum-chemical insight into the reactivity pattern reveals a high energy barrier related to the dissociation of a neutral moiety, which is consistent with the experimental observation of rather low reaction efficiency. Besides, the reaction of C-O coupling was discovered to occur in the $Ta_4CH_2^+/CO_2$ system. More specifically, $Ta_4CH_2^+$ undergoes a C-O coupling with a CO_2 molecule followed by the dissociation of [2H,C,O] compound and formation of

Ta_4CO^+.

The carbide dihydride structure of the $[4Ta,C,2H]^+$ ion was previously calculated to lie lower in energy than the more usual carbene[111]. This motivated a thorough structural analysis of this species using the IRMPD spectroscopy[171]. In this work, the calculated vibrational spectra of three structural isomers were compared with the experimental data. The spectra show no indication of the carbene structure, which has been usually determined for $[M,C,2H]^+$ species before[162–164, 166, 167]. Moreover, the vibrational patterns evidenced rather the dominance of the carbide dihydride isomer; however, the presence of a carbyne hydrides cannot be discarded. The carbide dihydride structure has not been reported before for the products of methane dehydrogenation by metal clusters. However, this very atomic arrangement of $[4Ta,C,2H]^+$ can be responsible for the aforementioned reactivity of this ion with CO_2 and for its reactivity with O_2[86]. These findings emphasise once more the importance of extensive investigations of metal clusters by various gas-phase techniques.

Finally, the reaction of $Ta_8O_2^+$ with CH_4 was studied in the REIT under various temperatures. Previously, it has been demonstrated that an oxygen-atom ligand can significantly enhance the reactivity of tantalum clusters towards activation of methane[111]. The accurate kinetic analysis involving the isotopic substitution of methane by its deuterated analogue revealed that the reaction of $Ta_8O_2^+$ with CH_4 proceeds *via* a catalytic cycle, in which two methane molecules couple to form two neutral reaction products: a molecule of hydrogen and a molecule of, presumably, ethane.

The scientific works discussed in this thesis exemplify the importance of gas-phase investigations of size-selected metal clusters as fine models for the "real-world" catalytic systems. The ability to detect reaction intermediates enables thorough kinetic analysis of reaction pathways. Coupled with quantum-chemical modelling of studied systems, it allows to match the reactivity of clusters to their physical properties. Thus, the spectroscopic investigation of $[4Ta,C,2H]^+$ supported by DFT calculations allows to gain insight into the reactivity of this species towards oxygen or carbon dioxide. Analogously, a theoretical treatment of Ta_n^+/CO_2 system helps explain its two-regime evolution, which can be found useful in further studies of CO_2 activation.

The design of the ring electrode ion trap allows to conduct gas-phase experiments under multi-collision conditions at various temperatures. Such experimental conditions may be able to bridge the "pressure gap" between the high vacuum and condensed phases[72] and allow for the detection of reaction pathways, inaccessible under single-collision environment[46]. For example, the discovery of the second path of C-C coupling by Ta^+ proves REIT experiments advantageous over those conducted under ultra-high-vacuum. The observation of a catalytic cycle in the $Ta_8O_2^+/CH_4$ system further evidences the advantage of gas-phase experiments,

in which the kinetics of relatively large, ligated clusters can be accurately studied.

The latter system is subject to further analysis, both theoretical and experimental. First, spectroscopic examination of the physical and electronic structure of $Ta_8O_2^+$ may help uncover the cause of its extraordinary reactivity with methane. Second, deposited tantalum clusters of various sizes can be probed by surface techniques and tuned to serve as active sites of heterogeneous catalysts. Such an experiment would bridge the gas-phase and surface approaches. Alternatively, the remarkable ability of Ta clusters to perform C-C and C-O coupling reactions can be employed in the design of atomically precise bi-metallic catalysts for controllable conversion of CO_2 and CH_4. In this regard, gas-phase experimental techniques serve excellent tools for discovery and characterization of such candidates.

Bibliography

[1] Hugh S. Taylor. *Catalysis*. Encyclopedia Britannica. 2018.

[2] R. S. Hanson and T. E. Hanson. "Methanotrophic bacteria." In: *Microbiology and Molecular Biology Reviews* 60.2 (1996), pp. 439–471.

[3] Stuart J. Ferguson. "Nitrogen cycle enzymology". In: *Current Opinion in Chemical Biology* 2.2 (1998), pp. 182–193.

[4] Brian M. Hoffman et al. "Mechanism of Nitrogen Fixation by Nitrogenase: The Next Stage". In: *Chemical Reviews* 114.8 (2014), pp. 4041–4062.

[5] Bikash Kumar and Pradeep Verma. "Biomass-based biorefineries: An important architype towards a circular economy". In: *Fuel* 288 (2021), p. 119622.

[6] Piet W.N.M. van Leeuwen and Carmen Claver. *Recent Advances in Nanoparticle Catalysis*. Molecular Catalysis 1. Springer International Publishing, 2020.

[7] M. Haruta et al. "Gold catalysts prepared by coprecipitation for low-temperature oxidation of hydrogen and of carbon monoxide". In: *Journal of Catalysis* 115.2 (1989), pp. 301–309.

[8] Masatake Haruta. "Size- and support-dependency in the catalysis of gold". In: *Catalysis Today* 36.1 (1997), pp. 153–166.

[9] Richard Feynman. "There's Plenty of Room at the Bottom". In: *Engineering and Science* 23 (5 1959), pp. 22–36.

[10] Robert C. Weast, ed. *CRC Handbook of Chemistry and Physics*. 63rd ed. CRC Press, 1982.

[11] Joseph M. Fox III. "The Different Catalytic Routes for Methane Valorization: An Assessment of Processes for Liquid Fuels". In: *Catalysis Reviews* 35.2 (1993), pp. 169–212.

[12] P. Bousquet et al. "Contribution of anthropogenic and natural sources to atmospheric methane variability". In: *Nature* 443.7110 (2006), pp. 439–443.

[13] Dorian Q Fuller et al. "The contribution of rice agriculture and livestock pastoralism to prehistoric methane levels: An archaeological assessment". In: *The Holocene* 21.5 (2011), pp. 743–759.

[14] T. Baba and A. Miyaji. "Overview of Direct Methane Conversion to Chemicals with C–O and C–C Bonds." In: *Catalysis and the Mechanism of Methane Conversion to Chemicals*. Springer Singapore, 2020, pp. 1–21.

[15] Ray Boswell and Timothy S. Collett. "Current perspectives on gas hydrate resources". In: *Energy Environ. Sci.* 4 (4 2011), pp. 1206–1215.

[16]   Matthias Peter and Tobin J. Marks. "Platinum Metal-Free Catalysts for Selective Soft Oxidative Methane → Ethylene Coupling. Scope and Mechanistic Observations". In: *Journal of the American Chemical Society* 137.48 (2015), pp. 15234–15240.

[17]   Shanfu Liu et al. "'Soft' oxidative coupling of methane to ethylene: Mechanistic insights from combined experiment and theory". In: *Proceedings of the National Academy of Sciences* 118.23 (2021).

[18]   Suji Yoon et al. "Study on the unsteady state oxidative coupling of methane: effects of oxygen species from O_2, surface lattice oxygen, and CO_2 on the C_{2+} selectivity". In: *RSC Adv.* 10 (59 2020), pp. 35889–35897.

[19]   R. Pitchai and K. Klier. "Partial Oxidation of Methane". In: *Catalysis Reviews* 28.1 (1986), pp. 13–88.

[20]   Donghyun Park and Jeewon Lee. "Biological conversion of methane to methanol". In: *Korean Journal of Chemical Engineering* 30.5 (2013), pp. 977–987.

[21]   Ouarda Benlounes et al. "Direct oxidation of methane to oxygenates over heteropolyanions". In: *Journal of Natural Gas Chemistry* 17.3 (2008), pp. 309–312.

[22]   *The Future of Hydrogen.* Tech. rep. Paris: IEA, all rights reserved, 2019.

[23]   Raimund Horn and Robert Schlögl. "Methane Activation by Heterogeneous Catalysis". In: *Catalysis Letters* 145.1 (2015), pp. 23–39.

[24]   T. T. Isson et al. "Evolution of the Global Carbon Cycle and Climate Regulation on Earth". In: *Global Biogeochemical Cycles* 34.2 (2020).

[25]   P. Friedlingstein et al. "Global Carbon Budget 2019". In: *Earth Syst. Sci. Data* 11.4 (2019), pp. 1783–1838.

[26]   Thomas P. Senftle and Emily A. Carter. "The Holy Grail: Chemistry Enabling an Economically Viable CO_2 Capture, Utilization, and Storage Strategy". In: *Accounts of Chemical Research* 50.3 (2017), pp. 472–475.

[27]   Mar Pérez-Fortes, Andrei Bocin-Dumitriu, and Evangelos Tzimas. "CO_2 Utilization Pathways: Techno-Economic Assessment and Market Opportunities". In: *Energy Procedia* 63 (2014). 12th International Conference on Greenhouse Gas Control Technologies, GHGT-12, pp. 7968–7975.

[28]   Michele Aresta, Angela Dibenedetto, and Antonella Angelini. "Catalysis for the Valorization of Exhaust Carbon: from CO_2 to Chemicals, Materials, and Fuels. Technological Use of CO_2". In: *Chemical Reviews* 114.3 (2014), pp. 1709–1742.

[29]   Mette Mikkelsen, Mikkel Jørgensen, and Frederik C. Krebs. "The teraton challenge. A review of fixation and transformation of carbon dioxide". In: *Energy Environ. Sci.* 3 (1 2010), pp. 43–81.

[30]   James A. Dumesic, George W. Huber, and Michel Boudart. "Principles of Heterogeneous Catalysis". In: *Handbook of Heterogeneous Catalysis*. American Cancer Society, 2008. Chap. 1.1.

[31]   Pierre Schwach, Xiulian Pan, and Xinhe Bao. "Direct Conversion of Methane to Value-Added Chemicals over Heterogeneous Catalysts: Challenges and Prospects". In: *Chemical Reviews* 117.13 (2017), pp. 8497–8520.

[32]   Run-Ping Ye et al. "CO_2 hydrogenation to high-value products via heterogeneous catalysis". In: *Nature Communications* 10.1 (2019), p. 5698.

[33] Ho Seok Whang et al. "Heterogeneous catalysts for catalytic CO_2 conversion into value-added chemicals". In: *BMC Chemical Engineering* 1.1 (2019), p. 9.

[34] Jiawei Zhong et al. "State of the art and perspectives in heterogeneous catalysis of CO_2 hydrogenation to methanol". In: *Chem. Soc. Rev.* 49 (5 2020), pp. 1385–1413.

[35] Min Bum Park, Eun Duck Park, and Wha-Seung Ahn. "Recent Progress in Direct Conversion of Methane to Methanol Over Copper-Exchanged Zeolites". In: *Frontiers in Chemistry* 7 (2019), p. 514.

[36] Kimberly T. Dinh et al. "Viewpoint on the Partial Oxidation of Methane to Methanol Using Cu- and Fe-Exchanged Zeolites". In: *ACS Catalysis* 8.9 (2018), pp. 8306–8313.

[37] M. Haris Mahyuddin et al. "Direct Conversion of Methane to Methanol by Metal-Exchanged ZSM-5 Zeolite (Metal = Fe, Co, Ni, Cu)". In: *ACS Catalysis* 6.12 (2016), pp. 8321–8331.

[38] Nikolay Kosinov and Emiel J. M. Hensen. "Reactivity, Selectivity, and Stability of Zeolite-Based Catalysts for Methane Dehydroaromatization". In: *Advanced Materials* 32.44 (2020), p. 2002565.

[39] Xiang Yu et al. "Selective photocatalytic conversion of methane into carbon monoxide over zinc-heteropolyacid-titania nanocomposites". In: *Nature Communications* 10.1 (2019), p. 700.

[40] Zongwei Sun, Chunling Wang, and Yun Hang Hu. "Highly selective photocatalytic conversion of methane to liquid oxygenates over silicomolybdic-acid/TiO_2 under mild conditions". In: *J. Mater. Chem. A* 9 (3 2021), pp. 1713–1719.

[41] Lu Li et al. "Photoinduced Conversion of Methane into Benzene over GaN Nanowires". In: *Journal of the American Chemical Society* 136.22 (2014), pp. 7793–7796.

[42] Hui Song et al. "Solar-Energy-Mediated Methane Conversion". In: *Joule* 3.7 (2019), pp. 1606–1636.

[43] Zhonghua Li et al. "Photocatalytic and Thermocatalytic Conversion of Methane". In: *Solar RRL* (2021), p. 2000596.

[44] Byungik Lee and Takashi Hibino. "Efficient and selective formation of methanol from methane in a fuel cell-type reactor". In: *Journal of Catalysis* 279.2 (2011), pp. 233–240.

[45] Logi Arnarson et al. "Fundamental limitation of electrocatalytic methane conversion to methanol". In: *Phys. Chem. Chem. Phys.* 20 (16 2018), pp. 11152–11159.

[46] Sandra M. Lang and Thorsten M. Bernhardt. "Gas phase metal cluster model systems for heterogeneous catalysis". In: *Phys. Chem. Chem. Phys.* 14 (26 2012), pp. 9255–9269.

[47] Walt A. de Heer. "The physics of simple metal clusters: experimental aspects and simple models". In: *Rev. Mod. Phys.* 65 (3 1993), pp. 611–676.

[48] P.B. Armentrout. "The Thermochemistry of Adsorbates on Transition Metal Cluster Ions: Relationship to Bulk-Phase Properties". In: *European Journal of Mass Spectrometry* 9.6 (2003), pp. 531–538.

[49] Diethard K. Böhme and Helmut Schwarz. "Gas-Phase Catalysis by Atomic and Cluster Metal Ions: The Ultimate Single-Site Catalysts". In: *Angewandte Chemie International Edition* 44.16 (2005), pp. 2336–2354.

[50] Zhixun Luo and Shiv N. Khanna. *Metal Clusters and Their Reactivity*. Springer Singapore, 2020.

[51] R. A. Larsen, S. K. Neoh, and D. R. Herschbach. "Seeded supersonic alkali atom beams". In: *Review of Scientific Instruments* 45.12 (1974), pp. 1511–1516.

[52] K. Sattler, J. Mühlbach, and E. Recknagel. "Generation of Metal Clusters Containing from 2 to 500 Atoms". In: *Phys. Rev. Lett.* 45 (10 1980), pp. 821–824.

[53] W. D. Knight et al. "Electronic Shell Structure and Abundances of Sodium Clusters". In: *Phys. Rev. Lett.* 52 (24 1984), pp. 2141–2143.

[54] T. P. Martin et al. "Shell structure of clusters". In: *The Journal of Physical Chemistry* 95.17 (1991), pp. 6421–6429.

[55] I. M. Goldby et al. "Gas condensation source for production and deposition of size-selected metal clusters". In: *Review of Scientific Instruments* 68.9 (1997), pp. 3327–3334.

[56] Masamichi Yamashita and John B. Fenn. "Electrospray ion source. Another variation on the free-jet theme". In: *The Journal of Physical Chemistry* 88.20 (1984), pp. 4451–4459.

[57] Guangdi Wang and Richard B. Cole. "Charged residue versus ion evaporation for formation of alkali metal halide cluster ions in ESI". In: *Analytica Chimica Acta* 406.1 (2000), pp. 53–65.

[58] Jeremy T. O'Brien and Evan R. Williams. "Hydration of Gaseous Copper Dications Probed by IR Action Spectroscopy". In: *The Journal of Physical Chemistry A* 112.26 (2008), pp. 5893–5901.

[59] Theresa E. Cooper, D. R. Carl, and P. B. Armentrout. "Hydration Energies of Zinc(II): Threshold Collision-Induced Dissociation Experiments and Theoretical Studies". In: *The Journal of Physical Chemistry A* 113.49 (2009), pp. 13727–13741.

[60] Matthew F. Bush, Richard J. Saykally, and Evan R. Williams. "Hydration of the Calcium Dication: Direct Evidence for Second Shell Formation from Infrared Spectroscopy". In: *ChemPhysChem* 8.15 (2007), pp. 2245–2253.

[61] Arthur T. Blades et al. "Ion-molecule clusters involving doubly charged metal ions (M2+)". In: *International Journal of Mass Spectrometry and Ion Processes* 102 (1990), pp. 251–267.

[62] T. G. Dietz et al. "Laser production of supersonic metal cluster beams". In: *The Journal of Chemical Physics* 74.11 (1981), pp. 6511–6512.

[63] Carleton J. Howard. "Kinetic measurements using flow tubes". In: *The Journal of Physical Chemistry* 83.1 (1979), pp. 3–9.

[64] N.G. Adams and D. Smith. "The selected ion flow tube (SIFT); A technique for studying ion-neutral reactions". In: *International Journal of Mass Spectrometry and Ion Physics* 21.3 (1976), pp. 349–359.

[65] S.-G. He et al. "Reaction of niobium and tantalum neutral clusters with low pressure, unsaturated hydrocarbons in a pickup cell: From dehydrogenation to Met-Car formation". In: *The Journal of Chemical Physics* 125.16 (2006), p. 164306.

[66] P. B. Armentrout. "Reactions and Thermochemistry of Small Transition Metal Cluster Ions". In: *Annual Review of Physical Chemistry* 52.1 (2001), pp. 423–461.

[67] Thorsten M. Bernhardt. "Gas-phase kinetics and catalytic reactions of small silver and gold clusters". In: *International Journal of Mass Spectrometry* 243.1 (2005), pp. 1–29.

[68] Daniel J. Goebbert, Gerard Meijer, and Knut R. Asmis. "10 K Ring Electrode Trap—Tandem Mass Spectrometer for Infrared Spectroscopy of Mass Selected Ions". In: *AIP Conference Proceedings* 1104.1 (2009), pp. 22–29.

[69] G.G. Dolnikowski et al. "Ion-trapping technique for ion/molecule reaction studies in the center quadrupole of a triple quadrupole mass spectrometer". In: *International Journal of Mass Spectrometry and Ion Processes* 82.1 (1988), pp. 1–15.

[70] A. G. Marshall, C. L. Hendrickson, and G. S. Jackson. "Fourier transform ion cyclotron resonance mass spectrometry: a primer." In: *Mass Spectrom Rev.* 17 (1 1998), pp. 1–35.

[71] Karsten Eller and Helmut Schwarz. "Organometallic chemistry in the gas phase. A comparative fourier transform-ion cyclotron resonance/tandem mass spectrometry study". In: *International Journal of Mass Spectrometry and Ion Processes* 93.2 (1989), pp. 243–257.

[72] Helmut Schwarz. "Chemistry with Methane: Concepts Rather than Recipes". In: *Angewandte Chemie International Edition* 50.43 (2011), pp. 10096–10115.

[73] Helmut Schwarz et al. "Unexpected Mechanistic Variants in the Thermal Gas-Phase Activation of Methane". In: *Organometallics* 36.1 (2017), pp. 8–17.

[74] Sandra Feyel et al. "Activation of Methane by Oligomeric $(Al_2O_3)_x^+$ (*x*=3,4,5): The Role of Oxygen-Centered Radicals in Thermal Hydrogen-Atom Abstraction". In: *Angewandte Chemie International Edition* 47.10 (2008), pp. 1946–1950.

[75] Maria Schlangen and Helmut Schwarz. "Ligand and electronic-structure effects in metal-mediated gas-phase activation of methane: A cold approach to a hot problem". In: *Dalton Trans.* (46 2009), pp. 10155–10165.

[76] Wenzhen Lai et al. "Hydrogen-Abstraction Reactivity Patterns from A to Y: The Valence Bond Way". In: *Angewandte Chemie International Edition* 51.23 (2012), pp. 5556–5578.

[77] Maria Schlangen and Helmut Schwarz. "Effects of Ligands, Cluster Size, and Charge State in Gas-Phase Catalysis: A Happy Marriage of Experimental and Computational Studies". In: *Catalysis Letters* 142.11 (2012), pp. 1265–1278.

[78] Detlef Schröder, Sason Shaik, and Helmut Schwarz. "Two-State Reactivity as a New Concept in Organometallic Chemistry". In: *Accounts of Chemical Research* 33.3 (2000), pp. 139–145.

[79] Detlef Schröder and Helmut Schwarz. "FeO$^+$ Activates Methane". In: *Angewandte Chemie International Edition in English* 29.12 (1990), pp. 1433–1434.

[80] Matthew F. Ryan et al. "Radical-like Behavior of Manganese Oxide Cation in Its Gas-Phase Reactions with Dihydrogen and Alkanes". In: *Journal of the American Chemical Society* 117.7 (1995), pp. 2033–2040.

[81] Alireza Shayesteh et al. "Reactions of Atomic Cations with Methane: Gas Phase Room-Temperature Kinetics and Periodicities in Reactivity". In: *The Journal of Physical Chemistry A* 113.19 (2009), pp. 5602–5611.

[82] Karl K. Irikura and J. L. Beauchamp. "Electronic structure considerations for methane activation by third-row transition-metal ions". In: *The Journal of Physical Chemistry* 95.21 (1991), pp. 8344–8351.

[83] Helmut Schwarz. "Relativistic Effects in Gas-Phase Ion Chemistry: An Experimentalist's View". In: *Angewandte Chemie International Edition* 42.37 (2003), pp. 4442–4454.

[84] Ralf Wesendrup, Detlef Schröder, and Helmut Schwarz. "Catalytic Pt^+-Mediated Oxidation of Methane by Molecular Oxygen in the Gas Phase". In: *Angewandte Chemie International Edition in English* 33.11 (1994), pp. 1174–1176.

[85] Ralf Wesendrup and Helmut Schwarz. "Tantalum-Mediated Coupling of Methane and Carbon Dioxide in the Gas Phase". In: *Angewandte Chemie International Edition in English* 34.18 (1995), pp. 2033–2035.

[86] T. Masubuchi et al. "Thermal C–O coupling reactions of Ta methylene clusters $[Ta_nCH_2]^+$ (n = 1, 4) with O_2". In: *Phys. Chem. Chem. Phys.* 21 (37 2019), pp. 20743–20749.

[87] Sandra M. Lang et al. "Temperature-Tunable Selective Methane Catalysis on Au_2^+: From Cryogenic Partial Oxidation Yielding Formaldehyde to Cold Ethylene Production". In: *The Journal of Physical Chemistry C* 115.14 (2011), pp. 6788–6795.

[88] Sandra M. Lang et al. "Methane Activation and Catalytic Ethylene Formation on Free Au_2^+". In: *Angewandte Chemie International Edition* 49.5 (2010), pp. 980–983.

[89] Nicholas S. Shuman et al. "Au_2^+ cannot catalyze conversion of methane to ethene at low temperature". In: *Catal. Sci. Technol.* 9 (11 2019), pp. 2767–2780.

[90] Lucie Jašíková and Jana Roithová. "Infrared Multiphoton Dissociation Spectroscopy with Free-Electron Lasers: On the Road from Small Molecules to Biomolecules". In: *Chemistry – A European Journal* 24.14 (2018), pp. 3374–3390.

[91] Jana Roithová and Joost M. Bakker. "Ion spectroscopy in methane activation". In: *Mass Spectrometry Reviews* (in print).

[92] Dorothy H. Gibson. "The Organometallic Chemistry of Carbon Dioxide". In: *Chemical Reviews* 96.6 (1996), pp. 2063–2096.

[93] J. Mascetti and M. Tranquille. "Fourier transform infrared studies of atomic titanium, vanadium, chromium, iron, cobalt, nickel and copper reactions with carbon dioxide in low-temperature matrices". In: *The Journal of Physical Chemistry* 92.8 (1988), pp. 2177–2184.

[94] Leah G. Dodson, Michael C. Thompson, and J. Mathias Weber. "Characterization of Intermediate Oxidation States in CO_2 Activation". In: *Annual Review of Physical Chemistry* 69.1 (2018), pp. 231–252.

[95] M. Sodupe et al. "Theoretical Study of M^+-CO_2 and OM^+CO Systems for First Transition Row Metal Atoms". In: *The Journal of Physical Chemistry A* 101.42 (1997), pp. 7854–7859.

[96] Gregory K. Koyanagi and Diethard K. Bohme. "Gas-Phase Reactions of Carbon Dioxide with Atomic Transition-Metal and Main-Group Cations: Room-Temperature Kinetics and Periodicities in Reactivity". In: *The Journal of Physical Chemistry A* 110.4 (2006), pp. 1232–1241.

[97] Ping Cheng, Gregory K. Koyanagi, and Diethard K. Bohme. "Gas-Phase Reactions of Atomic Lanthanide Cations with CO_2 and CS_2: Room-Temperature Kinetics and Periodicities in Reactivity". In: *The Journal of Physical Chemistry A* 110.47 (2006), pp. 12832–12838.

[98]   Helmut Schwarz. "Metal-mediated activation of carbon dioxide in the gas phase: Mechanistic insight derived from a combined experimental/computational approach". In: *Coordination Chemistry Reviews* 334 (2017), pp. 112–123.

[99]   Shaodong Zhou et al. "Sequential Gas-Phase Activation of Carbon Dioxide and Methane by $[Re(CO)_2]^+$: The Sequence of Events Matters!" In: *Journal of the American Chemical Society* 139.17 (2017), pp. 6169–6176.

[100] De-Man Han et al. "Carbon dioxide activation by Y atom and Y^+ cation in the gas phase: a density functional theoretical study". In: *Journal of the Chilean Chemical Society* 55 (2010), pp. 121 –125.

[101] James B. Griffin and P. B. Armentrout. "Guided ion-beam studies of the reactions of Fe_n^+ (*n*=1-18) with CO_2: Iron cluster oxide bond energies". In: *The Journal of Chemical Physics* 107.14 (1997), pp. 5345–5355.

[102] M. R. Sievers and P. B. Armentrout. "Potential energy surface for carbon-dioxide activation by V^+: A guided ion beam study". In: *The Journal of Chemical Physics* 102.2 (1995), pp. 754–762.

[103] M.R Sievers and P.B Armentrout. "Gas phase activation of carbon dioxide by niobium and niobium monoxide cations". In: *International Journal of Mass Spectrometry* 179-180 (1998), pp. 103–115.

[104] James B. Griffin and P. B. Armentrout. "Guided ion beam studies of the reactions of Cr_n^+ (*n*=1-18) with CO_2: Chromium cluster oxide bond energies". In: *The Journal of Chemical Physics* 108.19 (1998), pp. 8075–8083.

[105] Nadja Sändig and Wolfram Koch. "A Quantum Chemical View on the Mechanism of the Ta^+-Mediated Coupling of Carbon Dioxide with Methane". In: *Organometallics* 17.11 (1998), pp. 2344–2351.

[106] Qiang Chen et al. "Coupling of Methane and Carbon Dioxide Mediated by Diatomic Copper Boride Cations". In: *Angewandte Chemie International Edition* 57.43 (2018), pp. 14134–14138.

[107] Yuan Yang et al. "Direct Conversion of Methane with Carbon Dioxide Mediated by $RhVO_3^-$ Cluster Anions". In: *Angewandte Chemie International Edition* 58.48 (2019), pp. 17287–17292.

[108] Shaodong Zhou et al. "Differences and Commonalities in the Gas-Phase Reactions of Closed-Shell Metal Dioxide Clusters $[MO_2]^+$ (M=V, Nb, and Ta) with Methane". In: *Chemistry – A European Journal* 22.21 (2016), pp. 7225–7228.

[109] Marjan Firouzbakht et al. "On the Activation of Methane and Carbon Dioxide by $[HTaO]^+$ and $[TaOH]^+$ in the Gas Phase: A Mechanistic Study". In: *Chemistry – A European Journal* 22.30 (2016), pp. 10581–10589.

[110] Shaodong Zhou et al. "Spin-Selective Thermal Activation of Methane by Closed-Shell $[TaO_3]^+$". In: *Angewandte Chemie International Edition* 55.25 (2016), pp. 7257–7260.

[111] Jan F. Eckhard et al. "Thermal Dehydrogenation of Methane Enhanced by μ_2-Oxo Ligands in Tantalum Cluster Cations $[Ta_xO]^+$, *x* = 4, 5". In: *The Journal of Physical Chemistry C* 122.44 (2018), pp. 25628–25637.

[112] Jan F. Eckhard et al. "Room-Temperature Methane Activation Mediated by Free Tantalum Cluster Cations: Size-by-Size Reactivity". In: *The Journal of Physical Chemistry A* 125.24 (2021), pp. 5289–5302.

[113]   Daniel Neuwirth. "The design of a ring electrode ion trap with enhanced mass range: Size-dependent oxidation of tantalum clusters". PhD thesis. Technical University of Munich, 2015.

[114]   U. Heiz et al. "Chemical reactivity of size-selected supported clusters: An experimental setup". In: *Review of Scientific Instruments* 68.5 (1997), pp. 1986–1994.

[115]   Tsugunosuke Masubuchi et al. "An efficient laser vaporization source for chemically modified metal clusters characterized by thermodynamics and kinetics". In: *Review of Scientific Instruments* 89.2 (2018), p. 023104.

[116]   F.A. Mellon. "MASS SPECTROMETRY | Principles and Instrumentation". In: *Encyclopedia of Food Sciences and Nutrition (Second Edition)*. Ed. by Benjamin Caballero. Second Edition. Oxford: Academic Press, 2003, pp. 3739–3749.

[117]   N.V. Konenkov, M. Sudakov, and D.J. Douglas. "Matrix methods for the calculation of stability diagrams in quadrupole mass spectrometry". In: *Journal of the American Society for Mass Spectrometry* 13.6 (2002), pp. 597–613.

[118]   Daniel Neuwirth et al. "Using controlled ion extraction to combine a ring electrode trap with a reflectron time-of-flight mass spectrometer". In: *International Journal of Mass Spectrometry* 387 (2015), pp. 8–15.

[119]   Dieter Gerlich. "Inhomogeneous RF Fields: A Versatile Tool for the Study of Processes with Slow Ions". In: *State-Selected and State-to-State Ion-Molecule Reaction Dynamics*. Vol. 82. John Wiley & Sons, 1992. Chap. Part 1: Experiment.

[120]   Jan Westergren et al. "Noble gas temperature control of metal clusters: A molecular dynamics study". In: *The Journal of Chemical Physics* 107.8 (1997), pp. 3071–3079.

[121]   W. C. Wiley and I. H. McLaren. "Time-of-Flight Mass Spectrometer with Improved Resolution". In: *Review of Scientific Instruments* 26.12 (1955), pp. 1150–1157.

[122]   B. A. Mamyrin et al. "Mass reflection: a new nonmagnetic time-of-flight high resolution mass- spectrometer." In: *Zh. Eksp. Teor. Fiz.* 64.1 (1973), pp. 82–89.

[123]   J. F. Eckhard et al. "Consecutive reactions of small, free tantalum clusters with dioxygen controlled by relaxation dynamics". In: *Phys. Chem. Chem. Phys.* 19 (8 2017), pp. 5985–5993.

[124]   J. F. Eckhard et al. "From oxidative degradation to direct oxidation: size regimes in the consecutive reaction of cationic tantalum clusters with dioxygen". In: *Phys. Chem. Chem. Phys.* 19 (17 2017), pp. 10863–10869.

[125]   A. C. Hindmarsh and L. R. Petzold. *LSODA, Ordinary Differential Equation Solver for Stiff or Non-Stiff System*. 2005.

[126]   Kenneth Levenberg. "A method for the solution of certain non-linear problems in least squares". In: *Quart. Appl. Math.* 2 (1944), pp. 164–168.

[127]   Donald W. Marquardt. "An Algorithm for Least-Squares Estimation of Nonlinear Parameters". In: *Journal of the Society for Industrial and Applied Mathematics* 11.2 (1963), pp. 431–441.

[128]   Tomas Baer and William L. Hase. *Unimolecular Reaction Dynamics: Theory and Experiments*. International Series of Monographs on Chemistry. New York: Oxford University Press, 1996, p. 446.

[129]   Marko Haertelt et al. "Structure Determination of Anionic Metal Clusters via Infrared Resonance Enhanced Multiple Photon Electron Detachment Spectroscopy". In: *The Journal of Physical Chemistry Letters* 2.14 (2011), pp. 1720–1724.

[130]   John R. Eyler. "Infrared multiple photon dissociation spectroscopy of ions in Penning traps". In: *Mass Spectrometry Reviews* 28.3 (2009), pp. 448–467.

[131]   H.P. Freund and Jr. Antonsen T.M. *Principles of Free Electron Lasers*. Springer International Publishing AG, 2018.

[132]   Jos Oomens et al. "Gas-phase infrared multiple photon dissociation spectroscopy of mass-selected molecular ions". In: *International Journal of Mass Spectrometry* 254.1 (2006), pp. 1–19.

[133]   Karl F. Renk. "Basics of Laser Physics". In: Springer International Publishing, 2017. Chap. 19, pp. 347–412.

[134]   Karl K. Irikura and J. L. Beauchamp. "Methane oligomerization in the gas phase by third-row transition-metal ions". In: *Journal of the American Chemical Society* 113.7 (1991), pp. 2769–2770.

[135]   Peter B. Armentrout. "Methane Activation by 5 d Transition Metals: Energetics, Mechanisms, and Periodic Trends". In: *Chemistry – A European Journal* 23.1 (2017), pp. 10–18.

[136]   Laura G. Parke, Chris S. Hinton, and P. B. Armentrout. "Experimental and Theoretical Studies of the Activation of Methane by Ta^+". In: *The Journal of Physical Chemistry C* 111.48 (2007), pp. 17773–17787.

[137]   Manfred M. Kappes and Ralph H. Staley. "Gas-phase oxidation catalysis by transition-metal cations". In: *Journal of the American Chemical Society* 103.5 (1981), pp. 1286–1287.

[138]   Yang Shi and Kent M. Ervin. "Catalytic oxidation of carbon monoxide by platinum cluster anions". In: *The Journal of Chemical Physics* 108.5 (1998), pp. 1757–1760.

[139]   Mark Brönstrup et al. "Platinum Dioxide Cation: Easy to Generate Experimentally but Difficult to Describe Theoretically". In: *Journal of the American Chemical Society* 123.1 (2001), pp. 142–147.

[140]   O. Petru Balaj et al. "Catalytic Oxidation of CO with N_2O on Gas-Phase Platinum Clusters". In: *Angewandte Chemie International Edition* 43.47 (2004), pp. 6519–6522.

[141]   C.-K. Siu et al. "Catalyst poisoning in the conversion of CO and N_2O to CO_2 and N_2 on Pt_4^- in the gas phase". In: *The European Physical Journal D* 43.1 (2007), pp. 189–192.

[142]   Sandra M. Lang et al. "$Pd_6O_4^+$: An Oxidation Resistant yet Highly Catalytically Active Nano-oxide Cluster". In: *Journal of the American Chemical Society* 134.51 (2012), pp. 20654–20659.

[143]   Sandra M. Lang et al. "Low-Temperature CO Oxidation Catalyzed by Free Palladium Clusters: Similarities and Differences to Pd Surfaces and Supported Particles". In: *ACS Catalysis* 5.4 (2015), pp. 2275–2289.

[144]   Xiao-Na Li et al. "Catalytic CO Oxidation on Single Pt-Atom Doped Aluminum Oxide Clusters: Electronegativity-Ladder Effect". In: *The Journal of Physical Chemistry C* 119.27 (2015), pp. 15414–15420.

[145]   Li-Na Wang et al. "Catalytic CO Oxidation by O_2 Mediated by Noble-Metal-Free Cluster Anions $Cu_2VO_{3-5}^-$". In: *Angewandte Chemie International Edition* 57.13 (2018), pp. 3349–3353.

[146] Li-Na Wang, Xiao-Na Li, and Sheng-Gui He. "Catalytic CO Oxidation by Noble-Metal-Free $Ni_2VO_{4,5}^-$ Clusters: A CO Self-Promoted Mechanism". In: *The Journal of Physical Chemistry Letters* 10.5 (2019), pp. 1133–1138.

[147] Sandra M. Lang, Anja Frank, and Thorsten M. Bernhardt. "Activation and Catalytic Dehydrogenation of Methane on Small Pd_x^+ and Pd_xO^+ Clusters". In: *The Journal of Physical Chemistry C* 117.19 (2013), pp. 9791–9800.

[148] Sandra M. Lang, Anja Frank, and Thorsten M. Bernhardt. "Comparison of methane activation and catalytic ethylene formation on free gold and palladium dimer cations: product binding determines the catalytic turnover". In: *Catal. Sci. Technol.* 3 (11 2013), pp. 2926–2933.

[149] Nikita Levin et al. "Catalytic Non-Oxidative Coupling of Methane on $Ta_8O_2^+$". In: *Journal of the American Chemical Society* 142.12 (2020), pp. 5862–5869.

[150] Detlef Schröder and Helmut Schwarz. "Gas-phase activation of methane by ligated transition-metal cations". In: *Proceedings of the National Academy of Sciences* 105.47 (2008), pp. 18114–18119.

[151] Christoph Heinemann, Ralf Wesendrup, and Helmut Schwarz. "Pt^+-mediated activation of methane: theory and experiment". In: *Chemical Physics Letters* 239.1 (1995), pp. 75–83.

[152] Maria Pavlov et al. "Pt^+-Catalyzed Oxidation of Methane: Theory and Experiment". In: *The Journal of Physical Chemistry A* 101.8 (1997), pp. 1567–1579.

[153] Detlef Schröder et al. "Activation of hydrogen and methane by thermalized FeO^+ in the gas phase as studied by multiple mass spectrometric techniques". In: *International Journal of Mass Spectrometry and Ion Processes* 161.1 (1997), pp. 175–191.

[154] Michael Filatov and Sason Shaik. "Theoretical Investigation of Two-State-Reactivity Pathways of H-H Activation by FeO^+: Addition-Elimination, "Rebound", and Oxene-Insertion Mechanisms". In: *The Journal of Physical Chemistry A* 102.21 (1998), pp. 3835–3846.

[155] Maria Schlangen, Detlef Schröder, and Helmut Schwarz. "Ligand and Substrate Effects in Gas-Phase Reactions of NiX^+/RH Couples (X=F, Cl, Br, I; R=CH_3, C_2H_5, nC_3H_7, nC_4H_9)". In: *Chemistry – A European Journal* 13.24 (2007), pp. 6810–6816.

[156] Detlef Schröder and Jana Roithová. "Low-Temperature Activation of Methane: It also Works Without a Transition Metal". In: *Angewandte Chemie International Edition* 45.34 (2006), pp. 5705–5708.

[157] Hannu Häkkinen et al. "Structural, Electronic, and Impurity-Doping Effects in Nanoscale Chemistry: Supported Gold Nanoclusters". In: *Angewandte Chemie International Edition* 42.11 (2003), pp. 1297–1300.

[158] André Fielicke et al. "Infrared Spectroscopy and Binding Geometries of Oxygen Atoms Bound to Cationic Tantalum Clusters". In: *The Journal of Physical Chemistry A* 114.36 (2010), pp. 9755–9761.

[159] Yide Gao et al. "Thermochemistry Is Not a Lower Bound to the Activation Energy of Endothermic Reactions: A Kinetic Study of the Gas-Phase Reaction of Atomic Chlorine with Ammonia". In: *The Journal of Physical Chemistry A* 110.21 (2006), pp. 6844–6850.

[160]   Daravong Soulivong et al. "Non-Oxidative Coupling Reaction of Methane to Ethane and Hydrogen Catalyzed by the Silica-Supported Tantalum Hydride: ($\equiv$SiO)$_2$Ta-H". In: *Journal of the American Chemical Society* 130.15 (2008), pp. 5044–5045.

[161]   D.R. Lide. *CRC Handbook of Chemistry & Physics*. 84th. CRC Press LLC, 2004.

[162]   V. J. F. Lapoutre et al. "Structures of the Dehydrogenation Products of Methane Activation by 5d Transition Metal Cations". In: *The Journal of Physical Chemistry A* 117.20 (2013), pp. 4115–4126.

[163]   Cameron J. Owen et al. "Structures of the dehydrogenation products of methane activation by 5d transition metal cations revisited: Deuterium labeling and rotational contours". In: *The Journal of Chemical Physics* 148.4 (2018), p. 044307.

[164]   Oscar W. Wheeler et al. "Activation of C-H Bonds in Pt$^+$ + xCH$_4$ Reactions, where x = 1–4: Identification of the Platinum Dimethyl Cation". In: *The Journal of Physical Chemistry A* 120.31 (2016), pp. 6216–6227.

[165]   P. B. Armentrout et al. "Spectroscopic Identification of the Carbyne Hydride Structure of the Dehydrogenation Product of Methane Activation by Osmium Cations". In: *Journal of the American Society for Mass Spectrometry* 29.9 (2018), pp. 1781–1790.

[166]   P. B. Armentrout et al. "Infrared Spectroscopy of Gold Carbene Cation (AuCH$_2^+$): Covalent or Dative Bonding?" In: *The Journal of Physical Chemistry A* 123.41 (2019), pp. 8932–8941.

[167]   Oscar W. Wheeler et al. "Sequential activation of methane by Ir$^+$: An IRMPD and theoretical investigation". In: *International Journal of Mass Spectrometry* 435 (2019), pp. 78–92.

[168]   Sandra M. Lang et al. "Selective C-H Bond Cleavage in Methane by Small Gold Clusters". In: *Angewandte Chemie International Edition* 56.43 (2017), pp. 13406–13410.

[169]   Dan J. Harding et al. "Activated Methane on Small Cationic Platinum Clusters". In: *Angewandte Chemie International Edition* 51.3 (2012), pp. 817–819.

[170]   Dan J. Harding and André Fielicke. "Platinum Group Metal Clusters: From Gas-Phase Structures and Reactivities towards Model Catalysts". In: *Chemistry – A European Journal* 20.12 (2014), pp. 3258–3267.

[171]   Jozef Lengyel et al. "Carbide Dihydrides: Carbonaceous Species Identified in Ta$_4^+$-Mediated Methane Dehydrogenation". In: *Angewandte Chemie International Edition* 59.52 (2020), pp. 23631–23635.

[172]   Nick C. Polfer. "Infrared multiple photon dissociation spectroscopy of trapped ions". In: *Chem. Soc. Rev.* 40 (5 2011), pp. 2211–2221.

[173]   Shimanouchi T. *Tables of Molecular Vibrational Frequencies Consolidated Volume I*. Vol. 39. Nat. Bur. Stand. (U.S.), 1972.

[174]   Robert N. Barnett and Uzi Landman. "Born-Oppenheimer molecular-dynamics simulations of finite systems: Structure and dynamics of (H$_2$O)$_2$". In: *Phys. Rev. B* 48 (4 1993), pp. 2081–2097.

[175]   John P. Perdew, Kieron Burke, and Matthias Ernzerhof. "Generalized Gradient Approximation Made Simple". In: *Phys. Rev. Lett.* 77 (18 1996), pp. 3865–3868.

[176]   Stefan Grimme. "Semiempirical GGA-type density functional constructed with a long-range dispersion correction". In: *Journal of Computational Chemistry* 27.15 (2006), pp. 1787–1799.

[177]   M. J. Frisch et al. *Gaussian 09, Revision D.01*. Tech. rep. Wallingford CT: Gaussian, Inc., 2009.

[178]   V. Masson-Delmotte et al. *Global Warming of 1.5°C. An IPCC Special Report on the impacts of global warming of 1.5°C above pre-industrial levels and related global greenhouse gas emission pathways, in the context of strengthening the global response to the threat of climate change, sustainable development, and efforts to eradicate poverty.* Report. 2018.

[179]   Kai Man Kerry Yu et al. "Recent Advances in CO_2 Capture and Utilization". In: *ChemSusChem* 1.11 (2008), pp. 893–899.

[180]   D. Neuwirth et al. "Two reaction regimes in the oxidation of larger cationic tantalum clusters (Ta_n^+, n = 13-40) under multi-collision conditions". In: *Phys. Chem. Chem. Phys.* 18 (11 2016), pp. 8115–8119.

[181]   Wei Fa, Chuanfu Luo, and Jinming Dong. "Coexistence of ferroelectricity and ferromagnetism in tantalum clusters". In: *The Journal of Chemical Physics* 125.11 (2006), p. 114305.

[182]   Z.J. Wu, Y. Kawazoe, and J. Meng. "Geometries and electronic properties of Ta_n, Ta_nO and TaO_n (n = 1-3) clusters". In: *Journal of Molecular Structure: THEOCHEM* 764.1 (2006), pp. 123–132.

[183]   André Fielicke et al. "Infrared Spectroscopy and Binding Geometries of Oxygen Atoms Bound to Cationic Tantalum Clusters". In: *The Journal of Physical Chemistry A* 114.36 (2010), pp. 9755–9761.

[184]   Jörg Meyer and Karsten Reuter. "Modeling Heat Dissipation at the Nanoscale: An Embedding Approach for Chemical Reaction Dynamics on Metal Surfaces". In: *Angewandte Chemie International Edition* 53.18 (2014), pp. 4721–4724.

[185]   Frank Neese et al. "The ORCA quantum chemistry program package". In: *The Journal of Chemical Physics* 152.22 (2020), p. 224108.

[186]   Yingkai Zhang and Weitao Yang. "Comment on "Generalized Gradient Approximation Made Simple"". In: *Phys. Rev. Lett.* 80 (4 1998), pp. 890–890.

[187]   Florian Weigend and Reinhart Ahlrichs. "Balanced basis sets of split valence, triple zeta valence and quadruple zeta valence quality for H to Rn: Design and assessment of accuracy". In: *Phys. Chem. Chem. Phys.* 7 (18 2005), pp. 3297–3305.

[188]   Jiguang Du, Xiyuan Sun, and Gang Jiang. "A theoretical study on Ta_n^+ cluster cations: Structural assignments, stability, and electronic properties". In: *The Journal of Chemical Physics* 136.9 (2012), p. 094311.

[189]   Jun Bao et al. "Significant Advances in C1 Catalysis: Highly Efficient Catalysts and Catalytic Reactions". In: *ACS Catalysis* 9.4 (2019), pp. 3026–3053.

[190]   W Huang et al. "Possibility of Direct Conversion of CH_4 and CO_2 to High-Value Products". In: *Journal of Catalysis* 201.1 (2001), pp. 100–104.

[191]   Esther M Wilcox, George W Roberts, and James J Spivey. "Direct catalytic formation of acetic acid from CO_2 and methane". In: *Catalysis Today* 88.1 (2003), pp. 83–90.

[192]   Yi-Hui Ding, Wei Huang, and Yong-Gang Wang. "Direct synthesis of acetic acid from CH_4 and CO_2 by a step-wise route over Pd/SiO_2 and Rh/SiO_2 catalysts". In: *Fuel Processing Technology* 88.4 (2007), pp. 319–324.

[193]   Xiumei Wang et al. "NMR-Spectroscopic Evidence of Intermediate-Dependent Pathways for Acetic Acid Formation from Methane and Carbon Monoxide over a ZnZSM-5 Zeolite Catalyst". In: *Angewandte Chemie International Edition* 51.16 (2012), pp. 3850–3853.

[194]   Abdelrahman M. Rabie, Mohamed A. Betiha, and Sang-Eon Park. "Direct synthesis of acetic acid by simultaneous co-activation of methane and CO_2 over Cu-exchanged ZSM-5 catalysts". In: *Applied Catalysis B: Environmental* 215 (2017), pp. 50–59.

[195]   Caiyun Geng et al. "Ta_2^+-mediated ammonia synthesis from N_2 and H_2 at ambient temperature". In: *Proceedings of the National Academy of Sciences* 115.46 (2018), pp. 11680–11687.

[196]   Yuntao Zhao et al. "Direct C–C Coupling of CO_2 and the Methyl Group from CH_4 Activation through Facile Insertion of CO_2 into $Zn-CH_3$ σ-Bond". In: *Journal of the American Chemical Society* 138.32 (2016), pp. 10191–10198.

[197]   Yuntao Zhao et al. "Active Site Ensembles Enabled C–C Coupling of CO_2 and CH_4 for Acetone Production". In: *The Journal of Physical Chemistry C* 122.17 (2018), pp. 9570–9577.

[198]   Yuan Yang et al. "Catalytic Co-Conversion of CH_4 and CO_2 Mediated by Rhodium-Titanium Oxide Anions $RhTiO_2^-$". In: *Angewandte Chemie International Edition* 60.25 (2021), pp. 13788–13792.

[199]   M. J. Frisch et al. *Gaussian 09, Revision D.01*. Tech. rep. Wallingford CT: Gaussian, Inc., 2010.

[200]   Jochen Heyd, Gustavo E. Scuseria, and Matthias Ernzerhof. "Hybrid functionals based on a screened Coulomb potential". In: *The Journal of Chemical Physics* 118.18 (2003), pp. 8207–8215.

[201]   Florian Weigend. "Accurate Coulomb-fitting basis sets for H to Rn". In: *Phys. Chem. Chem. Phys.* 8 (9 2006), pp. 1057–1065.

Acknowledgements

I am very thankful to the people who helped me on the long and not always smooth way to obtain the degree.

The very work would not have happened, if Ueli Heiz had not confided this research project to me, even though I had never worked on a similar topic before. His trust and support has led me through the entire course of my doctorate. Martin Tschurl has significantly contributed to the success of this work: he educated me good scientific practices, and his confidence and leadership guided me through my studies. I am indebted to Jozef Lengyel for the warm and friendly ambience in the group and for his immediate help and advice in the daily laboratory routine. I am also obliged to George Goddard and Tsugunosuke Masubuchi, who gave me a nice introduction to the experiment and thus tremendously relieved my adaptation to the lab.

I would like to express my profound gratitude to Robert Spitzenpfeil for his technical assistance and Daniela Reicheneder who was always there to help with administrative issues. I am also very grateful to Christian Schmid and Leo Maeser for their efforts in coding the data-analysis programs.

I would like to thank all the members of the Heiz group, with whom I shared a lot of amusing memorable moments and conversations during our outdoor sport activities, Kicker sessions, and BBQ parties.

My special thanks go to my family, that has always been very supportive and reassuring throughout my doctorate.